Measurement of Charged Particles from the Hadronic Final State of Electron-Proton Deep Inelastic Scattering at a Centre of Mass Energy of 296 GeV

Corinna Catterall
University College, London

A thesis submitted for the degree of
Doctor of Philosophy
at the University of London

September 17, 1995

Measurement of Charged Particles from the Hadronic Final State of Electron-Proton Deep Inelastic Scattering at a Centre of Mass Energy of 296 GeV

Abstract

Charged particles from the hadronic final state of electron-proton deep inelastic scattering at HERA are measured by the Central Tracking Detector (CTD), a component of the ZEUS detector.

The operation of the CTD is described. Using the incomplete tracking data from 1992 and the first data, taken during 1993, for which the CTD was fully instrumented, some systematic effects on the measurement of charged particles are investigated, and where possible, corrected. Factors affecting assignment of tracks to the main event vertex are discussed. The angular and momentum ranges which are reliable for physics analysis are identified.

Momentum flow of charged hadrons, in pseudorapidity and in azimuth, is measured in the HERA laboratory frame with respect to the nominal direction of the struck quark, which is obtained from the reconstructed event kinematics. Comparisons are made with the predictions of three Monte Carlo models. Monte Carlo techniques are used to correct the data for detector effects.

The reconstructed momentum four-vectors of the charged hadrons are transformed to the Breit frame, where the momentum flow versus pseudorapidity is measured. Scaled momentum spectra of final state hadrons associated, in the Breit frame, with the fragmentation region of the struck quark (*current region*), are measured. The evolution of multiplicity and scaled momentum distributions with increasing virtuality Q of the mediating photon are shown and compared with data from e^+e^- annihilation experiments.

The increased effect at low x-Q^2 of initial-state QCD radiation in DIS is evident both in the momentum flow distributions and in the Breit-frame evolution of current region multiplicity with Q, but appears not to significantly affect the scaled momentum evolution which is found to be consistent with e^+e^- results.

Contents

List of Figures

List of Tables

Acknowledgements

Returning to an early interest in physics after a long detour, I have come to PhD work by an unconventional path. The people who have influenced its twists and turns are too numerous to list here, but I will attempt to acknowledge, in almost chronological order, those who have most directly contributed to making this thesis possible. If I have missed or miss-spelled anybody, sorry.

My first thanks are to the "gang of four" Peter Chester, Dick Rowberry, Carmel Searson and Zena de Souza, who ran the CATALYST access course at the City and East London College, and to fellow students Olive and Penny.

I would next like to thank the ex-staff of the ex-Physics Department of the then City of London Polytechnic. With their entire department axed (in preparation for University status?), they facilitated my entry into Queen Mary and Westfield (QMW) College.

Many thanks go to the staff of the Department of Physics at QMW for my three years there as an undergraduate, and particularly to Graham Thompson, supervisor of my third-year project, whose energy, enthusiasm and sound advice provided me with an invaluable foundation for particle physics research.

As a PhD student from University College London (UCL), who has been based at DESY, Hamburg, I owe many thanks to people at both DESY and UCL, and importantly to PPARC for funding my work.

At DESY, thanks are due to the members of the ZEUS collaboration, particularly to Ken Long, for showing me around the CTD software, to Nick Brook, Tony Doyle and Valerie Jamieson of the Glasgow group, for a wide range of DIS-related help and for comments on my thesis, and to Malcolm Derrick, Anatoly Solomin and Lydia Shcheglova for their charged multiplicity work.

Thank you Susan Ketels for steering my children and I through the German bureacracy, and Frau Silz and Rebecca for providing childcare.

At UCL I owe thanks to the Department of Physics and Astronomy, in particular the HEP group, for taking me on as a student. I wish to thank my supervisor, Tegid Jones, for his help and encouragement and his readiness, on occasion, to tackle the "heathen hordes". Thanks also to David Miller, for first-year coursework supervision and for allowing Gordon, Kwasi, Phil, Sabah and me to sabotage the Halzen and Martin sessions. Thanks to Julian Shulman, for his FADC pulse work and for continuously swearing at his computer.

I am especially grateful to John Lane, for his work on systematic tracking effects which he pioneered within ZEUS, for some interesting insights into the Breit frame analysis (including a memorable series of late-night email discussions about $\hat{s}$, $\hat{t}$ and "mud in the Breit frame"), for thoroughly proof-reading and commenting on everything, and for encouraging me when I was at my most dispairing. Thanks John.

My final thanks are to my children Ken and Karen, for giving me a reason to keep going, and for making a racket in Building 1 when I had told them not to.

Foreword

This is a small part of a story about learning to see.

Throughout history, humankind has been driven by a curiosity about things which lie beyond the limits of perception – in regions tantalisingly within the grasp of the intellect but beyond reach of the senses. Time and time again, we have managed, by some or other ingenious means or contrivance, to artificially extend the capabilities of our senses in order to test the results of our reasoning and deduction. Each time the boundaries of our conceptualisation have, in turn, retreated ahead of us.

The physics of elementary particles is the study of the very small. Cosmology is the study of the very large. The two are inextricably linked, because the fundamental forces which govern the creation and interactions of the tiniest constituents of matter are also believed to be responsible for the creation and ultimate fate of the entire universe.

We have invented microscopes for looking at small objects and telescopes for looking at large distant objects. Still the conjectured boundaries of the universe remain inaccessible even to our most sophisticated telescopes, and electron microscopes, while they can utilise quantum tunnelling effects to generate images of individual atoms, are unable to resolve structures at a subatomic level.

An accelerator ring which collides electron and proton beams at high energies, HERA, situated in Hamburg, Germany, has been described as the world's largest and most powerful electron microscope, as it uses an electron beam to probe the structure of the proton. It could eventually provide an indication of whether the quarks which make up the proton are truly fundamental constituents of matter or whether they in turn are composed of yet smaller particles. But if HERA is a microscope, how do we use it to see?

Perhaps it can be said that HERA the microscope is equipped with its own two giant artificial eyes. These are the particle detectors ZEUS and H1, and they have been designed and built to directly observe the structure of a proton, as revealed in the illumination of an electron beam, functioning in conditions which would cause immediate destruction of a human eye.

The human eye, like ZEUS and H1, is a detector of elementary particles. It is compact, intricate, efficient, extremely sensitive, and highly specialised for operation with photons in the visible light range. The retina of the eye consists of

tightly-packed cells. The deposition of photon energy in a cell generates a nerve impulse, a "raw signal" which is passed, via an individual connection in the optic nerve bundle, to a a system of "read-out" neurons in the visual cortex of the brain.

The function of the eye itself is only the first stage in the process of vision. In order to be "seen" as a recognisable structure, the initial raw signals must undergo, in the brain, many stages of processing, the sophistication and complexity of which is of considerable current interest to neuroscience and the "cognitive" branch of computer science alike.

Conventional electron microscopes produce photographic images, thereby presenting data to the human eye in a form which can be interfaced directly to the brain's "in-house software", so that the resulting interpretations are transferred instantly to the conscious mind. The output from ZEUS and H1, however, is not accepted as recognisable input by the human brain. So to look at the proton through HERA, we must, in addition to building artificial eyes, somehow emulate the functions of the brain's visual circuitry.

To be made comprehensible, the raw data from the detector read-out electronics must undergo processing by a variety of computers, by the conscious intellects of the international collaborations of humans staffing the detectors, and finally by the wider association of humans which constitutes the world particle physics community.

Pattern recognition, event reconstruction, rejection of irrelevant background and correction for systematic mismeasurement are all essential to this – tasks which the human brain performs unconsciously and effortlessly on the data it receives from its visual cortex.

Sometimes pictures are constructed of individual electron-proton collisions observed in ZEUS and H1. However, most analysis takes place via accumulation of"high statistics" data from large numbers ($\sim 10^4 - \sim 10^6$) of events. Again, this is similar to the operation of human vision, in which the observation of large numbers of scattered photons makes it possible to discern, for example, variations in intensity (light and shade) caused by the existence of preferred scattering angles, which are perceived as structure.

Important in this context are a variety of software utilities developed at CERN (including CERNLIB, GEANT, HBOOK, ZEBRA and PAW), the high-powered computing facilities at academic institutes in scores of countries, and, crucially, the worldwide nerve system of the Internet. All of these are as integral to a present-day high energy particle physics experiment as is the actual accelerator and detector hardware.

This thesis can be regarded as an account of some of the pathways followed in the process of learning to "see" with the ZEUS detector, and, in particular, of learning to interpret the signals produced by charged particles in the ZEUS Central Tracking Detector.

Chapter 1 contains a brief description of HERA and of the principal types of

interactions observed there. A general description of ZEUS is given in Chapter 2, while Chapter 3 describes the ZEUS Central Tracking Dector.

Particular attention is given, in Chapters 4 and 5, to the causes and correction of systematic effects which could result in misinterpretation of the data. The distinction between relevant and irrelevant data – what is of interest and what constitutes unimportant or confusing background – is also a necessary part of learning to see, and contributes to Chapters 5 and 6.

It is necessary to understand the limitations of our sight, and to assess its reliability. To aid this we compare what we see with what we expected to see using "Monte Carlo" simulation, perhaps our closest approximation, in software, to imagination. These topics feature in Chapters 6 and 7.

Finally, in Chapters 7 and 8, the understanding which has been gained regarding the functioning of the ZEUS "eye" is used to observe the final state of a proton which has disintegrated on collision with an electron. From measurement of the resulting sprays of particles, some underlying characteristics of the constituents of the proton and their interactions with one another are inferred.

Chapter 1

Physics at HERA

1.1 Overview of HERA

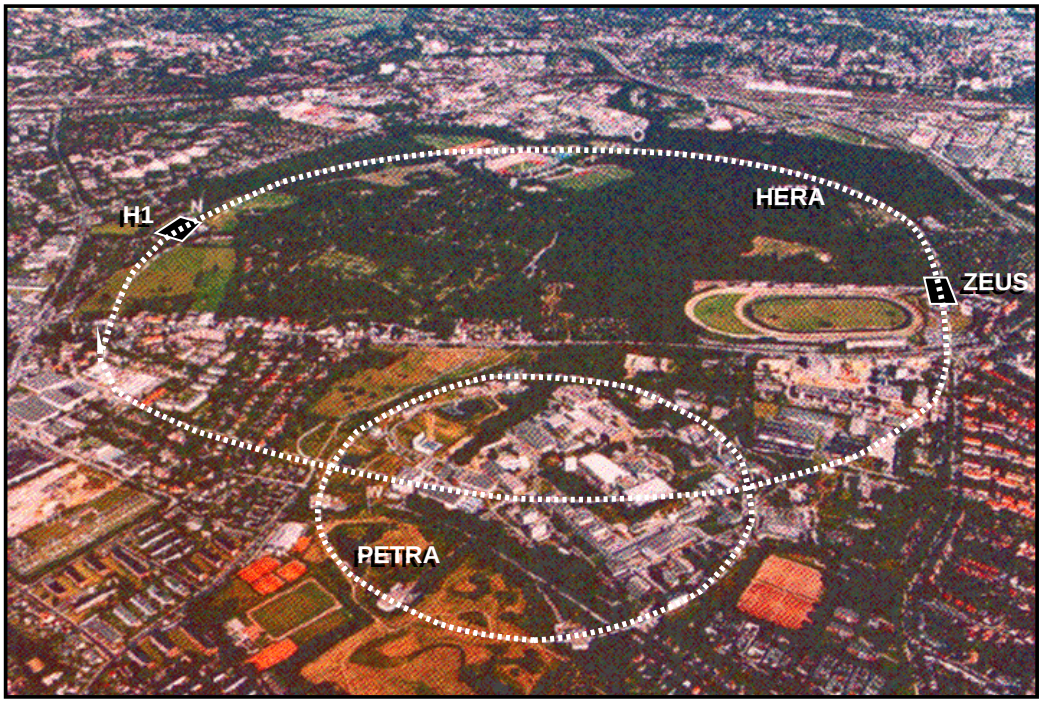

Figure 1.1: *Aerial view of the DESY site in Hamburg, showing the locations of the HERA ring, the PETRA ring, now used as a pre-accelerator for HERA, and the two detectors, ZEUS and H1.*

1.1.1 HERA and Its Detectors

The **H**adron **E**lectron **R**ing **A**nlage (*HERA*) is the world's first electron-proton colliding beam accelerator. Constructed by the German National Particle Physics Laboratory, DESY (*Deutsches Electronen Synchotron*), it is housed in a 6.3 *km*

long tunnel, situated beneath a suburb of Hamburg. The project was approved in 1984, the first electron-proton collisions were observed in October 1991, and regular data-taking commenced in May 1992.

There are two independent storage rings in HERA, one for electrons (or positrons), and one for protons (or deuterons). These rings are not uniform circles but are composed of four arcs, each with a radius of curvature of 779 m, joined by four straight sections each 360 m long. There are interaction points in three of the straight sections, and injection takes place in the fourth. Two large detectors, H1 and ZEUS, have been built around the north and south interaction points respectively. At the third interaction point, in the east, the HERMES detector, which will observe collisions of polarised electrons or positrons with a gas jet target, was still under construction during 1993.

1.1.2 Injection and Acceleration of the Beams

Injection of electrons and protons into HERA takes place in a series of stages involving several pre-accelerators.

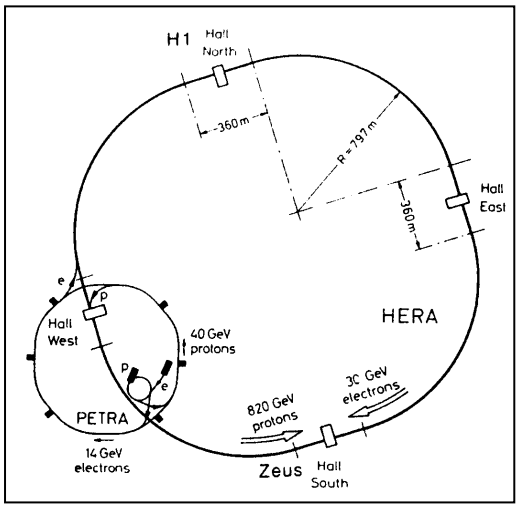

Figure 1.2: *Plan of HERA and its pre-accelerators.*

The layout of HERA and its pre-accelerators is shown in figure 1.2. Electrons are first accelerated up to 200 MeV in the linear accelerator LINAC II, then further accelerated to 7.5 GeV in the DESY II synchrotron. From there they are injected into the PETRA ring where they are ramped up to 14 GeV for injection into HERA. The protons start off as H^- ions which are accelerated to 50 MeV in the proton LINAC. They are next accelerated to 7.5 GeV in DESY III, after which the electrons are stripped off. The protons are then accelerated to 40 GeV in PETRA, ready for injection into HERA.

In HERA the protons, guided around the ring by means of superconducting dipole and quadrupole magnets, are accelerated up to 820 GeV using conventional (non-superconducting) radiofrequency cavities.

The electron ring uses warm (non-superconducting) magnets, and a mixture of conventional and superconducting radiofrequency cavities to accelerate the electrons up to a possible 30 GeV.

Close to the interaction region, the protons and electrons must have the same orbit in order to collide at zero angle. Therefore the protons are deflected by means of guiding magnets until they run in the same vaccuum pipe as the elec-

trons, and are brought back to the proton ring after passing the interaction point.

1.1.3 Running Conditions and Luminosity

The electrons and protons are constrained by the radiofrequency to travel in "bunches". With a separation of 29 m between bunches, HERA has the capacity for 220 bunches in each beam. The time between bunch crossings is 96 ns.

The design luminosity of HERA is $1.5 \times 10^{31}\ cm^{-2}s^{-1}$. Nominal energies of the electron and proton beams are 30 GeV and 820 GeV respectively, giving a centre-of-mass energy, $\sqrt{s}$, of 314 GeV.

During 1993 HERA ran with 84 paired bunches, and an additional 10 electron and 6 proton bunches were left unpaired for background studies. Since not all of the accelerator cavities were installed, the electron beam energy was 26.67 GeV, The proton beam was at its design value of 820 GeV, and the resulting centre-of-mass energy was 296 GeV. In 1993 HERA delivered to ZEUS a total integrated luminosity of $\sim 1000\ nb^{-1}$ of which $\sim 600\ nb^{-1}$ was recorded onto tape.

1.2 Deep Inelastic Lepton-Nucleon Scattering

1.2.1 Introduction to DIS

The term Deep Inelastic Scattering (DIS) describes inelastic lepton-nucleon collisions in which the momentum transfer between the lepton and nucleon is sufficient that, in accordance with the Heisenberg uncertainty relation $\Delta p \Delta x > \hbar$, distances significantly smaller than the nucleon radius can be resolved. In an analogue to the Rutherford scattering experiments [1] which first revealed atomic structure, the lepton in DIS acts as a probe which can reveal substructures within the nucleon.

Previous to HERA, DIS experiments have involved firing a beam of leptons (electrons, muons or neutrinos) at a fixed nucleon target such as liquid hydrogen. For fixed target experiments the momentum transfer is limited by the lepton beam energy. Colliding an electron of momentum 30 GeV with a proton of momentum 820 GeV at HERA is equivalent to scattering a 52500 GeV electron off a stationary proton target. Thus HERA is capable of resolving distances a factor of 10^3 smaller than the proton radius.

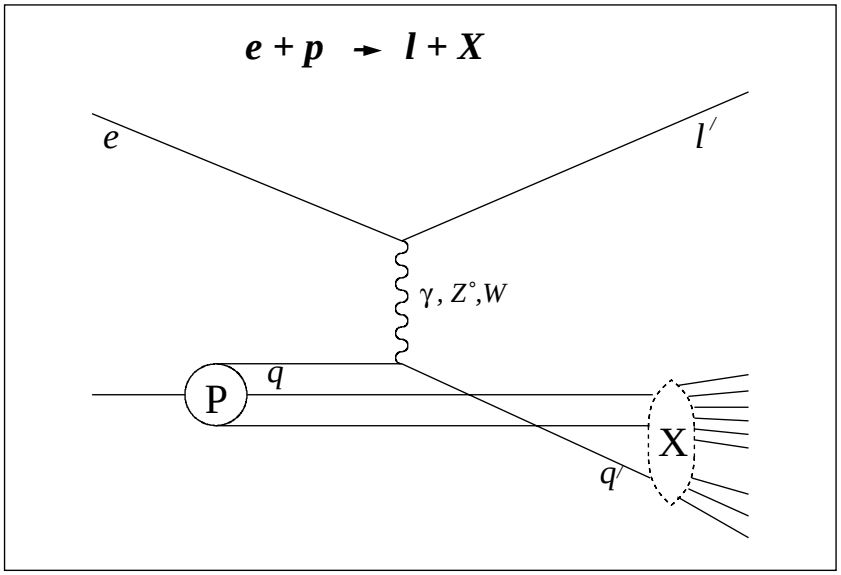

Figure 1.3: *Feynman diagram of the generic HERA interaction* $e + p \rightarrow l + X$

The mediating boson in DIS can be a photon or Z^0 boson (neutral current), where the lepton retains its identity, or a $W^{\pm}$ boson (charged current), where the lepton identity changes. The proton usually breaks up, forming a final state, X, of hadrons, most of which are mesons, which are often emitted in collimated "jets".

Figure 1.3 shows the Feynman diagram for the generic HERA interaction,

$e + p \rightarrow l + X$, where l is the scattered electron in a neutral current interaction or a neutrino in a charged current interaction, and X is the unspecified hadronic final state of the proton.

Interactions involving $W^{\pm}$ or Z^0 exchange, constitute an important future topic for HERA investigations. However, the integrated luminosity of 1993 yielded very few such events, as they are heavily suppressed due to the effect of the weak boson mass. In the kinematic region under investigation in this thesis it can be safely assumed that there is no contribution from weak virtual boson exchange. The DIS events referred to hereafter are therefore taken to be neutral current, mediated by the exchange of a virtual photon.

1.2.2 Standard DIS Kinematic Variables

For the DIS process $e(k) + p(P) \rightarrow e(k') + X$, the incoming four-vectors for the hadronic vertex are given by the momentum transfer q from the leptonic vertex and the proton four-momentum P. The hadronic mass W is given by

$$W^2 = P^2 + q^2 + 2P.q \tag{1.1}$$

and thus depends only on the variables q^2 and $2P.q$.

Since the exchanged boson is spacelike, q^2 is negative. The momentum transfer is customarily denoted by the positive quantity

$$Q^2 = -q^2. \tag{1.2}$$

Also in standard use are the dimensionless variables

$$x = \frac{Q^2}{2P.q} \tag{1.3}$$

and

$$y = \frac{q.P}{k.P}, \tag{1.4}$$

both of which are Lorentz-invariant and take values between 0 and 1.

If DIS is regarded as an interaction with a proton constituent, or *parton*, then x can be interpreted as the fractional momentum of the parton with respect to the proton momentum. In the proton rest frame y is the fraction of the electron energy taken by the virtual photon, but in the HERA frame y does not have a similarly intuitive interpretation.

The above three variables are related to one another by

$$Q^2 = sxy, \tag{1.5}$$

where s is the centre-of-mass energy squared of the ep system. Any two of x, y and Q^2 can therefore be used to completely specify the kinematics of the interaction.

1.2.3 DIS Cross Sections and Proton Structure

The cross-section for neutral current ep DIS [2], neglecting terms which depend on Z^0 exchange, is given by

$$\frac{d^2\sigma}{dxdQ^2} = \frac{4\pi\alpha^2}{xQ^4}\left[(1-y)F_2(x,Q^2) + y^2xF_1(x,Q^2)\right] \tag{1.6}$$

where α is the electromagnetic coupling constant. The dimensionless quantities F_1 and F_2 are known as *structure functions*, which embody our knowledge or ignorance of the virtual boson-nucleon interaction, and in general can depend on x and Q^2. The proton structure functions are related to the virtual γ^*p cross-section by

$$2xF_1(x,Q^2) = \frac{Q^2}{4\pi^2\alpha}(1-x)\sigma_T(x,Q^2) \tag{1.7}$$

and

$$F_2(x,Q^2) = \frac{Q^2}{4\pi^2\alpha}(1-x)[\sigma_T(x,Q^2) + \sigma_L(x,Q^2)] \tag{1.8}$$

where σ_T and σ_L are the respective cross sections for the transverse and longitudinally polarised virtual photon.

If σ_L can be taken to be small, then equations 1.7 and 1.8 yield the Callan-Gross [3] relation

$$2xF_1(x,Q^2) = F_2(x,Q^2) \tag{1.9}$$

The cross section for ep scattering can then be expressed in terms of F_2 as

$$\frac{d^2\sigma}{dxdQ^2} = \frac{2\pi\alpha^2}{xQ^4}[1+(1-y)^2]F_2(x,Q^2) \tag{1.10}$$

1.2.4 Photoproduction

For values of Q^2 below $\sim$ 1 GeV^2, the mediating photon can be regarded as "quasi-real" ($m^2 = q^2 \approx 0$). The structure of the photon, rather than the proton, is probed by the interaction. The electron is deflected only slightly, and is therefore not observed in the main body of the detector, but it may be observed in the LUMI detector (chapter 2, section 2.4.2). Due to the Q^4 term in the denominator of equation 1.6, the cross section for photoproduction is much larger than that for DIS. Photoproduction is a major area of study at HERA, but in a DIS event sample it forms an unwanted background, the removal of which is discussed in chapter 6, section 6.3.2.

1.3 The Quark-Parton Model

1.3.1 Historical Background to the Quark Hypothesis

In DIS experiments at SLAC [4] in the late 1960's it was observed that the structure functions approximately scaled, i.e. they were dependent on x but were not significantly dependent on Q^2 at a given value of x. Bjorken scaling was understood to demonstrate that the virtual photon was interacting with a point-like constituent (termed a *parton*) of the proton carrying a fraction x of the proton momentum.

This first experimental evidence of proton substructure supported the proposal, put forward in 1964 by Gell-Mann and Zweig as an explanation for the symmetries observed in baryon and meson resonances, that hadrons were composed of spin 1/2 particles termed *quarks*.

The Gell-Mann proposal required quarks to be of three types, or *flavours*, up u, with charge $+2/3$, down d with charge $-1/3$ and strange s with charge $-1/3$, each with a corresponding anti-particle of equal and opposite charge. Baryons were proposed to consist of three quarks (qqq) and mesons of a quark and anti-quark ($q\bar{q}$), the combination of quark charges giving net integer hadron charge in each case.

According to this scheme the Ω^-, Δ^- and Δ^{++} baryons would contain three quarks identical in flavour and in spin, violating the Pauli exclusion principle. To avoid this, quarks were proposed to have an additional degree of freedom, *colour*, which could take three values, r, g and b. From the observed hadron symmetries, flavour was postulated to have the property of $SU(3)$ symmetry, and colour likewise.

With the subsequent discovery of the c, b and recently the t quark resonances, the idea of $SU(3)$ flavour symmetry has been superceded by the Standard Model, in which the quarks are grouped into three "generations", $\{u,d\}$,$\{c,s\}$ and $\{t,b\}$, corresponding to the $\{e,\nu_e\}$, $\{\mu,\nu_\mu\}$ and $\{\tau,\nu_\tau\}$ lepton generations. However, $SU(3)$ flavour is of historical interest because it led to the hypothesis of quarks and to $SU(3)$ colour symmetry, which forms the basis of Quantum Chromodynamics (QCD), the currently accepted formalism of the strong interaction.

The quarks are believed to form a fundamental triplet of the $SU(3)$ colour symmetry group. Hadrons, exhibiting none of the properties attributed to colour, are required to belong to singlet representations of the group, which means that they have no net colour charge.

The octet representation of the colour group is occupied by the *gluons*, which are believed to be the carriers of the strong force. The major difference between electromagnetic and strong interactions is that the gluons themselves carry colour charge. As a result of this (section 1.4.1), the strong coupling constant α_s decreases at small distances, enabling quarks within the nucleon to behave essentially as free particles. At larger distances α_s becomes stronger, so that the

quarks are confined within the nucleus, accounting for the fact that they have never been observed as free particles.

1.3.2 DIS According to the Quark-Parton Model

The Quark-Parton Model (QPM) [5], developed from the early DIS results, is a simple formulation of quark interactions and hadron structure. In this model the gluon is essentially ignored, other than as a means of confining the quarks within the hadron, and interactions between quarks and gluons are neglected. In the QPM picture of ep DIS, the proton essentially consists of three "valence quarks" (uud), which are not considered to interact either with one another or with accompanying "sea-quarks" (virtual $q\bar{q}$ pairs).

The lepton scatters off a massless quark in the proton, as shown in figure 1.4, and the quark is dislodged. Unable to exist as an isolated object, it materialises into hadrons which, correlated in direction with the original quark, form the "current jet". The remaining quarks in the proton do not participate in the interaction, and continue in the original proton direction. After the removal of the struck quark the proton remnant also hadronises to form a "spectator jet".

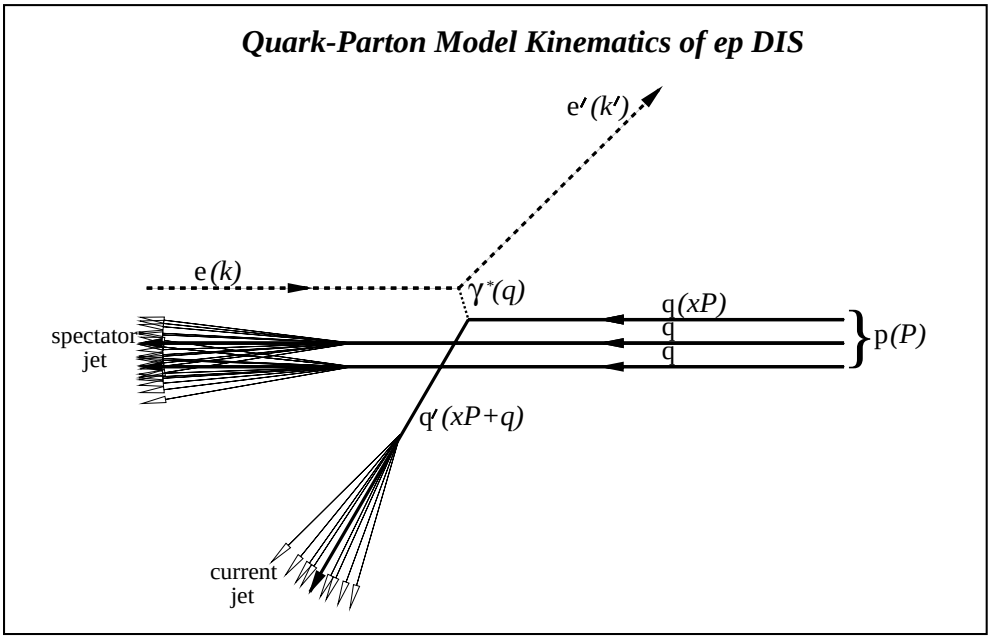

Figure 1.4: *QPM Kinematics for DIS.*

Thus the QPM kinematics of DIS are of a two body $\rightarrow$ two body configuration: $e(k) + q(xP) \rightarrow e'(k-q) + q'(xP+q)$, and are completely specified, at the quark level, by the incoming electron and proton four-momenta and any two of the variables x, y and Q^2 defined in section 1.2.2.

1.4 Gluons and QCD

1.4.1 Evidence for Gluons

If the probability to find a quark carrying a fraction x of the proton momentum is $q(x)$ then $F_2(x)$ is related to the quark x distribution by

$$F_2(x) = \sum_i e_i^2 x \left(q_i(x) + \bar{q}_i(x)\right) \tag{1.11}$$

where the sum i is over the quark flavours and e_i is the charge of a quark of flavour i.

Integrating $F_2(x)$ over x gives the overall momentum fraction of the proton carried by its charged constituents. Electrically neutral constituents make no contribution to F_2 as they do not interact with the virtual photon. A proton consisting solely of charged quarks, as in the QPM, would give

$$\int_0^1 F_2(x)dx = 1,$$

whereas the measurent of $\int F_2(x)dx$ gives a value of about 0.5. This indicates that about half the momentum in the proton is carried by neutral partons which are believed to be gluons.

Since gluons can form $q\bar{q}$ pairs, the proton has, in addition to the valence quark distributions $u_v(x)$ and $d_v(x)$ for the up and down quarks, the sea quark distributions $u_s(x) = \bar{u}_s(x)$ and $d_s(x) = \bar{d}_s(x)$, as well as contributions from the strange and heavier flavoured quarks in the sea, and the gluon distribution $g(x)$ which has to be determined by indirect means.

The gluons mediate the colour interaction between the quarks, the coupling α_s being of the form

$$\alpha_s(Q^2) = \frac{12\pi}{(33 - 2N_f) ln(Q^2/\Lambda^2_{QCD})} \tag{1.12}$$

where N_f is the number of quark flavours and Λ is a parameter which denotes the energy at which α_s is sufficiently large that perturbative calculations are not valid and the partons become confined within a hadron. For $Q^2 \gg \Lambda^2$, α_s is small and perturbative calculations can be used.

1.4.2 QCD Corrections to DIS

The leading order (LO) QCD processes, shown in figure 1.5, are Boson Gluon Fusion (BGF) and QCD Compton. These QCD corrections to the QPM cause the structure functions and parton distributions to evolve with Q^2 thereby violating

Bjorken scaling. The evolution for a quark density $q_i(x,Q^2)$ is given by the GLAP [6] evolution

$$\frac{d\,q(x,Q^2)}{d(\ln Q^2)} = \frac{\alpha_s(Q^2)}{2\pi}\int_x^1 \frac{d\,y}{y}\left[P_{qq}\left(\frac{x}{y}\right)q_i(y,Q^2) + P_{qg}\left(\frac{x}{y}\right)g(y,Q^2)\right] \qquad (1.13)$$

where $\alpha_s(Q^2)P_{qq}(\frac{x}{y})$ is proportional to the probability that a quark with momentum fraction x has come from a quark with momentum fraction y which has radiated a gluon, and $\alpha_s(Q^2)P_{qg}(\frac{x}{y})$ is proportional to the probability that a quark with momentum fraction x belongs to a $q\bar{q}$ pair created by a gluon of momentum fraction y.

The quantities $P_{qq}(\frac{x}{y})$ and $P_{qg}(\frac{x}{y})$ are two of the four *Altarelli-Parisi splitting functions* which govern the sharing of momentum in the parton branching. The remaining two, $P_{gq}(\frac{x}{y})$, and $P_{gg}(\frac{x}{y})$ describe the probability of a gluon with momentum x being radiated by a quark of momentum y and the probability of a gluon with momentum x coming from a triple gluon vertex in which the parent gluon has momentum y.

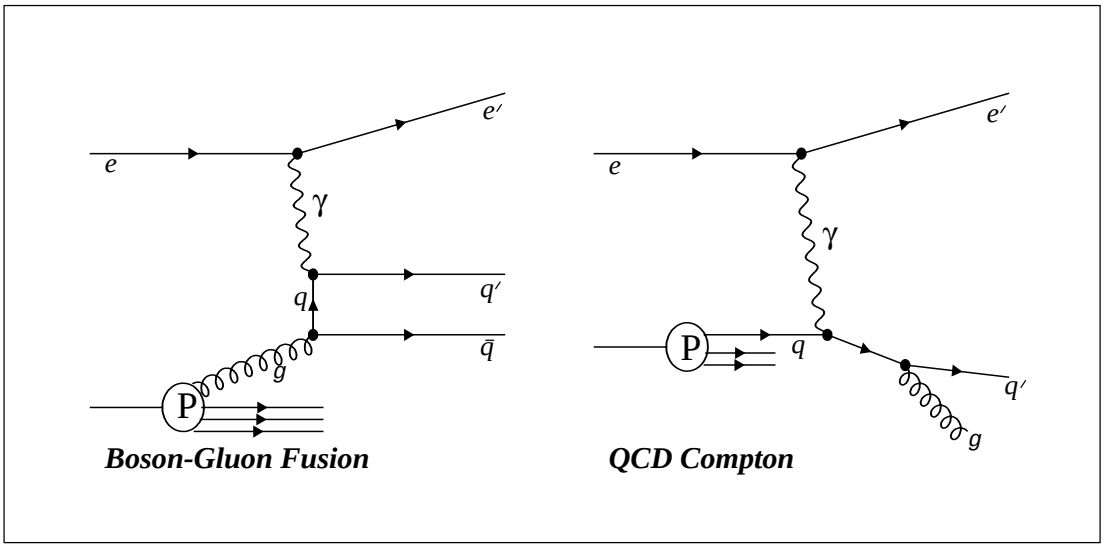

Figure 1.5: *Feynman diagrams of the $\mathcal{O}(\alpha_s)$ processes, Boson-Gluon Fusion* (left) *and QCD Compton* (right).

The Altarelli-Parisi splitting functions are also used in the perturbative calculation of higher order parton showering (PS) processes, both before coupling to the virtual photon (initial state) and after (final state).

1.4.3 Parton Shower Evolution

When QCD effects are taken into account, the current and remnant jets of DIS can no longer be considered to hadronise entirely independently of one another

since there is a colour flow between them mediated by a gluonic exchange.

As the outgoing quarks are decelerated by the force of the colour potential between them, formation of the hadronic final state is believed to take place via showers of radiated quarks and gluons, in a process analogous to electromagnetic showering. The perturbative phase of parton shower evolution [9] is governed by the Altarelli-Parisi splitting functions which determine how the momentum is divided between the two partons at each branching.

As the shower evolves, the individual partons are progressively less energetic. When the parton energies approach the cut-off scale Λ, α_s becomes sufficiently strong for perturbative QCD to break down and the non-perturbative stage of hadronisation is reached.

The inclusive process of "fragmentation", whereby an unobserved coloured parton is transformed into an observed colour-neutral hadronic system, is a major topic of this thesis.

1.4.4 DIS at Low x

At HERA the small x region $10^{-4} < x < 10^{-2}$ is for the first time accessible to physics analysis at values of $Q^2 > 4\ GeV^2$, where α_s is small enough for perturbative QCD to be applied. In fact, most analysis of 1993 data is primarily concerned with this region, since the 1993 luminosity provided little data at higher values of x.

Recent measurements of the structure function F_2 at HERA from both ZEUS [7] and H1 [8] show a strong rise of F_2 towards small x at fixed Q^2, increasing by a factor of about $2-3$ when x decreases from 10^{-2} to 10^{-4}.

At these low x values F_2 is dominated by the sea quark and gluon density functions; the quark which interacts with the virtual photon is usually the result of an initial state parton evolution characterised by multiple gluon branchings, often depicted (chapter 8, figure 8.3) in the form of a "ladder" diagram. In general, low x DIS is therefore a far more complicated process than the simple QPM two body $\rightarrow$ two body interaction described in section 1.3.2 (figure 1.4), and the kinematics can be expected to be somewhat different.

However, an interesting class of events has been observed at HERA, that of *Large Rapidity Gap* events or "diffractive DIS", in which the sea quark appears to couple not to a gluon but to a colourless object within the proton, generically termed the "pomeron". Diffractive DIS events are characterised by an absence of colour flow between the struck quark and the remnant, so that the QPM configuration persists even at low x.

For the non-diffractive DIS events observed at HERA, the energy flow and typical event configuration at low x indeed differ markedly from the QPM expectation. This, and its implications concerning the process of associating an observed final state particle with either the struck quark or the remnant, is investigated in detail in this thesis.

Chapter 2

The ZEUS Detector

2.1 The ZEUS Detector

The ZEUS detector is situated in the south interaction region of HERA, built and staffed by a collaboration of fifty institutes from twelve countries.

It is a hermetic detector; apart from a small region close to the beam pipe, it permits detection of the products of ep collisions emitted over the full 360° range.

The ZEUS co-ordinate system is right-handed Cartesian, with the positive Z-axis in the direction of the proton beam, the positive X-axis pointing to the centre of the HERA ring, and the origin at the nominal interaction point. A polar co-ordinate system is often used for event analysis. Here the polar angle θ measures the deviation from the positive Z-axis and the radial r-ϕ plane coincides with the X-Y plane.

2.1.1 Layout and Overview

Figure 2.1 shows ZEUS in Y-Z cross-section.

At the centre of the detector, closest to the beam pipe, and interaction region, is a Vertex Detector (VXD), which is surrounded radially by a Central Tracking Detector (CTD). To the front and rear of the CTD are the Forward Tracking Detector (FTD) and Rear Tracking Detector (RTD). Situated inside a superconducting coil designed to provide an axial magnetic field of 1.8 *Tesla*, this ensemble of inner tracking chambers allows measurement of charged particles emitted at polar angles from 7.5° to 170°.

The Uranium Calorimeter (UCAL), which encloses the inner tracking chambers and coil, is comprised of a cylindrical Barrel Calorimeter (BCAL), and Forward and Rear Calorimeters (FCAL, BCAL). A Hadron-Electron Separator (HES) is installed between the RCAL layers.

Surrounding the UCAL is a Backing Calorimeter (BAC), which measures energy leakage out of the main calorimeter. The BAC is made out of 7.3 *cm*

thick iron plates, which also serve as the return yoke for the superconducting magnets.

Muons are expected to pass through both calorimeters, so muon chambers, divided, similarly to the UCAL, into barrel, forward and rear sections, have been installed outside of the iron yoke (BMUO, FMUO, RMUO), and between the UCAL and the BAC (BMUI, FMUI, RMUI).

To the rear of the detector, a Veto Wall measures muons from the proton beam halo.

Components of ZEUS which are not visible in figure 2.1 are the Leading Proton Spectrometer (LPS), situated in the tunnel, 100 m forward from the interaction point, to detect forward-scattered protons, the Luminosity Monitor (LUMI), comprised of an electron and photon detector located respectively at about 35 m and 100 m to the rear of the interaction point (IP), and several small counters and collimators.

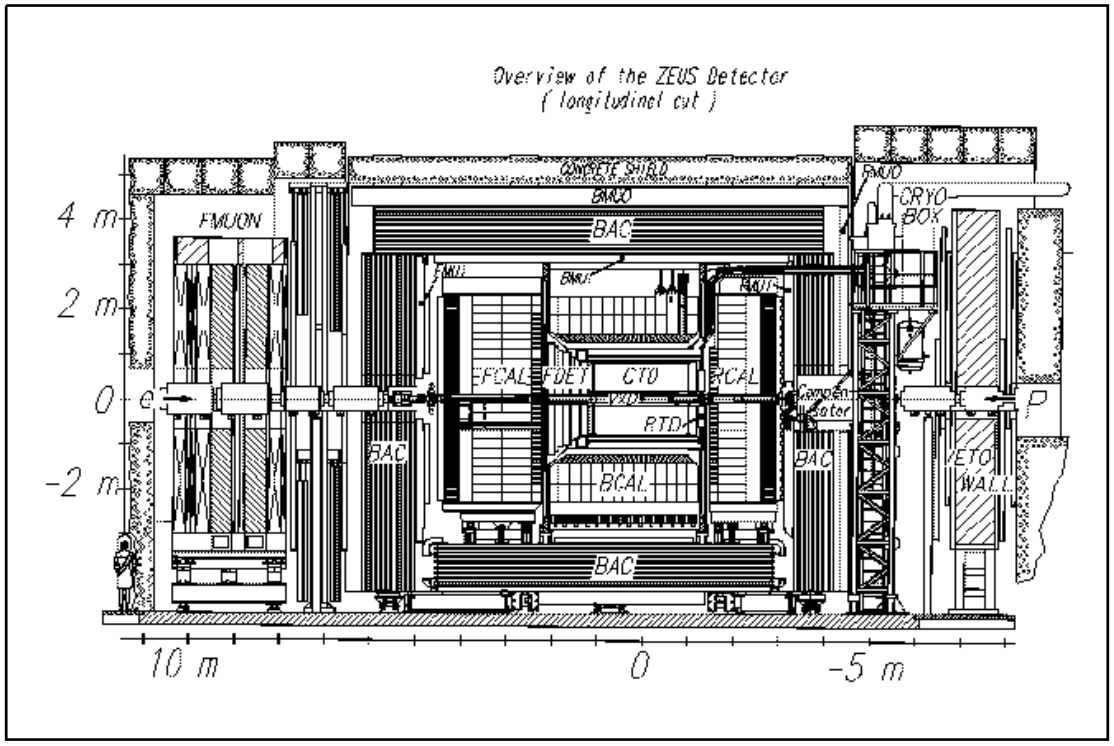

Figure 2.1: *The ZEUS Detector*

2.2 The Inner Tracking Detectors

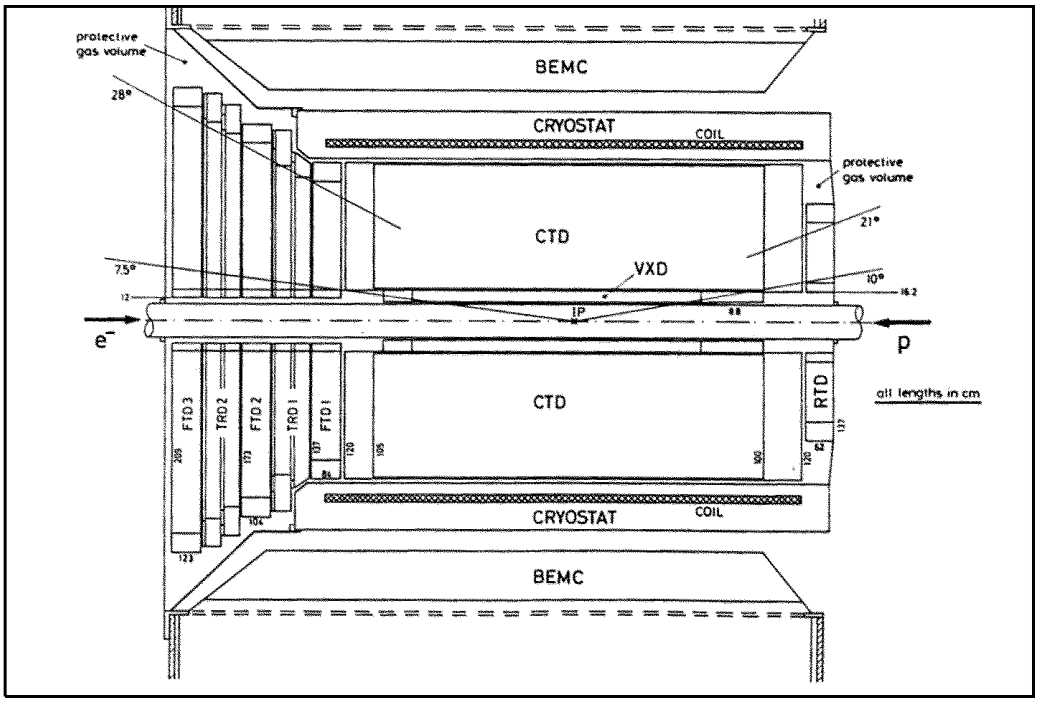

Figure 2.2: *The Inner Tracking Detectors.*

2.2.1 Objectives of the Inner Tracking Detectors

The ensemble of ZEUS inner tracking detectors, shown in figure 2.2, was designed

- to detect individual charged particles, including the scattered lepton in DIS events and particles within dense jets, over a wide angular range,
- to provide accurate measurement of momentum,
- to reconstruct tracks from decay products of short-lived particles,
- to provide identification of particle type using information from dE/dx and transition radiation,
- to give an accurate position measurement of the main event vertex, and
- to provide fast signals as an input to the event trigger.

2.2.2 The Magnetic Field

The momenta of charged particle tracks is obtained by measuring their curvature as they traverse a magnetic field. A strong field is necessary to give accurate

momentum measurement of high P_T tracks. For ZEUS this is provided by a superconducting solenoid situated between UCAL and the CTD. The coil is 2.46 m in length, with an inner diameter of 1.91 m. To date the coil has been operating at 1.43 *Tesla* although it is capable of producing a magnetic field of 1.8 *Tesla*. Since its length is only slightly greater than that of the CTD, the RTD and, particularly, the FTD, operate in an inhomogeneous field, whereas for the CTD and VXD the field is almost homogeneous.

2.2.3 The Vertex Detector

Innermost of the tracking detectors, and closest to the interaction point, the VXD is a cylindrical drift chamber consisting of 120 cells. Each cell has 12 sense wires running parallel to the Z-axis, from $Z = -50$ cm to $Z = +90$ cm. The sense wires are spaced 3 mm apart in the radial direction, the inner and outer radii of the VXD being at 9.9 cm and 15.9 cm respectively. The VXD has a polar angle acceptance from 8.6° to 165°.

Dimethyl-ether with a trace of oxygen was used as a drift gas.

The r-ϕ resolution achieved during 1993 was 50 μm in the central region of a cell (compared to a design resolution of 30 – 40 μm) and 150 μm near the edges.

2.2.4 The Central Tracking Detector

Radially surrounding the VXD, the CTD is a cylindrical drift chamber which extends from $Z = -100\,cm$ to $Z = +100\,cm$, with an inner radius of 16 cm and an outer radius of 80 cm, and with a polar angle acceptance from 15° to 164°.

This thesis is primarily concerned with tracking data from the CTD, therefore it is described in detail in the following chapter.

The r-ϕ resolution achieved during 1993 was $\sim 260\,\mu m$, and the two-track resolution was $\sim 2.5mm$.

2.2.5 Forward and Rear Tracking Detectors

The FTD and RTD were designed to extend the polar angle tracking acceptance to the front and rear of the CTD. The FTD, consisting of three planar drift chambers, separated in Z by two 21 cm gaps, covers the polar angle range from 7.5° to 28.0°. The RTD, a single planar drift chamber, covers the polar angle range from 160° to 170°.

Each chamber consists of three layers, two of which are rotated by ±60°, orientated perpendicular to the beam. Each layer is subdivided into cells of 6 sense wires. Test beam measurements gave single-wire resolutions of 120 – 130 μm and a two-track resolution of 2.3 mm.

Sandwiched between the FTD chambers are two Transition Radiation Detector (TRD) modules which are designed to enhance electron-hadron separation on

the energy range from 1 to 30 GeV. Each module consists of a 70 mm thick polypropylene fleece through which carbon dioxide is flushed, followed by a 3 cm thick drift chamber to detect the transition radiation.

The readout electronics of the forward and rear tracking detectors was not operational during 1993. Small sections of the FTD and TRD were read out for test purposes, but there were no data available for physics analysis from either the FTD, RTD or TRD.

2.3 ZEUS Calorimetry

Calorimetry measures the energy of a particle by measuring the energy given out as the particle is decelerated and absorbed by the medium through which it passes. This is a destructive process, since the particle usually loses its identity as it undergoes many interactions with the material of the detector, producing a *shower* of secondary particles. It is the energy of this shower which forms the basis of calorimeter measurement.

The ZEUS calorimeters have been designed to provide complementary information to that given by the tracking detectors. Calorimetry is necessary for the detection of neutral particles, and gives better measurement of high momentum particles in the region where track curvature becomes indiscernible.

Since the ZEUS calorimeter system is almost hermetic, it allows measurement of neutrinos from missing transverse energy in the detector.

2.3.1 The Uranium Calorimeter

The ZEUS UCAL is designed to achieve the best possible energy resolution for hadronic jets.

Electromagnetic energy, from electrons and photons, is easily detected, but hadronic energy may be lost in absorber processes such as nuclear capture. The proportion of energy lost may vary greatly from shower to shower, resulting in a loss in resolution. To overcome this, it is desirable to measure the energy lost due to nuclear absorption in such a way that the response to hadronic and electromagnetic showers is nearly equal. A calorimeter with this property is called a *compensating* calorimeter.

In ZEUS, this is achieved by the use of depleted uranium (U^{238}) as an absorber material. Some of the hadronic energy lost as binding energy is recouped via induced fission of the U^{238} nuclei.

In the UCAL uranium plates, 3.3 mm thick, are alternated with 2.6 mm scintillator plates. The thickness of the uranium and scintillator plates have been optimised to give equal response to hadronic and electromagnetic showers.

Energy from the showers produces light in the scintillator material. The light travels through a wavelength-shifter and light-guide to a photomultiplier (PMT) which converts and amplifies the signal so that it can be read out electronically.

The UCAL is divided into three parts, the central cylindrical BCAL and the two end caps, FCAL and RCAL. The FCAL has a maximum depth of 7.1 nuclear interaction lengths (λ), BCAL, 5.3 λ, and RCAL, 4.0 λ. The FCAL, BCAL and RCAL are each divided into modules, an example of which (from FCAL) is shown in detail in figure 2.3.

The modules are subdivided into 20 cm $\times$ 20 cm towers, segmented longitudinally into electromagnetic (EMC) and hadronic (HAC) sections. The EMC has a length of 1 λ ($\sim$ 25 radiation lengths). Electrons and photons deposit nearly

all their energy in the EMC, while hadrons lose only part of their energy there. Hadrons and electrons can be distinguished by the amount of energy which they deposit in the HAC sections.

The RCAL towers each have one EMC and one HAC section, while the BCAL and FCAL towers each have one EMC section and two HAC sections. To enhance electron position reconstruction the RCAL EMC is subdivided into 10 $cm \times 20$ cm cells, the FCAL and BCAL EMC into 5 $cm \times 20$ cm cells.

Each section has a wavelength shifter, coupled to a PMT, on each side, so that the two sides can be measured independently. Weighting the PMT signals from both sides enhances position reconstruction in the X direction.

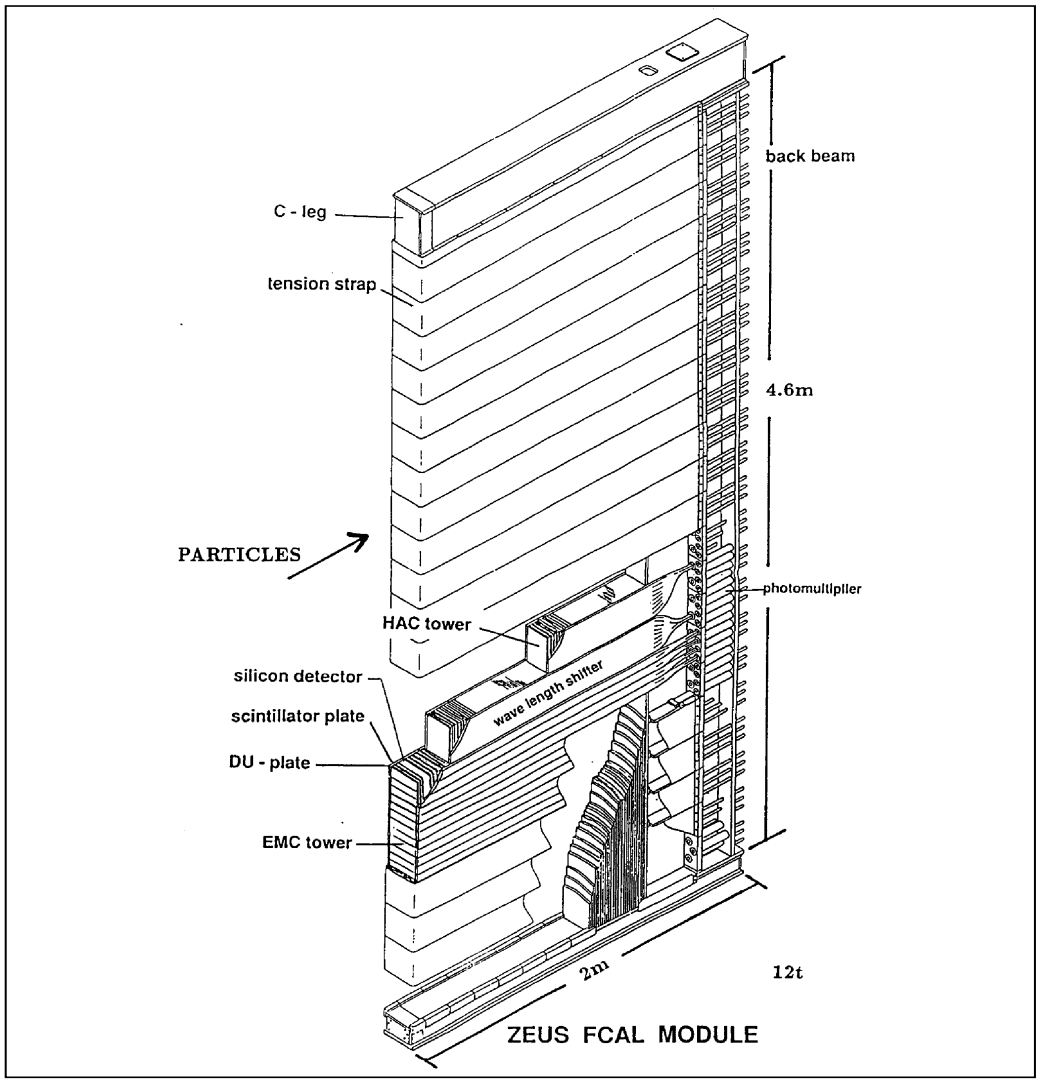

Figure 2.3: *Detailed view of a typical FCAL module and its substructure.*

The BCAL has a polar angle acceptance from 36.7° to 129.1°, the FCAL and RCAL from 2.2° 39.9° and 128.1° to 176.5° respectively.

The plastic scintillator has a fast response time which allows calorimeter timing to be used in the trigger to discriminate between *e-p* collisions originating in the interaction region and background events with upstream or downstream vertices.

The energy resolution of the UCAL is $\sigma(E)/E = 0.35/\sqrt{E} \oplus 0.02$ for hadrons, and $\sigma(E)/E = 0.18/\sqrt{E} \oplus 0.01$ for electrons.

2.3.2 The Hadron-Electron Separator

The HES consists of 3 cm $\times$ 3 cm silicon diodes which can be arranged in one or two planes, and is designed to give improved identification of isolated electrons and electrons within jets compared to that available from calorimeter information alone. The higher degree of granularity offered by the HES improves the segmentation of the calorimeter by an order of magnitude, and discrimination between electron and hadron showers is possible due to the difference in their shower profiles.

Gaps are provided for the HES to be installed after the fourth and seventh scintillator layers in FCAL, and after the fourth scintillator layer in BCAL and RCAL. However, installation was not complete in 1993, and only part of the rear HES was read out.

2.3.3 The Backing Calorimeter

The BAC measures the energy leakage from the UCAL, and also serves as the return yoke for the solenoid. Totally covering the UCAL, it consists of 7.3 cm thick iron plates, between which are 3.7 cm gaps containing proportional counters. The forward region has ten layers, the barrel region, nine, and the rear region, seven.

The BAC has an energy resolution of $\sigma(E)/E = 1.1/\sqrt{E}$.

2.4 Other Components

2.4.1 The Muon Detectors

Muons can be identified by the fact that, at energies greater than 2 GeV, they generally pass through the UCAL and BAC unhindered. They are detected by a system of drift chambers divided, similarly to the UCAL, into three main modules covering the forward (FMUON), barrel (BMUON) and rear (RMUON) regions.

The FMUON was designed to provide independent measurement of high momentum muons in the forward direction, where the particle flux is highest. It has four drift chamber planes, which measure polar angle, alternating with four planes of limited streamer tubes which provide r-ϕ co-ordinates. There are two additional planes of limited streamer tubes covering the region between the main forward part and the BMUON.

The first layer, FMUI, is installed inside the iron yoke between the UCAL and the BAC, while the outer part, FMUO, is installed outside the end cap of the iron yoke. For momentum measurement, the magnetic field from the yoke is complemented by two toroids in front of it, each with an internal field of 1.7 T.

The RMUON and BMUON detectors consist of two layers of limited streamer tubes, one layer (RMUI, BMUI) installed inside the yoke between the UCAL and BAC, the other layer (RMUO, BMUO) outside the BAC, with the magnetised yoke providing the magnetic field for momentum measurement.

2.4.2 The Luminosity Monitor

The LUMI monitor measures the luminosity of the experiment by means of the bremsstrahlung process $e + p \rightarrow e + p + \gamma$, which has the advantages of being precisely understood and having a high cross-section.

It consists of two lead-scintillator calorimeters situated upstream, which detect the outgoing electron and photon in coincidence. Electrons scattered at angles $\theta \leq 6$ $mrad$, with energies between 20% and 90% of the nominal beam energy, are observed in the electron detector, which is situated 34.7 m upstream from the IP, and about 10 cm away from the beam axis.

The photon detector is situated 92.5 m upstream from the IP, very close to the proton beam, since in this process the photons are emitted at angles $\theta \leq 0.5$ $mrad$. A carbon filter shields the photon calorimeter from synchrotron radiation.

In addition to measuring luminosity, the LUMI is used to tag small-angle electrons such as are observed in photoproduction, in which case there is no accompanying photon, and also events in which a photon is emitted from the incoming electron beam.

2.4.3 The C5 Counter

The C5 Counter is a scintillation counter situated near the C5 collimator about 3 m upstream, very close to the beam. Its main purpose is to provide an accurate time measurement for the background in order to veto events which are not in the time window of the electron-proton bunches. In addition the C5 counter detects showers and vetoes these events, too.

2.4.4 The Veto Wall

The veto wall consists of a thick iron block 800 cm wide, 907 cm high and 87 cm thick, the centre of which is situated 725 cm upstream from the IP. Its main function is to absorb background particles coming from the proton beam halo. Both sides are covered with scintillator hodoscopes to detect particles which pass through the wall, and to give signals which can serve as a veto for the main detector components.

2.5 The Trigger and Data Acquisition System

2.5.1 Triggering Conditions at ZEUS

The ZEUS trigger system has the task of selecting a small fraction of events which are of interest for physics analysis from an overwhelmingly large background. Bunch crossings occur every 96 ns, which is equivalent to a rate of 10^7 Hz, while the output rate, determined by the rate at which events can be written to tape, is in the region of $3 - 5$ Hz.

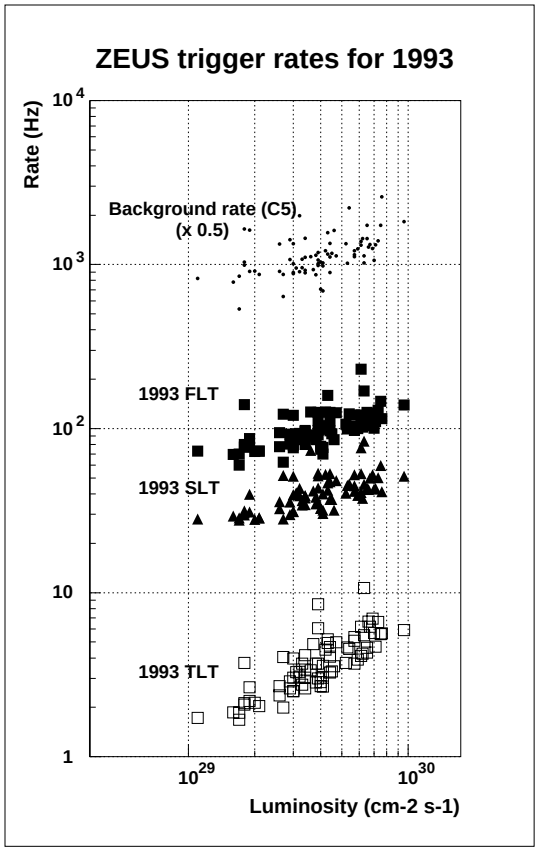

Figure 2.4: *ZEUS trigger rates for 1993.*

The principle sources of background are *synchrotron radiation* from the electron beam, *beam-gas* interactions between the proton bunch and residual gas molecules in the vaccuum, and *cosmic rays*.

Due to the extremely limited time available for deciding whether to accept or reject an event, the trigger system is organised into three tiers, the first level trigger (FLT), which gives a very fast, preliminary decision, the second level trigger (SLT), which uses more sophisticated algorithms to reduce the output rate, and the third level trigger (TLT), which makes the final decision on whether to write out the event. Figure 2.4 shows the rates, versus luminosity, which were recorded during 1993 for the FLT, SLT and TLT, and also for background events.

Each detector component of ZEUS has its own chain of trigger and readout electronics which transfers data to a central data acquisition system.

2.5.2 The First Level Trigger

The FLT requires 4.4 μs to process an event. Since this is considerably longer than the 96 ns between bunch crossings, the data from each bunch crossing are transferred to a 5 μs buffer, known as a *pipeline*, to await a FLT decision.

Each component has its own FLT, a hardware trigger operating on a subset of the full data, which must make a decision within 5 μs of the bunch crossing. The trigger decisions of the components are transferred to the global first level

trigger (GFLT), designed to have a maximum output rate of 1 kHz. If the GFLT decision is positive, digitised data are passed to the SLT.

2.5.3 The Second Level Trigger

The SLT has about 1 ms in which to perform calculations, and uses parallel processing on transputer networks. Compared to the FLT, the SLT is able to use more complicated procedures on a larger range of data variables, enabling rejection of a greater proportion of background events and refinement of the sample of physics candidate events.

For example, the calorimeter SLT compares the arrival time of energy in different parts of the calorimeter (see chapter 6, section 6.3.1) to reject events originating outside the interaction region. The CTD SLT can reconstruct tracks and fit an event vertex, allowing discrimination between events by comparing on-vertex and off-vertex multiplicities.

Again, the component decisions are passed to a global second level trigger (GSLT) which has a maximum output rate of 100 Hz.

2.5.4 The Third Level Trigger

If an event is accepted by the GSLT, data from all components are transferred to the Event Builder (EVB) where it is assembled into a single event record and passed to the TLT for the final trigger processing which reduces the rate from $\sim$ 100 Hz to less than 5 Hz. Using FORTRAN code, the TLT runs a subset of the offline reconstruction program, ZEPHYR, modified where necessary to reduce time overheads.

In addition to reconstruction of data from each subdetector, the TLT analyses the event as a whole and reconstructs kinematic properties such as Q^2, x, y and E_T. It performs a final rejection of non e-p background and classifies e-p events into physics categories according to filters set by the various physics groups.

Chapter 3

The Central Tracking Detector

3.1 Overview of the CTD

3.1.1 Detection of Charged Particles

The ZEUS Central Tracking Detector is a cylindrical gas-filled wire chamber.

The gas ionises along the paths of charged particles passing through the detector, liberating electrons which drift towards the anode, or "sense", wires, while the positive ions are repelled and drift towards the negative "field" wires. Close to a sense wire, "avalance multiplication" of the ionisation electrons occurs, so that a sufficient quantity is collected by the sense wire to produce a measurable signal, or *pulse*, which is recorded by electronic read-out.

3.1.2 The Structure of the CTD

The CTD has nine "superlayers", each composed of eight layers of sense wires, interleaved with layers of ground wires, alternating with field wires.

The superlayers are numbered from 1 (innermost) to 9 (outermost). The wires of the odd-numbered, or "axial" superlayers run parallel to the chamber axis. To aid three-dimensional track reconstruction, the wires of the even-numbered, or "stereo", superlayers are tilted at small ($\sim 5^\circ$) angles, as described in section 3.4.2.

Within each superlayer, the wires are grouped in the r-ϕ plane into drift cells, each centred around a row of sense wires, tilted by 45° with respect to the radius vector.

The CTD has a total of 4608 sense wires, 19584 field wires and 576 cells.

Figure 3.1(a) shows, in a section through the centre of the detector, the arrangement of sense wires in layers and superlayers. Figure 3.1(b) zooms in on a typical cell, showing the full wire layout and the drift paths taken by the ionisation electrons.

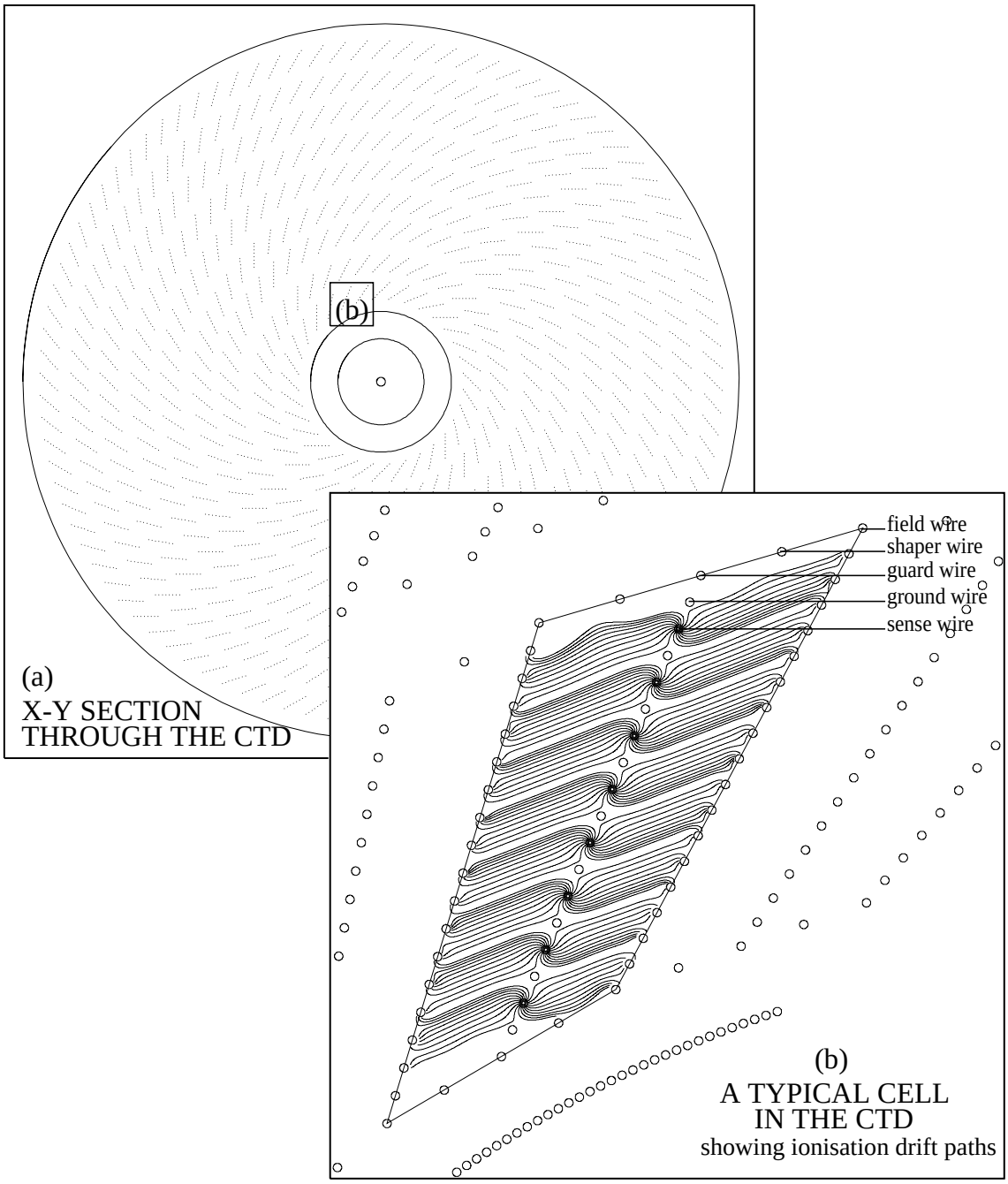

Figure 3.1: *(a) r-ϕ cross-section through the CTD, showing the nine superlayers, each with eight layers of sense wires. The field wires, ground wires and shaper wires are not shown. (b) A detailed representation of the wires in a single cell, and the drift paths of the ionisation electrons.*

3.2 The CTD Drift Cell

The design of the CTD cell was motivated by the following requirements [10].

1. For uniformity of gas gain, surface fields on sense wires must be as equal as possible over the volume of the detector.

2. The electric field must be as uniform as possible over a cell. To a certain extent, any non-uniformity may be compensated by running the chamber so that the drift velocity is operating in the plateau region where variation of velocity with field is at its smallest.

3. The electrostatic forces between wires must be minimized and should be kept below those due to gravity.

4. Some gases, notably those containing hydrocarbons may have a tendency towards whisker growth. In order to minimize this, it is desirable to keep surface cathode fields below 30 kV/cm. [11]

5. Due to the complex layout of the cells, it is important to be able to reduce edge effects between adjacent superlayers as much as possible so that pulses on the outermost sense wires are not effected by the relative alignment between superlayers.

The field planes consist of 19 wires, graded to maintain a constant field across each tapering cell. At each end of the cell two field wires set the maximum negative potential which is then reduced by a constant voltage difference ΔV_f down the field wire plane. The two field planes in adjacent cells combine to produce the drift region, at the centre of which is situated the sense wire plane. This consists of 8 sense wires interleaved with ground wires. The use of the ground wires allow independent adjustment of gain and drift fields and collection of the slowly moving positive ions created in the avalanche at the sense wire. At the end of the cells there are 'shaper' wires to maintain the uniformity of the drift field that would otherwise be impaired by edge effects.

The cells are tilted by 45° with respect to the radius vector. The combined electric and magnetic fields are designed to give a Lorentz angle of 45°, so that the drift of electrons towards the sense wires is purely azimuthal. The tilt of the cells also enables every reasonably straight track coming from the interaction region to cross a sense plane in each superlayer it passes through, so that the first signals arise from close to the sense wire. These close hits typically have drift times of less than the 96 ns interval between beam crossings, enabling a CTD First Level Trigger to identify the correct beam crossing.

Another advantage of a tilted cell is that the left-right ambiguities inherent in the conversion of time to position measurement are greatly simplified, as described in section 3.4.1

3.3 The CTD Readout

3.3.1 Obtaining the Hits

The CTD has two independent systems of readout electronics, the r-ϕ FADC system, connected to all sense wires, and the z-by-timing (ZbyT) system, connected to a subset of the sense wires from the inner superlayers.

The input to the CTD readout is a signal from a sense wire. The output is a measured data point, or *hit*. A hit from the FADC system consists of a drift time and a pulse height, while a ZbyT hit consists of a drift time and a z position measurement. By comparing the FADC and ZbyT drift times, hits can be matched between the two systems.

3.3.2 The r-ϕ FADC System

Every sense wire is connected, at the rear end of the chamber, to an 8-bit Flash Analogue-to-Digital Converter (FADC). Signals from the sense wires are digitised by sampling the signal level (pulse height) every 9.6 ns. The digitisations are stored in a pipeline awaiting a first level trigger decision.

Pipeline data from events accepted by the first level trigger are saved and passed to Digital Signal Processors (DSPs), which analyse the FADC output. First there is a search for "pulse trains", which are groups of 9.6 ns time bins for which the signal has the characteristics expected from the pulses produced by charged particles passing through the chamber. Each identified pulse is then further analysed to determine the pulse height (peak signal level) in FADC counts, and arrival time (chapter 4, section 4.3.3) in 2.4 ns bins. The drift time is given by the arrival time relative to the trigger.

3.3.3 The ZbyT System

All the sense wires in superlayer 1, and the odd-numbered sense layers of superlayers 3 and 5, have additional readout electronics which enable fast determination of z position without the necessity for a track fit. This is vital for first level trigger calculations. It is also essential for the measurement of particles which pass through the CTD at shallow polar angles, leaving hits in only the first superlayer, so that z cannot be determined from stereo-layer information.

The ZbyT system is connected to both ends of the chamber, so that the z position of a hit can be determined from the difference in the arrival time of the signal between the front and rear ends. The drift time is output in 48 ns bins.

3.4 Position Measurement

The trajectory of a charged particle passing through the chamber is reconstructed from positions of the hits it has produced – ideally, one hit for each sense layer traversed.

3.4.1 Measurement in r-ϕ

Knowing the location in r-ϕ of the sense wire, and after calibrating [13] the velocity and orientation of the ionisation drift, the r-ϕ position of each hit is determined by converting the drift time (in ns) to a distance (in cm).

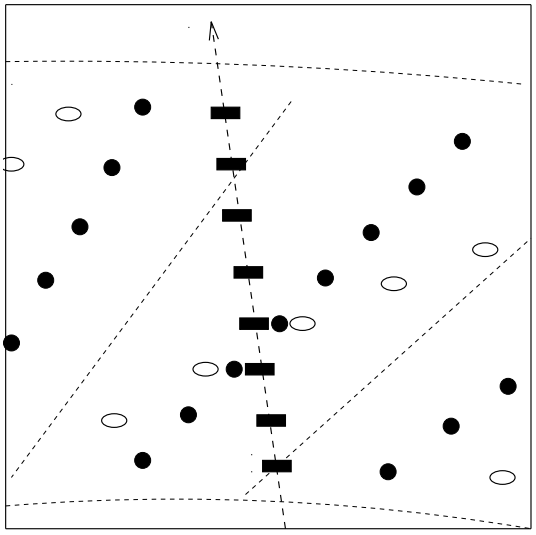

Figure 3.2: *Resolution of the left-right ambiguity within a superlayer. The solid circles represent the sense wires, the solid rectangles, the genuine hits, and the open ellipses, the ghost hits.*

However, since the drift time contains no directional information, there remains an ambiguity as to which side of the wire the hit originated. For each drift time measurement there are two possible position measurements, one the genuine hit, the other a "ghost" hit at the same distance on the opposite side of the sense wire.

The 45° tilt of the cells with respect to the radial direction facilitates resolution of the left-right ambiguity at the pattern-recognition stage of track reconstruction, since fairly straight tracks coming from the interaction region are likely to cross cell boundaries within a superlayer. The genuine hits line up to form continuous segments within a superlayer, and the segments match between superlayers.

The "ghost" segments, however, are broken up within a superlayer if the track crosses a cell boundary, and in any case do not match with segments from other superlayers.

Figure 3.2 shows, in diagramatic form, how the left-right ambiguity is resolved within a superlayer for a track which crosses two cell boundaries

3.4.2 Measurement in z

The stereo superlayers are designed to give precise reconstruction of the z coordinates of hits assigned to tracks. Alternate superlayers (2,4,6,8) are tilted at small angles α ($\approx 5°$) to the chamber axis.

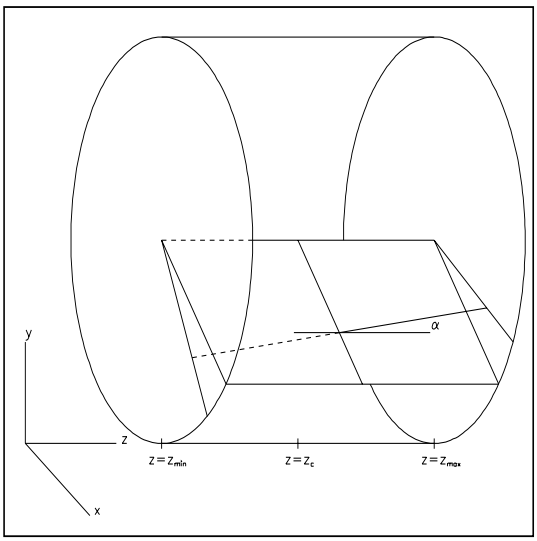

Figure 3.3: *Exaggerated diagram of the stereo angle α.*

A diagram of the stereo tilt is shown in figure 3.3.

Once a track has been identified, and its approximate r-ϕ trajectory discerned from the axial superlayers, its trajectory in z can be determined from the amount by which its stereo-layer segments are displaced in ϕ. Stereo segments have zero displacement at $z = 0$ and maximum displacement at the ends of the chamber at $z = \pm 100$.

To avoid a systematic pulling of the entire track, the wires of superlayers 2 and 8 are inclined by $\alpha \approx +5°$, while those of superlayers 4 and 6 are inclined by $\alpha \approx -5°$.

The z information from the stereo layers is combined, during reconstruction, with any available z-by-timing information.

3.5 Operating Conditions for 1993

3.5.1 Gas Mixture

The CTD design requires a Lorentz angle of 45° to achieve azimuthal drift of ionisation towards the sense wires. The design value of the magnetic field was 1.8 T, for which a planned 50:50 argon-ethane gas mixture was expected to give a Lorentz angle of 45° and a drift velocity of about 50 $\mu m/ns$.

In practice, ZEUS has been operating, to date, with a lower magnetic field of 1.43 T. Due to the reduced magnetic field, it was necessary to modify the gas mixture in order to obtain a Lorentz angle of the required value.

During 1993 a mixture of argon, ethane and carbon dioxide in the ratio 90:8:2 was used, with 0.4% of ethanol added. The resulting Lorentz angle and drift velocity were measured at 44.7° and 47.4 $\mu m/ns$ respectively, which are close to their design values.

3.5.2 HV Levels

The operation of the chamber is extremely sensitive to the surface field (sense wire voltage) level. If it is set too low, the chamber is inefficient, while setting it too high results in excessive noise as well as loss of precision of dE/dx and, ultimately, position measurement, due to FADC saturation.

The surface field was optimised during the initial 1993 running by measuring pulse height and hit-finding efficiency from the first data.

The effect of changes in atmospheric pressure on the gas was found to be an added complication, as the pulse height and consequently efficiency were observed to decrease with increasing atmospheric pressure.

During the early part of 1993 running, the surface field was set at 168.0 kV/cm but it was later increased to improve hit-finding efficiency. Most of the 1993 data was taken with a surface field of 171.5 kV/cm and a drift field of 1.20 kV/cm.

3.5.3 Readout Instrumentation

During the 1992 running period, only the ZbyT instrumentation was complete. Crude tracking was achieved using the ZbyT output alone.

Early in the 1993 running period, the r-ϕ FADC system became fully operational. ZEUS 1993 data therefore contains output from the complete CTD readout. It is the understanding of this first data from the FADC system, and the consequent use of full CTD tracking for analysis of DIS events, which forms the subject of this thesis.

Chapter 4

Understanding the CTD Data

4.1 Systematic Effects on Track Measurement

The CTD became fully operational after the start of the 1993 running period. Physics analysis of the 1993 tracking data, therefore, is inevitably dependent on, and has been taking place concurrently with, the process of learning to understand the detector.

In all its complexity, the CTD is subject to quite a variety of systematic effects which can result in mismeasurement of the positions of hits. Those currently known about exhibit dependences on:

- *track angle*, in r-ϕ and in θ,
- *pulse height*, of saturated pulses and of low, spread-out pulses,
- *multi-hit interference* when there are two or more hits on the same wire,
- *edge effects*, in regions of non-uniform E-field, such as at the ends of cells, and in the immediate vicinity of sense wires, guard wires and shaper wires,
- *position in the CTD*; variations in Lorentz angle, drift velocity, and drift in the z direction [12].

Systematic mismeasurement can result either in hits being wrongly excluded from the track, or in the overall track measurement being systematically altered. This can mean that tracks are wrongly excluded from the main event vertex.

It is possible for hit position measurement to go wrong at two stages.

The first is when the arrival time is obtained from the raw FADC pulse train. Arrival time can be mismeasured when the pulse shape is different from that expected, i.e. when the build-up of ionisation at a sense wire takes place in a different manner to that assumed by the hit-finding algorithms. This effect is described in section 4.3.3.

The second is when time is converted to distance. Distance can be mismeasured when the ionisation travels either by a different path or at a different velocity to that assumed. This is discussed in section 4.7.3.

Calibration of time-zero, drift velocity and Lorentz angle is discussed elsewhere [13]. Out of the effects itemised above, those investigated in this thesis are

- *track angle effects* in r-ϕ, when the track makes a shallow angle with respect to the drift direction of the ionisation,
- *pulse height* and its relation to pulse shape, particularly concerning small spread-out pulses and large pulses which saturate the FADC,
- *edge effects* at the ends of cells, where ionisation can be split between two cells, and
- *multi-hit effects* – a focus on multiple hits, whether genuine (as caused by two close tracks) or spurious, resulting from irregularly-shaped single pulses, or from noise.

4.2 Data – 1992 and 1993

Some of the studies described in this chapter utilise the first available data obtained from the CTD FADC system in autumn 1992, while others are based on data obtained during the 1993 running period. These studies are complementary.

In 1992 only a limited amount of data was available, but it contained complete information about the signals received by the FADCs. In 1993, the chamber was fully instrumented with FADCs for almost the entire run period, but the volume of data made it impractical to output detailed pipeline information for analysis. Instead, hit parameters were output after online processing by DSPs; the small fraction of complete FADC pipelines which were output for test purposes proved unsuitable for detailed studies, since they were selected randomly and many did not even contain pulses.

The 1992 data, therefore, is suitable for looking at pulse shape and hit quality, but nothing more than basic tracking, since only a small part of the CTD, corresponding to a limited range in ϕ, was instrumented with FADCs, and this for only a short period. By contrast the 1993 data is excellent from the point of view of detailed studies of tracking systematics, but, compared to the 1992 data, contains limited hit information.

4.2.1 Selection of 1992 data

The data used here is from run 4163, the largest physics run taken during the period in which the CTD was instrumented with FADC readout.

Run 4163 consisted of 86480 raw events, of which 8131 were written to DST. From these, 5068 were selected on the basis of the TSTAM11 physics cuts (accepting any kind of physics event), after which a final selection was made of events which had four or more FADC hits. This left 2745 events in the final sample. From each event, only wires which had a single FADC hit were selected for study.

4.2.2 Selection of 1993 data

The data used for the tracking studies described in this chapter consists of a subset of the 1993 ZEUS DIS data, selected according to the criteria outlined in chapter 6, section 6.3. It was unnecessary to use this dataset in its entirety, and certainly impractical; for a study such as this, involving the individual hits on tracks, the data volume would have been unmanageable. What is used here is therefore a subset of 2500 events, taken during October 1993 during a period of very smooth operation of both HERA and ZEUS. No further event selection cuts were imposed, but from each event only the longest tracks were selected – those passing through a minimum of eight of the nine CTD superlayers. This was to ensure that quantities such as residuals of hits and curvature of tracks were reasonably well measured. An explicit cut on the number of hits on a track was

avoided since, for reasons discussed in section 4.7.5, this would have introduced a selection bias against negative tracks.

4.2.3 Monte Carlo Simulation of the CTD

The official ZEUS Monte Carlo, MOZART [14], uses GEANT [15] to propagate the products of electron-proton collisions outwards from the interaction point, fully simulating interactions with material in the detector and magnetic field effects.

In the CTD, whenever a charged particle crosses a drift plane a hit is produced on the appropriate sense wire. A pulse height is obtained, using a simple conversion factor, from the energy loss of the particle as given by GEANT. The drift time is allocated according to the planar drift approximation, (section 4.7.3). Random Gaussian smearing is applied to the pulse height and drift time. The hit parameters are then digitised so as to appear in an identical form to that obtained from the readout electronics of the detector, and thus the same reconstruction software can be used for Monte Carlo output as for real raw data.

The drift of ionisation to the sense wire is not fully simulated, nor is the avalanche, the build-up of a pulse, nor the operation of the hit-finding software on a pulse train. Therefore the Monte Carlo does not describe effects which depend on pulse shape or those involving deviations from the planar drift approximation – i.e. most of the effects discussed in this chapter.

The Monte Carlo does simulate the hit-finding inefficiency that results when two hits are close together on the same wire. Where appropriate, the second hit is deleted. There is also simulation of a general, random hit-finding inefficiency throughout the chamber. An available option for simulation of random noise hits is not presently used, so that all CTD hits are "genuine", associated with charged particles passing through the chamber.

The Monte Carlo data referred to in this chapter is a 1000-event subset of the simulated deep inelastic scattering events with $Q^2 > 4GeV^2$ used for acceptance corrections in the analyses of chapters 7 and 8. A more detailed description of this dataset is given in chapter 6.

4.3 Looking at Pulses with 1992 FADC Pipelines

4.3.1 Offline Emulation of the DSP

The 1992 ZEUS data used for physics analysis, contains tracking information from the CTD z-system only, since the r-ϕ FADC system was not operational at that time. However, during September 1992 a segment of the CTD was instrumented with FADC readout for test purposes.

As described in chapter 3, the FADC signals from each sense wire are processed by an online DSP, which establishes whether, according to a set of eligibility criteria, they constitute a pulse (or possibly more than one pulse), and, if so, determines the height and position of the peak(s). However, the online DSPs were not in use at that time. Instead, the entire FADC pipeline data was written to tape, the hits being found at a later stage by an offline emulation of the DSP code [16], contained within the reconstruction software [17].

The FADC pipelines are written out in the form of a bitpacked table containing an entry for each wire. With this table as input, the offline processing loops over all the wires, in the following procedure:

1. The pipeline data for a given wire is unpacked into an array of digitised signals in FADC time bins – a *pulse train.*

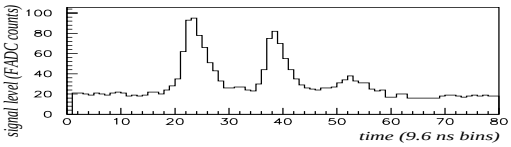

2. The pedestal value is subtracted from the signal. At this stage, if offline filter parameters have been set, the digital filtering is implemented. [18]

3. The signals are checked against the pulse-recognition criteria. Where pulses are identified, values are obtained for their size and drift time, and entered into a table for FADC information obtained offline.

4. This is combined with data from the z-by-timing system, filling a table of CTD hits. This table forms the basis of the CTD track reconstruction, which proceeds from here on independently of whether the FADC data was obtained from online DSPs or via offline processing.

4.3.2 Pulse Height and Integrated Pulse Size

Proportionality of Height and Integrated Size

With the full FADC pipeline data it is possible to investigate the relationship between pulse height and integrated size. The height of a pulse is the height of a single FADC bin which contains the peak, and this measures the ionisation early in the pulse. The pulse integrated size measures the total ionisation in the pulse, obtained by summing the signals in all the FADC bins from the point at which the pulse first rises above the threshold, to the point at which it falls back below the threshold. Normally the pulse height is expected to scale with its area.

Why Use Pulse Height?

The DSPs could output pulse area as easily as pulse height, and it would seem that the area would provide a more direct measurement of dE/dx. However, there are drawbacks. Accurate height measurement is possible as long as there is a relatively clean rising edge, whereas area measurement can be affected by noise fluctuations anywhere along its entire length, so there is a much greater chance for things to go wrong. Particularly in the case of overlapping hits on a wire, the height of the first pulse is usually measured accurately, whereas, working with areas, it would be impossible to disentangle the signal associated with the first pulse from that associated with the second.

Results from the ZEUS 1992 data

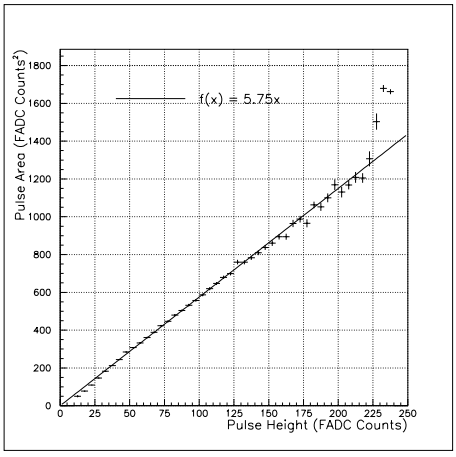

Figure 4.1: *Area versus height of FADC pulses, with superposed linear fit.*

To ensure the reliability of dE/dx measurement based on pulse height, it is necessary to check that the heights of pulses from the ZEUS CTD FADC system do scale with their areas. Figure 4.1 shows that on average the height and integrated size of a pulse are indeed proportional, scaling by a factor of 5.7. However, very small pulses and very large pulses appear to deviate from the linear relationship. For very large pulses this is to be expected since the FADCs saturate at 255 FADC counts, corresponding to a height of about 235 FADC counts for a pulse rising from the pedestal (noise) level. Since the heights of these large pulses are truncated, the height is less, in proportion to the area, than for unsaturated pulses.

For small pulses the situation is more complicated, resulting from a combination of factors. Pulse shape, and hence the relationship between area and height, can change depending on the position of the hit within the drift cell (described below), and on the angle of the track (section 4.7.5). It is also affected when a second pulse is superposed on the tail of a previous pulse (section 4.4).

A significant cause of reduction in pulse height, seen in figure 4.2, is the splitting of the ionisation between two cells, when a track passes close to a cell boundary.

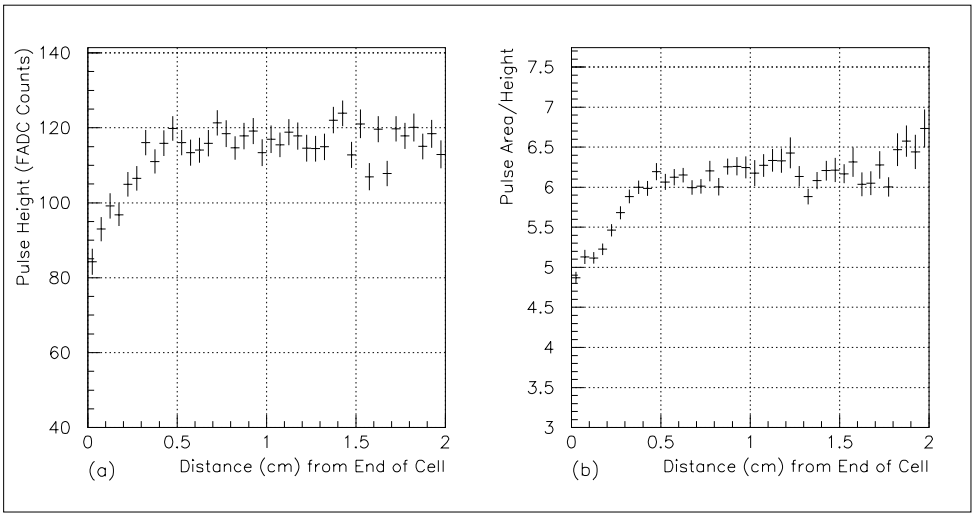

Figure 4.2: *(a)Pulse height versus distance from the cell boundary. (b)Integrated pulse size/pulse height versus distance from the cell boundary*

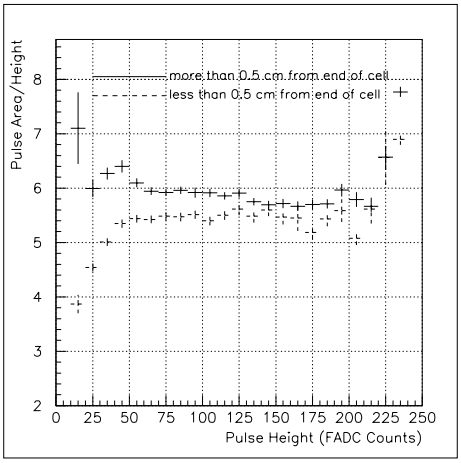

Figure 4.3: *Pulse area/height versus height.*

Figure 4.2(a) shows a marked fall-off in pulse height for hits within 0.5 *cm* of the edge of a cell. In addition, the area decreases with respect to height, as shown in figure 4.2(b), indicating a change in pulse shape. Figure 4.3 shows that the decrease in area/height seen for small pulses seen in figure 4.1 is largely due to the effects of hits near the cell boundaries. For pulses more than 0.5 *cm* away from the edge of the cell, the ratio increases for small pulses, a possible indication of loss of height due to the spreading out of ionisation

4.3.3 Pulse-Shape Dependence of Time Measurement

Changes to the shape of a pulse have implications not only for dE/dx measurement but also, if the rising edge is affected, time, and hence position measurement.

The FADC pipelines are stored in time bins of 9.6 ns. From these the DSP obtains a measurement of the arrival time, in bins of 2.4 ns, by using the Constant Fraction Discriminator algorithm [19], which interpolates between the two bins in which the signal level is either side of a constant fraction (currently set at 0.16) of the difference between the trough and peak signals, thus estimating the time at which the pulse reaches 16% of its peak height.

This method assumes that the rising edge of the pulse has a uniform gradient, and that the base level is flat. If this is not the case, then the arrival time of the pulse may be overestimated or underestimated.

4.4 Multi-Track Interference

4.4.1 Two or More Hits on a Wire

Even with such rudimentary tracking as was possible with the 1992 FADC data, there were some striking qualitative differences observed between hits assigned to tracks and those left off tracks. The pulse heights of hits on tracks had a Landau-type distribution, with a peak at about 50 FADC counts, which is roughly equivalent to a minimum ionising particle. By contrast hits left off tracks tended to have low pulse heights, so that their distribution was peaked towards zero.

It was also apparent that single hits or first hits on a wire were twice as likely to be put on tracks as second or subsequent hits.

One explanation was that the majority of hits with small pulse heights that were left off tracks were due to noise, or resulted from the break up of the tail of a larger pulse. The other, more worrying, possibility was that second hits on a wire, whose pulse heights are generally reduced, were being systematically excluded from tracks due to position mismeasurement (section 4.4.2).

4.4.2 Systematic Mismeasurement of Second Hits

When the trajectories of two or more charged particles passing through the CTD become sufficiently close together, their ionisation mingles. When it reaches the sense wire, a confused signal is picked up by the FADC, the tail of one pulse overlapping with the rising edge of another. The second pulse may be lost completely.

The DSP algorithms which calculate the height and arrival time of the FADC pulses assume an "ideal" pulse – one which rises very steeply from the base level to a well-defined peak, then falls slowly back again to base level, with a long "tail". When pulses overlap, the situation is obviously much less straightforward than for single isolated pulses, giving rise to errors in measurement, particularly for the second or subsequent pulses.

Reasons for Time Mismeasurement

As explained in section 4.3.3, the arrival time of a pulse is calculated using the Constant Fraction Discriminator method, which is sensitive to pulse shape. When the rising edge of a second pulse is superposed on the downward tail of a preceding pulse, the gradient of the rising edge of the second pulse is underestimated, causing the arrival time to be overestimated.

Reasons for Pulse Height Mismeasurement

The pulse height is measured as the difference between the peak of the pulse and the preceding trough. If there is no preceding pulse, the trough level is that of the background level, or *pedestal* offset. However, for second or subsequent pulses,

the trough is some point on the falling tail of the preceding pulse, and if this is significantly higher than the pedestal, then the second pulse will be measured to have a lower height than it should. A possible alternative would be to use the *baseline to peak* measurement, i.e. the difference between the peak and the pedestal. However, this would cause the second pulse height, sitting on the tail of the previous pulse, to be overestimated.

4.4.3 Creating Artificial Double Pulses

By adding together the signals from two FADC pipelines, each containing a single pulse (subtracting the pedestal from one pipeline), it is possible to artificially create a double pulse. Running the hit-finding software first on the two original pulses separately and then on the "double pulse", the sizes and times of the two hits when they are found separately can be compared with their values when measured as two components of a double pulse, giving some idea of the systematic shifts in these values for second and subsequent hits. By this means it is also possible to determine the efficiency with which the two pulses are resolved, and how this varies with the distance between them.

Previous Studies

This method of overlaying single pulses to simulate the effects of double pulses was used in the Centaur Test Chamber [19], and possible parametrisations of corrections to the size and timing were considered. The effect of digital filtering was investigated. It was found to improve the two-hit resolution [19],[18], but with the drawback that it gave less accurate dE/dx information.

Pulse Quality Criteria

In order to minimise contamination of the initial single-pulse sample by unresolved double pulses, a selection requirement was made for this study that

(a) there should be no glitches in either the rising or falling edge of the pulse, and

(b) the pulse tail, once having fallen below the threshold, should not rise above the threshold again by more than a given (input) value.

Saturated pulses were accepted.

4.4.4 Adding the Signals from Two Pulse Trains

The following method was used to overlay pulses:

First the FADC hits were found by running the offline pulse analysis as described in section 4.3.1. For each pulse which satisfied the criteria of section 4.4.3, the time and size measurements, as given in the offline hit table, were recorded,

referenced to the number of the wire on which the pulse was found. The offline hit table was then emptied.

For each selected wire, the pulse train signals from each single pulse were added bin-by-bin to the signals from a stored pulse train on the same wire from a previous event, subtracting the pedestal from one pulse so as not to double the noise level, and this produced a modified train containing a double pulse.

The unmodified pulse train was meanwhile stored, overwriting the previously stored train, and ready to add to the next single pulse to occur on the same wire in a future event. (If no train had been previously stored for that wire, the train from the current event was simply stored for future use, with no double pulse created.)

The modified train containing the newly-created double pulse was reinserted into the offline pulse analysis chain and thence into the offline hit table, so that eventually each event had a new offline hit table filled with the hit parameters obtained from the artificially created double pulses.

So now, after the initial offline hit-finding, for each wire containing a selected hit the processing steps are:

The pulse-train signals are added bin-by-bin to those of a stored pulse from a previous event.

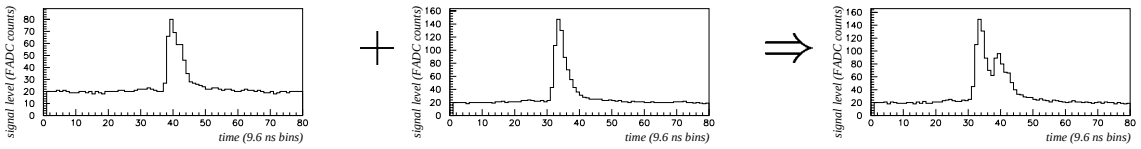

Pedestal subtraction and, if required, filtering, take place as before.

The hit-finding software looks for the pulses, either resolves or fails to resolve the two hits, obtains their (altered) time and size value(s), and refills the offline hit table.

The hits obtained from the simulated double pulses were analysed to determine, firstly, whether the algorithm successfully resolved the two pulses or found just one, i.e the *two-pulse resolution.* In the cases where two hits were found, the *input* values of size and drift time from the two single pulses were compared with the *measured* values from the double pulse.

This procedure of overlaying pulses was first undertaken with unfiltered pulses, then repeated with the addition of an offline algorithm to simulate the effects of a digital filter, and the two sets of results were compared.

4.5 Results Obtained from Overlaid Pulses

4.5.1 Two-Pulse Resolution

The two-pulse resolution can be defined as the separation time for which the pulse-finding algorithm is 50% efficient at resolving the two pulses. The probability for both hits to be found clearly depends on the separation of the pulses, and it also depends on their relative sizes. (A small pulse may be seen as a slight glitch on the tail of a preceding large saturated pulse, even when they are quite far apart.)

Figure 4.4(a) shows how the probability that both hits are found (i.e. the two-hit resolution efficiency) varies with the time interval between the input pulses, for unfiltered and filtered pulses. The two-hit resolution efficiency reaches 50% when the pulses are separated by about 50 ns. This corresponds spatially to a two-track resolution of about 2.5 mm, and agrees with previous results from the Centaur test chamber. At separations of 125 ns or more, the two-hit resolution efficiency is about 100%. These values do not appear to be changed by the use of the digital filter. The resolution efficiency is slightly improved when the pulses are less than 50 ns apart, but slightly worse when they are between 50 and 125 ns apart.

In figure 4.4(b) the effect of the height ratio of the input pulses is examined. If the height of the second pulse is less than half that of the 1st, then there is less than a 50% chance of the two hits being resolved, at time separations of less than 125 ns. The digital filter seems to give an improvement when the 2nd pulse is larger than the first, but gives a slightly worse result when the 2nd pulse is smaller.

4.5.2 Effects on Time Measurement of the Second Pulse

As described in section 4.4.2, the measured arrival time of a second pulse is expected typically to be later than its true arrival time. The results obtained from overlaying pulses, shown in figure 4.5(a), appear to confirm this. When the pulses are separated by 150 ns (a distance of about 7.5 mm), or more, the time measurement of the second pulse is not significantly affected. As the pulses get closer together, the shift in arrival time becomes increasingly large; pulses 50 ns (2.5 mm) apart are typically measured 3 ns late, corresponding to a spatial error of 150 μm. Pulses closer together than 50 ns are unlikely to be resolved.

Using the digital filter appears to have an adverse effect; the mismeasurement at 50 ns separation becomes 5 ns, corresponding to 250 μm.

Plotting the shift in arrival time against *input* pulse separation is interesting, but not useful in the context of considering a possible correction to the data, since only the *measured* separation of the two hits is known. This value already has the time mismeasurement of the second hit folded into it. Figure 4.5(b) shows the shift in time measurement in relation to the *measured* pulse separation. Figure 4.6 shows how the shift in time measurement varies with the *measured* height ratio of the second pulse to the first.

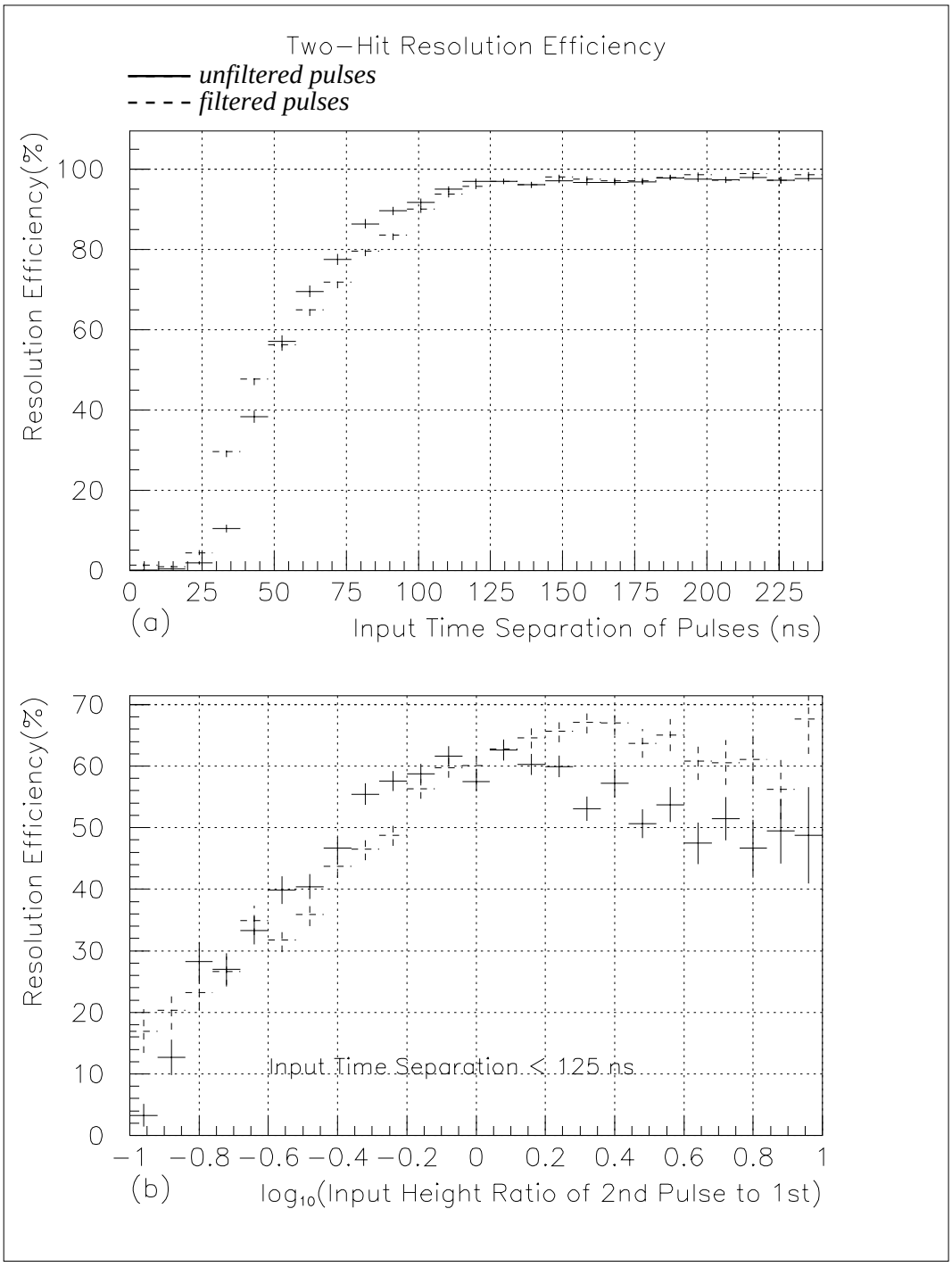

Figure 4.4: *(a) Two-hit resolution efficiency, plotted against the time interval between the input single pulses, comparing unfiltered and digitally filtered pulses. (b) Two-hit resolution efficiency for pulses separated by less than 125 ns, plotted against the height ratio of the input 2nd pulse to the 1st, comparing unfiltered and filtered pulses.*

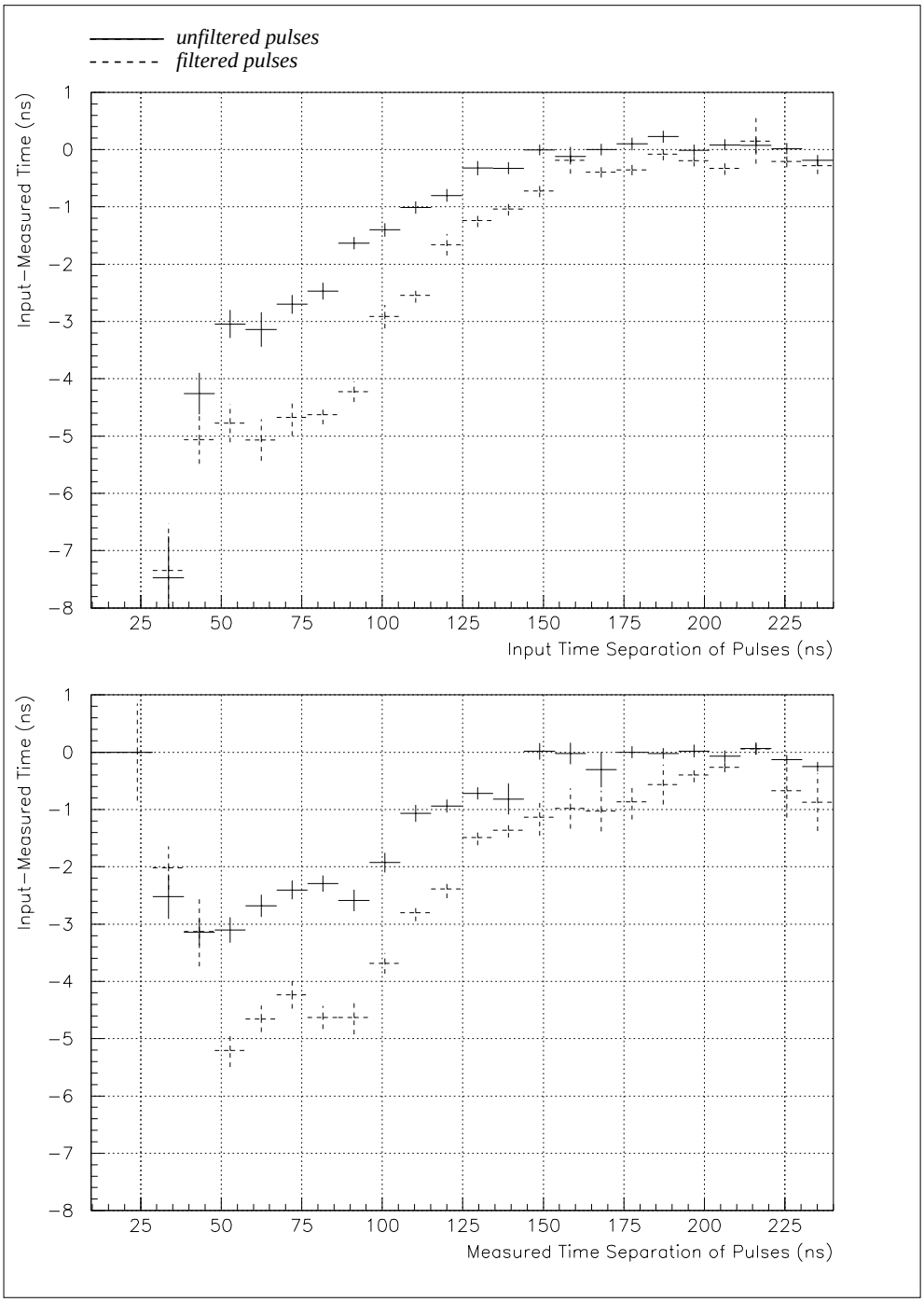

Figure 4.5: *Input-Measured time of the second pulse, (a) versus* input *separation, and (b) versus* measured *separation between the first and second hits, using unfiltered and filtered pulses.*

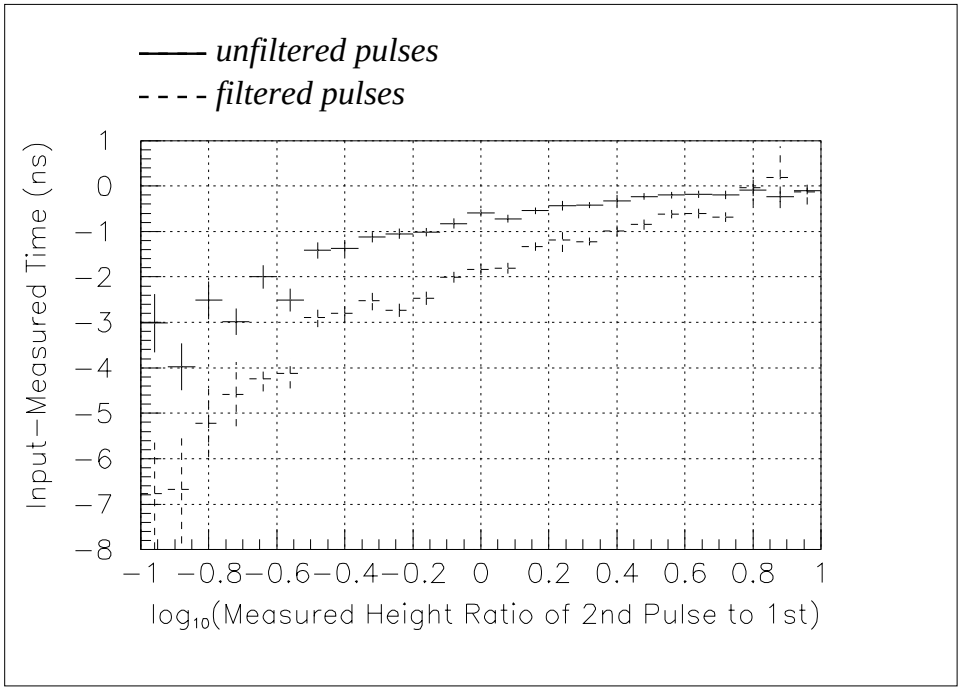

Figure 4.6: *Input-Measured time of the second pulse, versus* measured *height ratio of the second pulse to the first, using unfiltered and filtered pulses.*

4.5.3 Effects on Height Measurement of the Second Pulse

If a second pulse arrives before the signal from a previous pulse has returned to base level, measurement from the preceding trough to the peak tends to underestimate the height of the second pulse (section 4.4.2). The results obtained from overlaying pulses indicate that this can be by as much as 40 FADC counts when the pulses are 50 ns apart. The magnitude of the shift falls exponentially as the pulse separation increases; it is quite small for pulses separated by 150 ns (7.5 mm), and negligible for pulses 200 ns (1 cm) apart. At intervals greater than 200 ns the tails of all but the very largest pulses will have died away.

If second hits are to be included in dE/dx studies, these shifts will have to be corrected. As shown in figure 4.7(a), a simple exponential curve fits the data quite well, in this case $e^{5-0.027x}$, x being the measured pulse separation. A second pulse will also be affected by the size of the preceding pulse.

Normally there is no way of knowing the true height ratio of the two pulses, so corrections must be based on their measured height ratio which has already folded into it the mismeasurement of the second pulse. Figure 4.7(b) shows how the input-measured height of the second pulse varies with height ratio.

It appears in figure 4.7 that the effect is less pronounced when the digital filter is used. However it must be remembered that a pulse height measured after digital filtering tends to be less representative of the dE/dx than an unfiltered

pulse height measurement, so probably even here there is no net advantage.

Figure 4.8(a) shows how the shift in height measurement of the second pulse varies with respect to the height ratio of the two pulses after the correction function shown in figure 4.7(a) has been applied to remove separation-dependent effects (using unfiltered pulses). A linear correction, $-7x$, is shown, where x is the measured $log_{10}(2nd\ height/1st\ height)$. Applying this, in addition to the previous correction, gives figure 4.8(c). Compared with the uncorrected *input-measured* height distribution of figure 4.8(b), it can be seen that the mean has been moved to close to zero, and the *rms* has been reduced from 20.2 to 15.5 FADC counts.

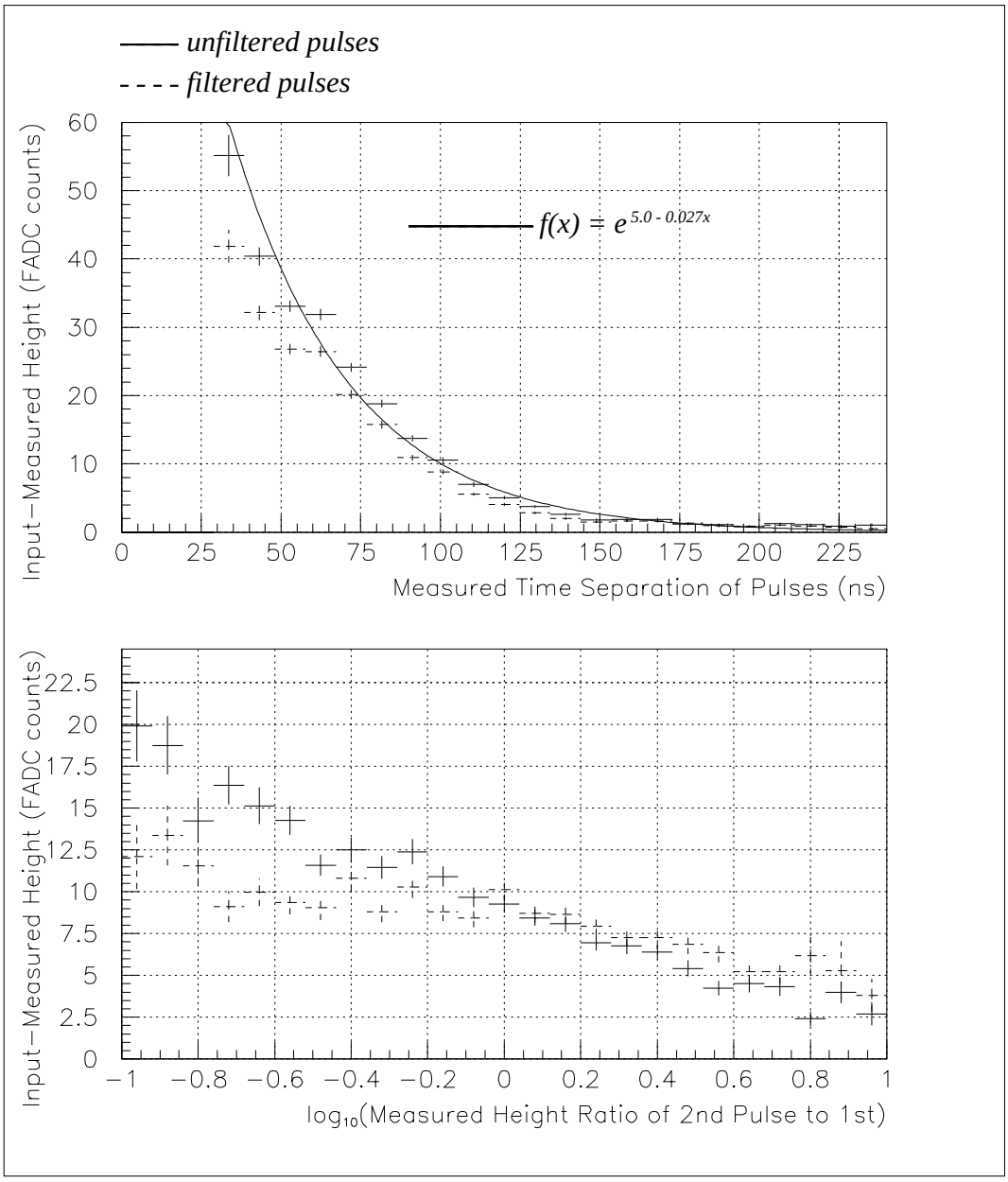

Figure 4.7: *Input-measured height of the second pulse, with unfiltered and filtered pulses, (a) versus* measured *separation of the first and second hits, with a superposed correction function, and (b) versus* measured *height ratio of the second pulse to the first.*

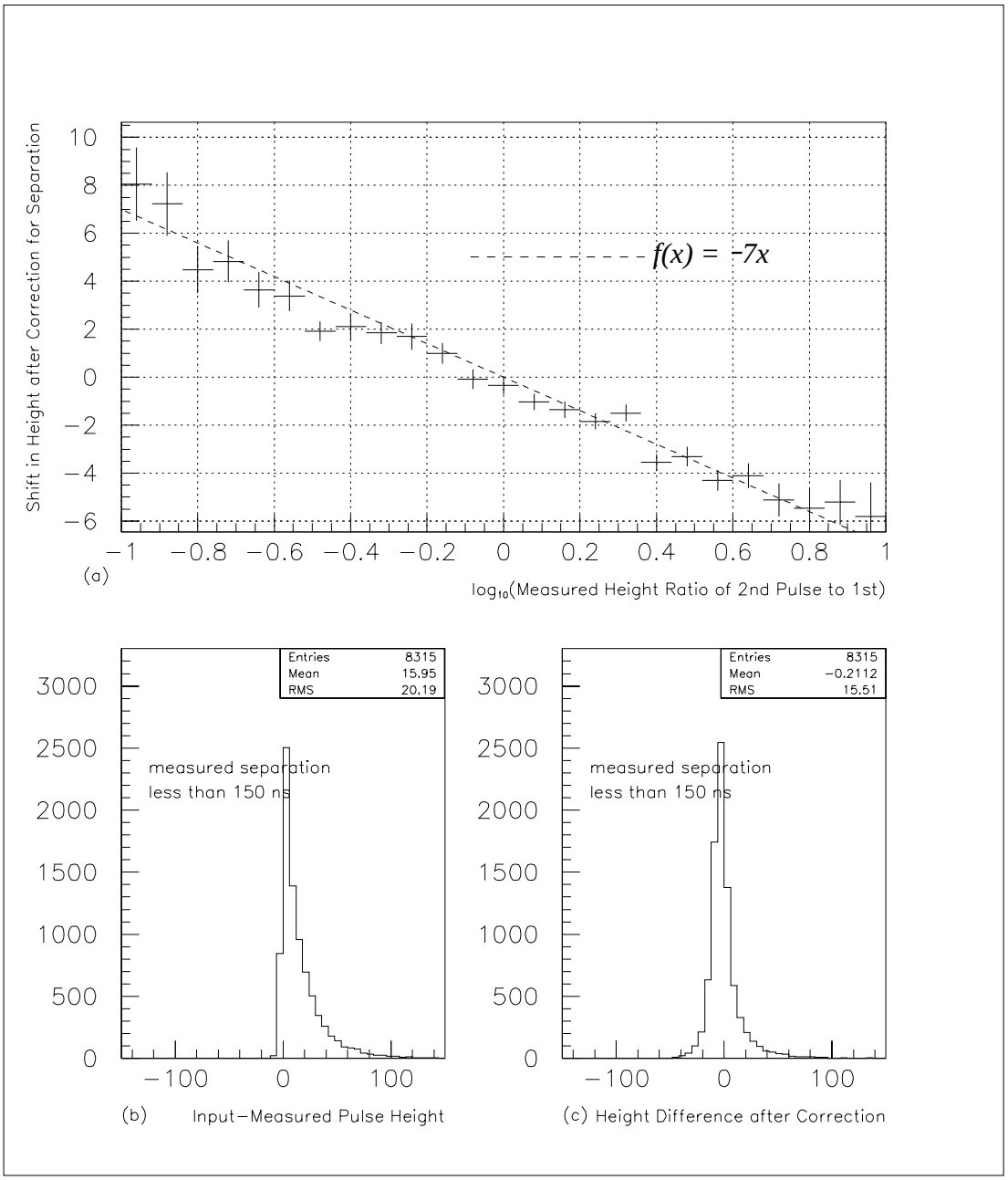

Figure 4.8: *(a) Unfiltered input-measured height of the second pulse, after having been corrected on the basis of pulse separation as shown in figure 4.7(a), versus log_{10} of the* measured *height ratio of the second pulse to the first, with superposed correction function.*
(b) Uncorrected input-measured height of the second pulse for hits separated by less than 150 ns, for unfiltered pulses.
(c) Input-measured height of the second pulse, after correction on the basis of both pulse separation and height ratio, for unfiltered pulses separated by less than 150 ns.

4.6 Summary of Results from 1992 FADC Pipelines

- For FADC pulses from the ZEUS CTD, height is on average proportional to integrated size. However this is not true for saturated pulses nor for very small pulses.

- For pulses close to cell boundaries, there is a reduction in both height and integrated size, and a loss of proportionality between them.

- Overall, the two-hit resolution efficiency is 50% when the pulses are 50 ns apart, for both filtered and unfiltered pulses. This is the design value of the CTD.

- When two hits are close together the measurement of a second or subsequent hit can be considerably affected by the tail of the previous hit. In general, the measured height of the second pulse is smaller than its true height, while the measured arrival time is later. For pulses separated by about 50 ns (2.5 mm), arrival times are typically measured 3 ns late (150 μm), and pulse heights at typically 35 FADC counts below their true value. These effects decrease in magnitude the further apart the pulses are; the systematic effects on pulses further apart than 150 ns (7.5 mm) appear to be very small.

- The effect of the digital filter is somewhat complicated, and appears to actually aggravate the time mismeasurement of 2nd hits. Its effect on the two-hit resolution is mixed. The results seem to differ from those obtained with the Centaur test chamber, possibly due to sensitivity to pulse shape, given the irregular nature of many of the pulses found in the CTD. All tracks in the Centaur test chamber had the same angle of incidence and the magnetic field was zero. It should be noted that in this study the filter parameters used were those obtained from work with the Centaur test chamber; they were not reoptimised for the CTD. However, other studies with the digital filter indicated that it would be extremely difficult to obtain a sufficiently uniform scaling of pulse height to permit dE/dx work [20], and it was decided not to use online digital filtering for the forseeable future.

- It is possible to apply corrections to the height of the second pulse, based on the separation between the pulses, and the height ratio of the second pulse to the first. These appear to get rid of the systematic shift in measured height, bringing the *input-measured* mean closer to zero and having some effect in reducing the rms.

4.7 1993 DSP Data – Systematic Effects Seen in Residuals

In June 1993 the FADC instrumentation of the CTD was completed, and full r-ϕ information from all nine superlayers became available for the first time. Studies of r-ϕ residuals from long tracks revealed a variety of systematic shifts in the positions of hits [21], [22]. Those described below are now corrected for offline, and have been incorporated into the latest version of the official ZEUS Monte Carlo.

The residual of a hit is the difference in position between the track fit and the hit measurement. Long tracks are used because they are pulled less by a badly-measured hit, i.e. the measurement of a track passing through many superlayers is expected to be reliable. Thus if the position of an individual hit is a significant distance from the track, then it is likely that it is the hit position, rather than the track position, which has been inaccurately measured.

The sign convention used here for residuals is that they are positive if the hit and the wire are both on the same side of the track, negative if the hit is on the opposite side of the track from the wire. This means that underestimation of the arrival time (or drift distance) produces a positive residual, while overestimation gives a negative residual.

4.7.1 Correcting for Systematic Effects

Offline corrections for the systematic effects described below have been implemented in the most recent track reconstruction software. The correction functions used are obtained from empirical parametrisations of the effects seen in the data. They are chosen to be simple in form and well-behaved at the extremities of the range to which the correction is applied. It was decided that, at this stage, corrections should be aimed at reducing the magnitude of any systematic shifts in the residuals to less than 100 μm [21].

4.7.2 Pulse Height Effects

The residuals show a noticeable dependence on pulse height, as is seen in figure 4.9(a). There are two effects here. The largest pulses ($\sim$ 235 FADC counts, after pedestal subtraction) which are likely to be saturated, have a positive shift of more than 100 μm in their mean residual. At the other end of the scale, the residuals of the smallest pulses can have a negative shift of 300 μm or more.

Saturated Pulses

When a FADC pulse saturates, there is no way of knowing the true height of the peak, as it is truncated at 255 FADC counts.

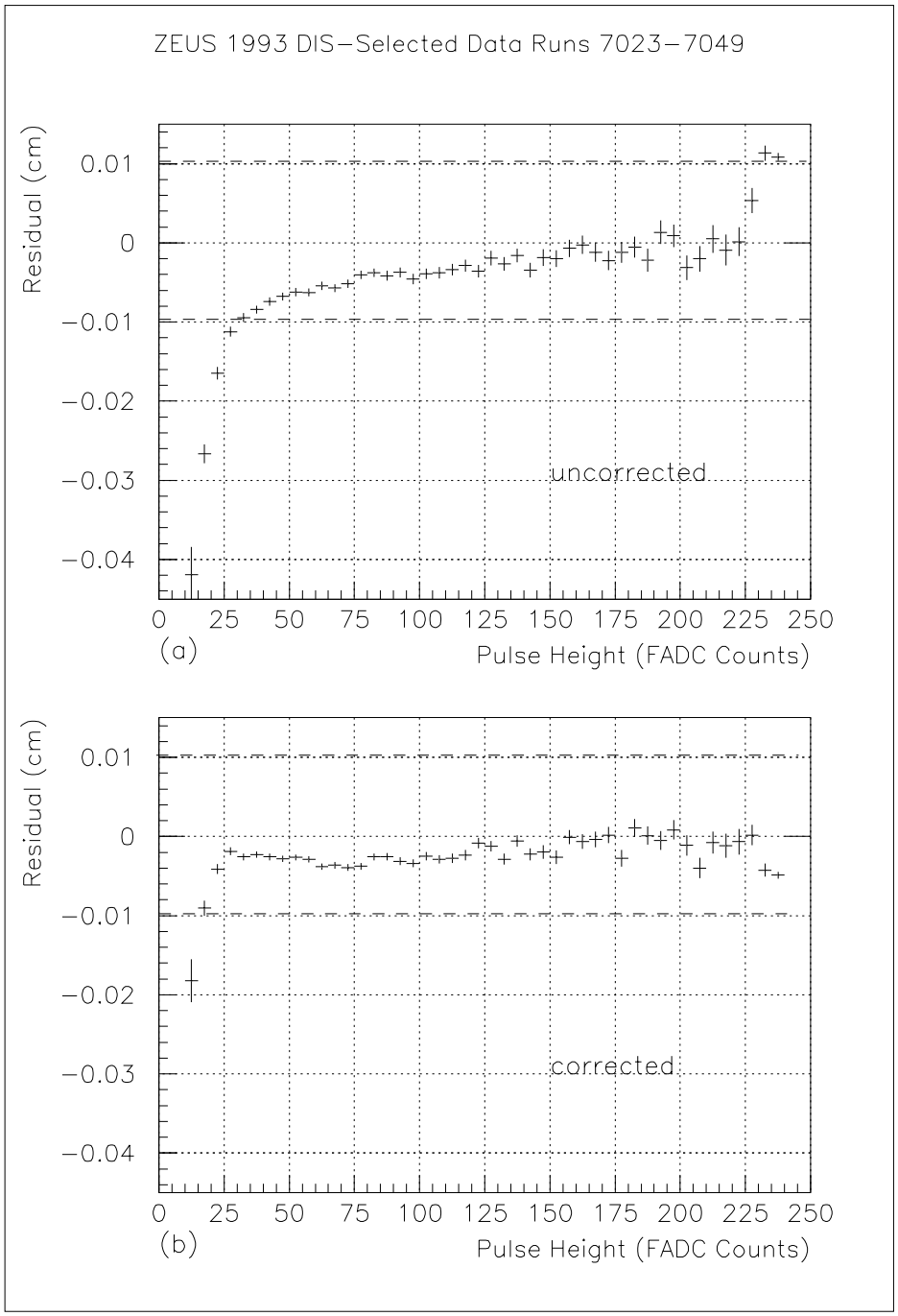

Figure 4.9: *Residual versus pulse height, (a) uncorrected, (b) corrected. The horizontal dashed lines show the target range of* ± 100 μm.

Moreover, if more than one FADC bin is saturated, it is impossible to determine the true position of the peak, or the gradient of the rising edge, since all saturated bins are the same height.

The FADC time bin containing the measured peak is the first saturated bin, while the true peak may be several bins later. The measured arrival time therefore tends to be less than the true arrival time, and this is seen in figure 4.9(a) as a positive shift in the residuals of very large pulses.

Small Pulses

Figure 4.9(a) also shows a systematic negative shift for very small pulses, implying that the measured arrival time is later than the true arrival time. The situation regarding small pulses is not simple. There are direct and indirect reasons for their measured arrival time to be late.

The indirect factors tend to reduce pulse height and at the same time lengthen distance measurement, producing hits with small pulse heights and a negative residuals. Probably the largest contribution is from hits near cell boundaries, where the drift velocity appears to be reduced (section 4.7.4), affecting distance measurement, and the pulse height is reduced due to the ionisation being split between two cells.

Another contribution is from multiple hits on a wire (section 4.4.2), where the measured height of the second pulse can be greatly reduced, while the measured arrival time is lengthened.

A direct cause is the effect of pulse shape. It has been noticed, from visual inspection of plots of FADC pulse trains, and from the studies of ratio of pulse height to integrated pulse size (section 4.3.2), that very small pulses are often different in shape to larger ones, having, instead of the characteristic sharp rising edge and long tail, a rounded, almost Gaussian, appearance. A shallower rising edge will cause the DSP to overestimate the arrival time, as described in section 4.3.3.

On the premise that the primary cause of these pulse height-related effects is a systematic mismeasurement of drift time, a pulse height-based offline correction is currently applied to the raw times of hits, before commencing track reconstruction. Figure 4.9 shows the results of a correction of 1.5 ns to saturated pulses, $0.5 - 50/max(pulseheight - 4, 1)$ to unsaturated pulses.

4.7.3 Where the Planar Drift Approximation Comes Adrift

The time measurements of hits are converted into position measurements using the *planar drift approximation*. This assumes that ionisation will drift with a uniform velocity, and in a straight path, towards the nearest sense wire. Although a good approximation, it is not a complete description of what is happening, and there are cases in which it can go noticeably wrong.

Looking at figure 3.1 in chapter 3, it is apparent that there are regions where the drift paths are far from straight. At small drift distances, they curl in towards the sense wires. There are also various distortions due to the effects of fields associated with neighbouring ground wires, shaper wires and field wires.

However well-measured the arrival time, position co-ordinate will be mismeasured if the ionisation has travelled by a path of different length to that assumed. In fact, the situation is usually compounded because the time measurement is affected as well, since any localised distortion of the drift lines will result in drift paths of unequal lengths, causing some degree of spread in arrival time and thereby changing the pulse shape.

The planar drift approximation can also fail in regions where the drift velocity is non-uniform. There are indications that this could be the case in the vicinity of cell boundaries.

4.7.4 Effects at Large Drift Distance

For particles passing close to the edges of cells, the ionisation collection efficiency may be reduced, the drift velocity may be reduced and the ionisation could be split between two cells.

It is apparent from the track residuals, as shown in figure 4.10(a), that position measurement is significantly affected in the proximity of a cell boundary. That the shift in the residuals is negative indicates that the distance measurement tends to be overestimated. It is believed that most of the negative distances seen in figure 4.10(a) (hits measured to be beyond the end of the cell), are also due to overestimation of drift distance, although it is possible for ionisation to leak in from beyond the cell boundary. This systematic shift in distance measurement could be the result of a change in shape associated with small pulses. Equally, it could be caused by a reduction in drift velocity. Comparing figure 4.10(a) with figure 4.2(a), it is apparent that whereas pulse heights begin to fall at about 0.5 cm from the cell boundary, there is no noticeable effect on distance measurement until about 0.2 cm from the cell boundary. This suggests that the change in distance measurement is not directly related to the change in pulse shape, and is a consequence of other factors, such as a reduction in drift velocity as the electric field becomes non-uniform.

Figure 4.10(b) shows the result of applying a Gaussian-shaped correction to hits within 2 mm of the cell boundary. At all physically realistic distances (i.e. less than the cell length) any systematic shift in the residuals is well within 100 μm. It can also be seen, by comparing the statistical error bars in negative regions of figures 4.10(a) and (b), that fewer hits are measured to be outside the cell.

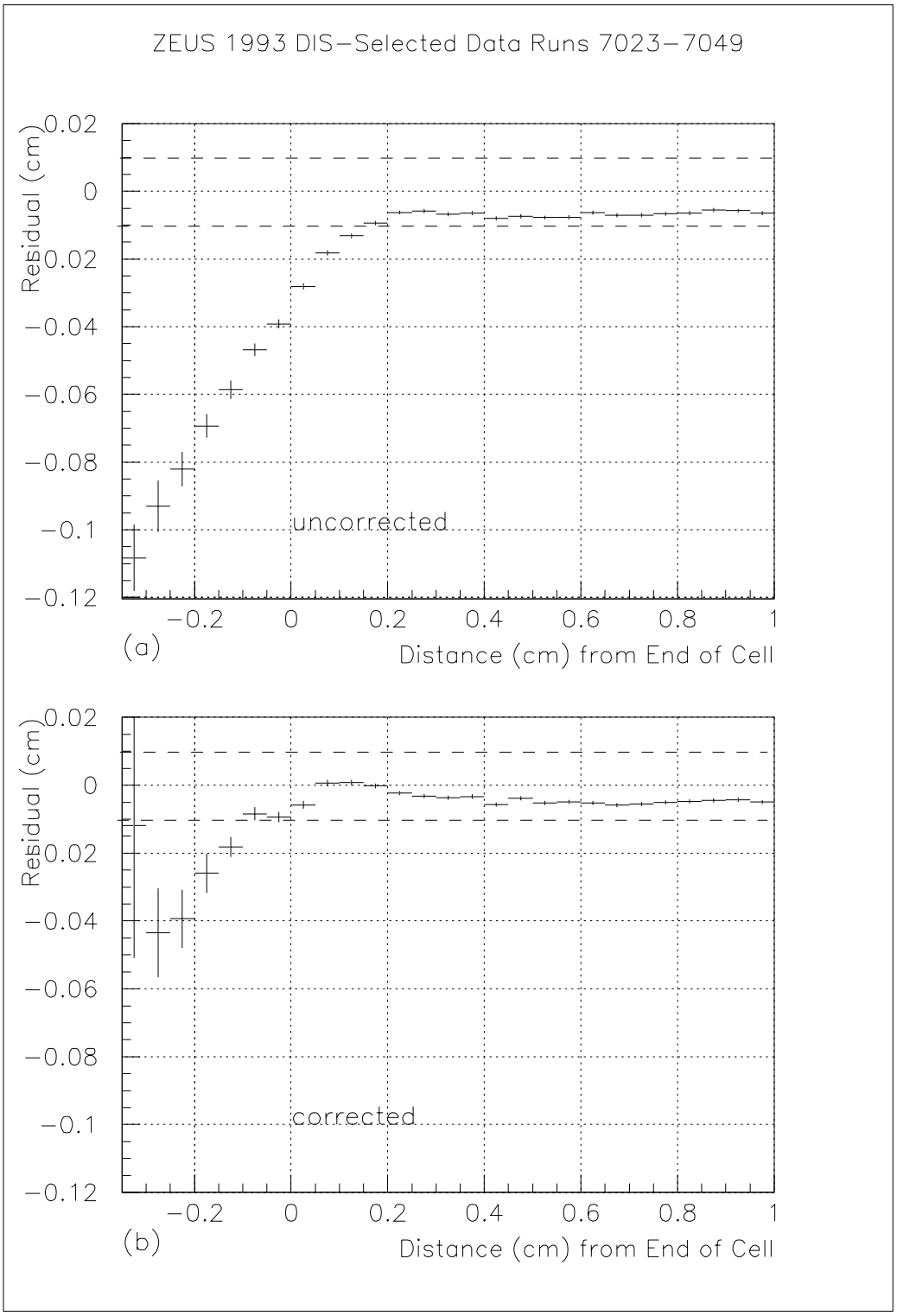

Figure 4.10: *Residual versus measured distance of hit from end of cell, (a) uncorrected, (b) corrected. Negative values indicate hits whose positions have been measured to be beyond the end of the cell – usually from position mismeasurement due to an overestimation of arrival time.*

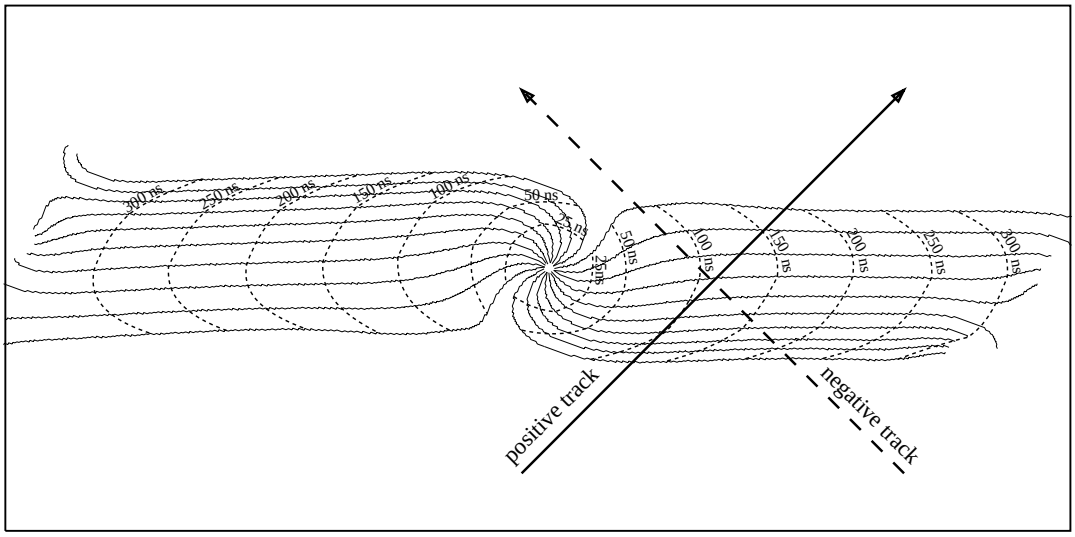

Figure 4.11: *Detail of drift paths of electrons towards a single sense wire in the CTD, and lines of constant drift time (dashed).*

4.7.5 Track-Angle Effects

When a charged particle crosses a plane of drift in the CTD, the path taken by the ionisation is affected by the angle between the track and the plane of drift, which, in turn, depends on the momentum and charge of the track. For tracks nearly perpendicular to the plane of drift (i.e. straight tracks), most of the ionisation tends to arrive together, producing a pulse with a clearly-defined leading edge which gives an accurate time measurement. However when tracks curve to shallow angles, the various paths taken by the ionisation differ very significantly in length (see figure 4.11). So some of the ionisation arrives early, and some of it late, causing the pulse shape to become more spread-out and less well-defined. Since the first ionisation arrives early the overall drift time tends to be underestimated relative to the planar drift approximation. However this is partly counteracted by the change in pulse shape, which tends to lengthen the time measurement.

Systematic Effects on Positive and Negative Tracks

In a magnetic field, the Lorentz force causes an asymmetry between positive and negative tracks, as the drift lines are twisted in the proximity of a sense wire, as seen in figure 4.11, and in chapter 3, figure 3.1. Consequently the angle giving optimal measurement corresponds to that made by a slightly curving positive track. While both positive and negative tracks tend to be less well measured at shallow angles, the effect is more pronounced for negative tracks.

This is demonstrated in figure 4.11 which shows the drift paths of ionisation

towards a single sense wire, with superposed arrows representing the paths taken by a positive track and a negative track, each at 45° to the drift plane. Both tracks are drawn to have the same measured distance in the planar drift approximation, corresponding to a drift time of somewhat more than 100 ns. It can be seen that the first ionisation from the positive track arrives earlier than this, at 100 ns, and for the negative track, even earlier.

In addition the ionisation from the negative track arrives over a longer period. The difference in arrival time between the first and last ionisation is more than 100 ns for the negative track. For the positive track it is less than 100 ns, with most of the ionisation arriving within a 50 ns interval. This causes a difference in pulse shape, and lower pulse heights, for negative tracks, which has been confirmed in the dE/dx calibration [23]. Another consequence is that the pulse from the negative track in figure 4.11 has more chance of being broken up since the same amount of ionisation is distributed over a larger range of FADC drift bins. This is discussed further in section 4.9.

The ψ' Angle

A useful quantity, in this context, is an angle which, for historical reasons, has become known within the ZEUS experiment as ψ'. This is defined as the angle between the tangent to the track and the normal to the ionisation drift direction (positive towards increasing ϕ). It is zero for completely straight tracks, which are perpendicular to the drift direction, positive for positive tracks and negative for negative tracks. Figure 4.12(a) shows how the residuals vary with ψ'. For negative tracks ($\psi' < 0$) there is a shift in hit position of about 400 μm at 45° (-0.8 radians).

The distribution is asymmetric. Its minimum is shifted to the right from zero, so that the residuals are smallest for small positive values of ψ'. This supports the previous discussion that slightly curving positive tracks are the best measured.

Figure 4.12(b) shows the results of a correction to the distance measurement, $0.15(1 - sin(\psi' - 0.07)) - 0.008$, applied during both the pattern-recognition and track-fitting stages of the reconstruction. The systematic shift has been reduced to well within the acceptable region of ± 100 μm.

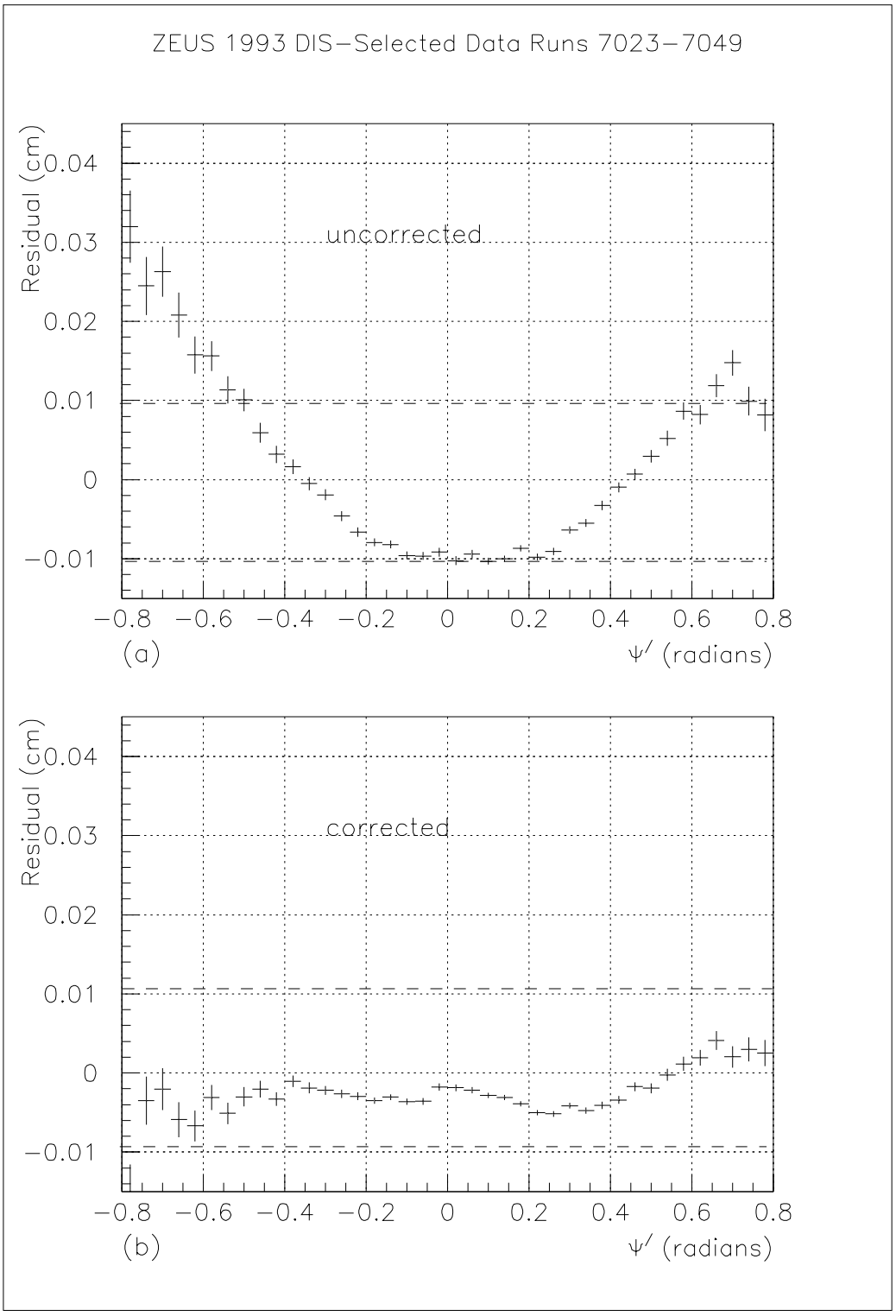

Figure 4.12: *Residual versus ψ' (a) uncorrected, (b) after position correction during the pattern recognition and track fitting.*

4.8 Multiple Hits Revisited – 1993 DSP data

In section 4.4, position mismeasurement effects due to two or more hits occurring on the same wire were investigated using FADC pipelines from the 1992 data. It was hoped that the 1993 data would show a systematic shift in the residuals of second and subsequent hits, which would provide a basis for the calibration of time corrections for second hits directly from the data.

The results were, however, significantly different to what had been expected, revealing

- about 20% of hits followed by second hits on the same wire, compared with an expected 10%,
- a disproportionate tendency for double hits to be very close together,
- second hits often wrongly assigned to tracks,
- a strong correlation of all of these effects with the ψ' angle, and
- evidence suggesting break-up of pulses, particularly at large negative ψ'.

4.8.1 Effects of Second Hits on Residuals

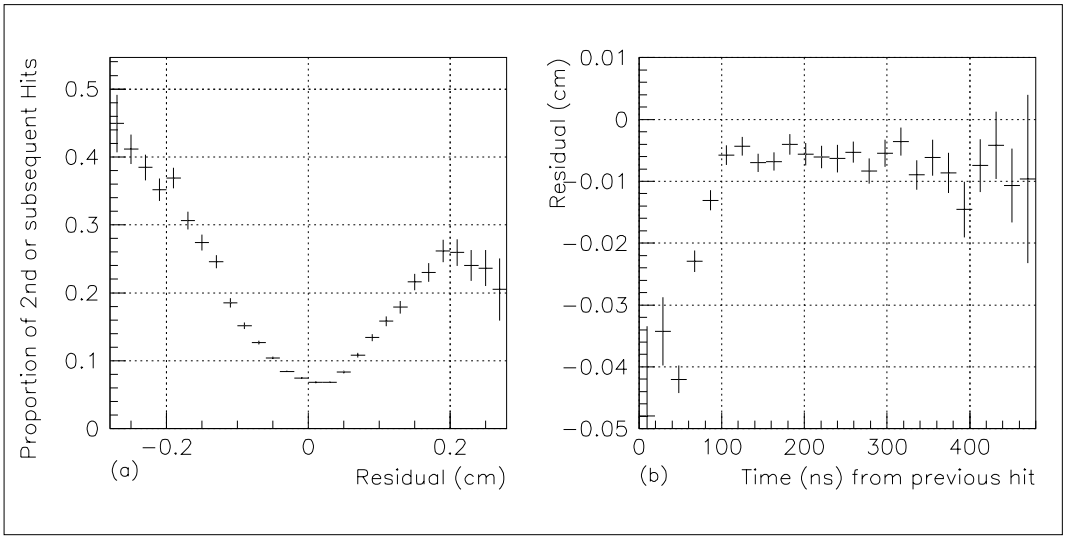

Figure 4.13: *(a) Proportion of hits on tracks, out of the total, which are second or subsequent hits on a wire, versus the track residual. (b) Residuals of second or subsequent hits versus the time interval from the previous hit.*

At first glance, the 1993 data appears consistent with the results obtained in section 4.5 from overlaying pulses. Figure 4.13 confirms that the times of second

and subsequent hits tend to be badly measured, and in general, overestimated. Figure 4.13(a) shows that a disproportionately large number of hits with very large residuals are second or subsequent hits. Second hits comprise about 40% of hits with residuals beyond $-0.2\ cm$. Figure 4.13(b) shows a systematic negative shift in the residuals of second hits separated by less than 125 ns, becoming more pronounced as the separation between the hits decreases.

However, a closer look reveals important differences between the two sets of results.

Firstly, the magnitude of the effect observed in the 1993 data is much greater. When the two hits are separated by 50 ns, the average shift observed in the residuals of second hits is over 400 μm, compared with 150 μm (3 ns) predicted from the 1992 double pulse studies (figure 4.5(b)).

Secondly, the shape of the distribution of residuals of second hits, shown in figure 4.14(a), is distorted. The peak is shifted by less than 100 μm, the overall negative shift observed in figure 4.13(b) being caused by a prominent shoulder of large negative residuals. This effect is more pronounced for negative ψ', introducing a dependence on charge. This will be discussed later.

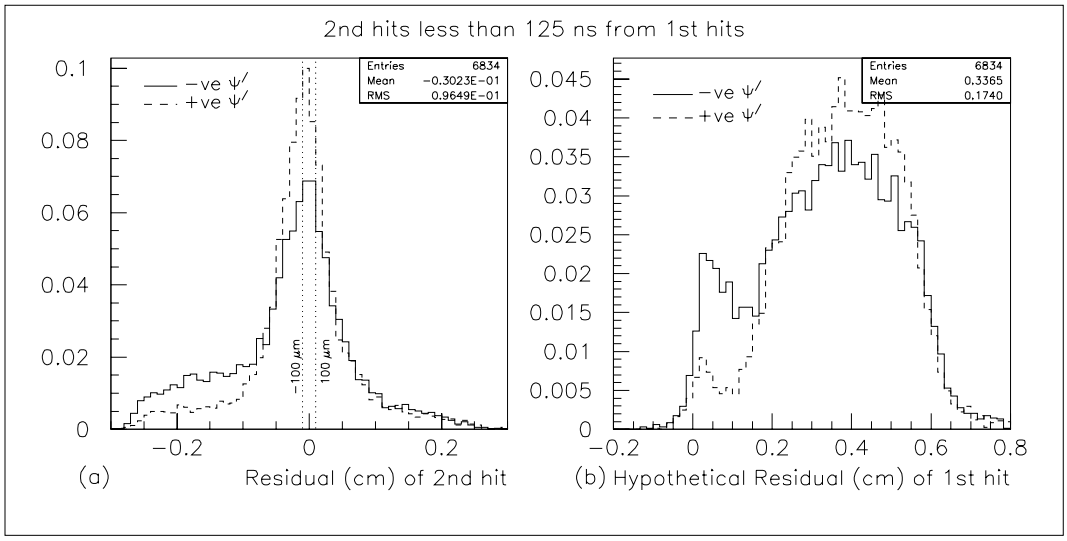

Figure 4.14: *(a)Residuals of hits separated by less than 125 ns from a previous hit on the same wire, for positive and negative ψ'. (b)Residual which the corresponding previous hit would have had, if it had been assigned to the track.*

4.8.2 Two-Hit Confusion

This distortion of the distribution of residuals for the second hit, seen as the shoulder in figure 4.14(a), is in fact caused by hits being wrongly placed on the track to which the previous hit should have belonged. This is shown in

figure 4.14(b). The distance from the previous hit is added to the residual, giving the value of the residual which the previous hit would have had, if it, rather than the second hit, had been assigned to the track. With this transformation, the large negative shoulder in figure 4.14(a) becomes, in figure 4.14(b), a peak close to zero, clearly demonstrating that the pattern recognition has chosen the wrong hit.

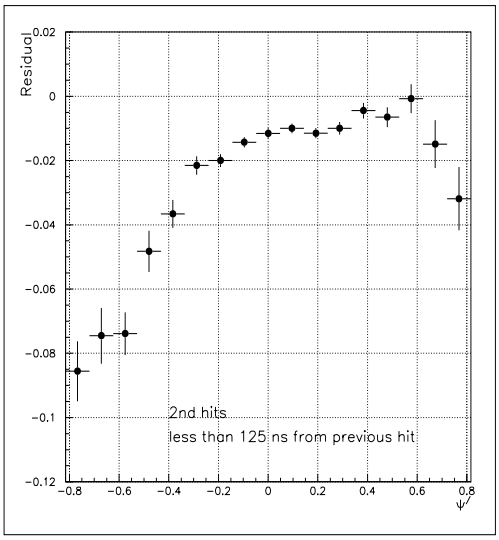

Figure 4.15: *Residual versus ψ' for hits separated from a previous hit by less than 125 ns.*

The probability for wrong hits to be put on tracks is strongly dependent on ψ'. Figure 4.15 shows residual versus ψ' for hits separated by less than 125 *ns* from a previous hit on the same wire. Instead of the usual systematic positive shift for extreme ψ' values (figure 4.12), an increasing tendency at large negative ψ' for second hits to be misassigned to tracks causes the distribution to curve in the opposite direction.

It is perhaps surprising that second hits are so often put on tracks in place of first hits, since overestimation of their arrival time would move them apart. However, if the measured arrival time of the first hit is early, as is the case at extreme ψ', and if a second hit follows closely, then the pattern recognition would have a difficult task deciding between them.

There is no observable corresponding tendency for first hits on a wire to be misassigned to tracks in place of second hits, perhaps because first hits are usually better-measured than second hits. It might also be that second hits are far less likely to be genuine hits, as will be discussed later.

4.8.3 Difficulties in Using Residuals to Correct Position

For second hits following less than 125 *ns* behind a previous hit on the same wire, the distribution of residuals is clearly non-Gaussian.

The typical shift in residuals caused by misassignment of second hits to tracks is far greater than that which would be expected to result from time mismeasurement due to changes in the gradients of the rising edge of second hits. Moreover, there is no clear way to disentangle the two effects.

This means that it is probably not possible, and certainly not straightforward, to calibrate systematic position corrections to second hits from the residuals in the manner employed in section 4.7.

4.9 Separation Between Multiple Hits

4.9.1 Why are Second Hits Left Off Tracks?

It is evident in both the 1992 and the 1993 data that when there are two or more hits on a wire, the first hit is far more likely to belong to a track than are any subsequent hits.

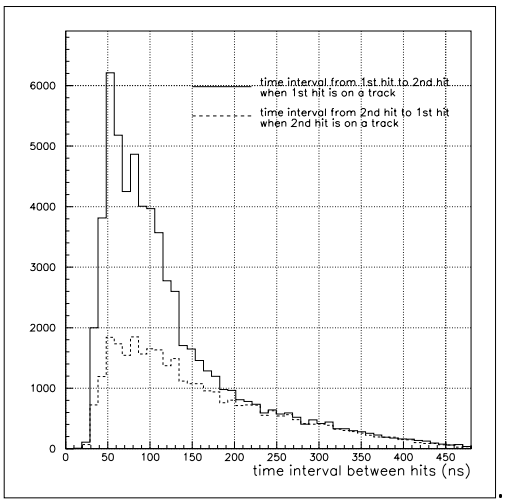

Figure 4.16: *Time interval between hits in the 1993 data.*

Figure 4.16, which shows two superposed distributions from the 1993 data, one of the time interval to the next hit in cases where the first hit is on a track but the second hit need not be, the other of the time interval from the previous hit in cases where the second hit is on a track but the first hit need not be. Two features are apparent. Firstly, comparison of the number of entries shows that far more first hits than second hits are being assigned to tracks. Secondly, this difference is true only for hits separated by less than 200 *ns*. For larger separations, the two distributions are identical.

A plausible explanation for this discrepancy between the numbers of first hits and second hits assigned to tracks when the two hits are close together is that second hits are mismeasured to such an extent that they are rejected by the pattern recognition or track fit. The closer together the two hits are, the worse the time measurement of the second hit is likely to be.

Another possibility is that second hits are less likely than first hits to be genuine. This could be due to noise hits following immediately after genuine hits, which might happen with a "noisy" gas. Alternatively it could be that the ionisation associated with a single track is not arriving at the sense wire coherently, and produces an irregular signal that is interpreted by the DSP as two or more separate pulses. This latter case might be expected to show a track angle dependence, since, as explained in section 4.7.5, at large negative ψ' the ionisation associated with a single hit can be spread among drift paths of widely varying length.

One or all of the above effects could be present, and it would be useful to have some idea which is dominant, and also to have some idea of how many genuine multi-hits are expected, and how the separation of genuine multi-hits ought to be distributed.

4.9.2 How Many Multi-Hits are Expected?

In the Monte Carlo dataset used here there is no simulation of noise (section 4.2.3). Every hit observed is caused by a charged particle passing through the CTD.

In the real detector there is undoubtedly noise of one kind or another, so it is reasonable to expect that there will be more instances of multiple hits on a wire in the data than in the Monte Carlo. If these are purely random, most will not be assigned to tracks. Figure 4.17(a) shows the number of hits on a wire on which there is at least one hit belonging to a track, versus superlayer, for the 1993 data and for Monte Carlo. As expected, the number of multi-hits progressively decreases with each superlayer, as tracks become further apart. However, it appears that, unlike random noise, many of the extra hits found in the data are associated with genuine hits, since, compared with the Monte Carlo, more of the hits assigned to tracks in the data belong to multi-hit trains. The frequency with which these extra hits occur has a clear ψ' dependence, shown in figure 4.17(b). Through most of the positive ψ' range there are about twice as many second or subsequent hits in the data as in the Monte Carlo. For negative ψ' this increases sharply until, when ψ' is -1, there are more than seven times as many. This suggests that a substantial proportion of multi-hits are caused by irregular or broken pulses. The peak at $\psi' = 0$ in both Monte Carlo and data occurs in the inner superlayers where tracks are closer together and have not curved much.

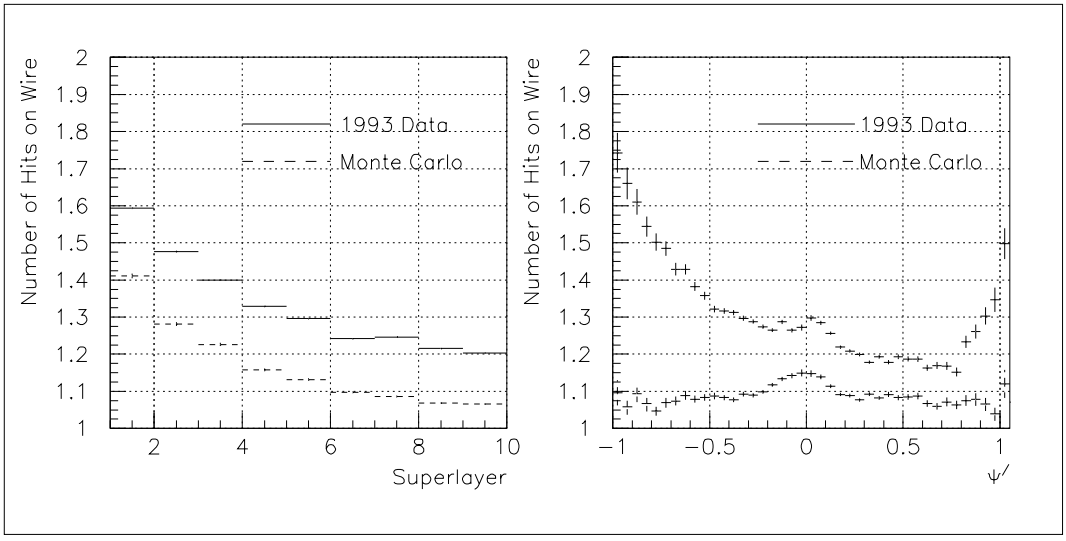

Figure 4.17: *(a)Number of hits on a wire versus superlayer. There is a greater frequency of multiple hits in the data than is predicted in the Monte Carlo. (b) Number of hits on a wire versus ψ'. Hits on tracks at extreme ψ', particularly for negative ψ' values, are far more likely to belong to a multi-hit train than are hits at central and medium-positive values of ψ'.*

4.9.3 The Expected Distribution of Hit Separation

If multiple hits occur randomly within a restricted interval (as in a drift cell) the resulting distribution of hit separation will not be flat but peaked towards zero. Consider a sense wire for which the maximum drift distance (i.e. the distance to the cell boundary) is $Dmax$, corresponding to a maximum drift time $Tmax$, on which there are two random hits, one of which arrives at time t. If the other hit has arrived earlier, the maximum separation between the hits will be t. If it arrives later, the maximum separation will be $Tmax - t$. There are then two ways in which the hits can be separated by $min(t, Tmax - t)$, and only one way in which they can be separated by $max(t, Tmax - t)$. Therefore there will be a tendency for hits to be close together rather than far apart.

The resulting normalised distribution of the time separation $tsep$, where there are specifically two hits per wire, is triangular, of the form

$$\frac{1}{N}\frac{dN}{d\ tsep} = \frac{2}{Tmax} - \frac{2tsep}{Tmax^2} \tag{4.1}$$

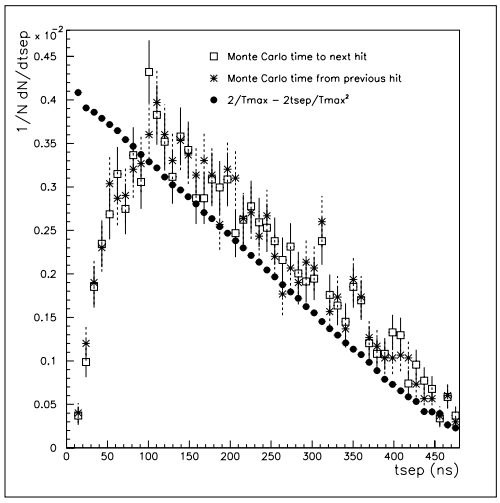

Figure 4.18: *Time interval between hits observed in the Monte Carlo, with superposed distribution expected from random statistics.*

In the CTD the maximum drift distance varies with each wire layer, and on either side of the sense wire within a cell (see figure 3.1, chapter 3), and there is a difference of more than 200 ns between the smallest and largest value of $Tmax$. The average value of $Tmax$ will to a certain extent depend on the hit separation, since hits are more likely to be separated by large intervals where there is a large maximum drift distance.

Figure 4.18 shows the normalised distributions of the hit separation seen in the Monte Carlo data in cases where there were two hits per wire, using superlayers 4 to 9. Superposed are the corresponding values obtained from equation 4.1, averaged over the values of $Tmax$ present in the data in each bin of $tsep$.

Unlike the ZEUS data, shown in figure 4.16, the Monte Carlo shows no difference between the distributions of the time difference from the first hit to the next, when the first hit is on a track, and the second hit from the previous, when the second hit is on a track. Both distributions are consistent with that expected from randomly occurring multi-hits, given by equation 4.1, apart from a fall-off at small separations, due to inefficiency of resolving the two hits, which has been

input into the Monte Carlo, and its consequence is that, due to the overall normalisation, the Monte Carlo distribution appears higher at separations greater than 100 ns.

4.9.4 The Observed Distribution of Hit Separation

The distributions seen in figure 4.16, particularly that of the time from the first hit to the second, when the first hit is on a track, appear to be quite different. However, in the region where the hits are separated by more than 200 ns, and both distributions of figure 4.16 coincide, the slope is in fact consistent with that given by equation 4.1. Weighting by the reciprocal of $\frac{2}{Tmax} - \frac{2tsep}{Tmax^2}$ results in both distributions, as well as the Monte Carlo distributions, becoming flat in this region.

This is shown in figure 4.19. All distributions have been normalised such that the flat region has the value of 1. These weighted distributions can be regarded as a kind of efficiency. (Compare the Monte Carlo curve in figure 4.19 with the two-hit resolution efficiency shown in figure 4.4.) Where the distributions are below 1, there are fewer hits than expected from statistical probability, indicative of two-hit resolution inefficiency. Where the distributions are above 1, there are more hits than there should be, suggesting the presence of spurious hits associated with genuine hits on tracks.

The Monte Carlo distributions in figures 4.19(a) and (b) are flat for hits separated by more than 100 ns. At smaller separations, they essentially give back the two-hit resolution efficiency distribution which has been incorporated into the production of Monte Carlo raw hits (section 4.2.3).

The real data from the CTD is strikingly different. Figure 4.19(a) shows the time interval between the first and second hit of a double pulse, when the first hit is on a track but the second need not be. More of the hits assigned to tracks have a second hit following closely afterwards than are expected , and there are far more of these extra second hits at negative than positive values of ψ'. This is consistent with the hypothesis that pulses associated with tracks – in particular negative tracks – making shallow angles to the drift plane are irregular in shape and tend to masquerade as multiple hits.

While figure 4.19(b) shows, as does figure 4.16, that there are fewer second hits than first hits on tracks, there are still, at close separations, rather more than the Monte Carlo predicts. From figures 4.17 and 4.19 it appears likely that a large proportion of second hits are not genuine, and that usually, where there are two hits close together, the first hit is, correctly, put on the track. However there is evidence, in figure 4.19(b) and in figure 4.14 that second hits are wrongly assigned to tracks often enough to have a significant effect on the residuals.

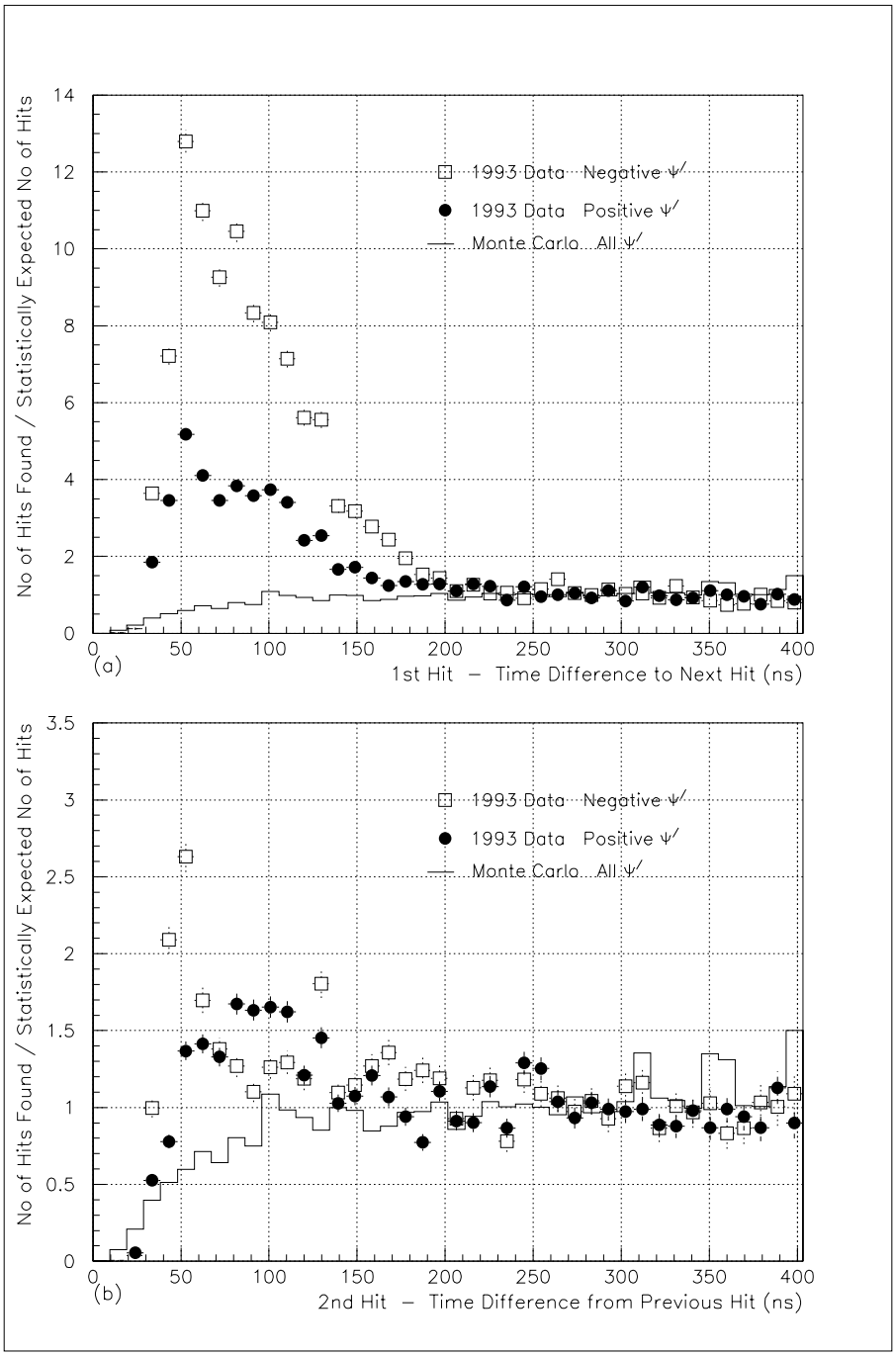

Figure 4.19: *Ratio of number of hits found to number expected from random statistics versus the time interval between hits, comparing positive and negative ψ' values in the 1993 data with the Monte Carlo data (which shows no ψ' dependence), (a) when the first hit of a double pulse has been placed on a track and, (b) when the second hit of a double pulse has been placed on a track.*

4.9.5 What Can be Done about Multi-Hits?

As discussed earlier, any systematic shift in the position measurement of second hits is compounded by confusion in the pattern recognition (which already has difficulties in the case of a curving track at a shallow angle to the drift plane) caused by the presence of spurious extra hits in close proximity to genuine ones, making correction on the basis of residuals difficult.

A possible solution is to ignore any second hits that are less than a specified interval from a previous hit. Another is to raise the threshold of the DSP for second and subsequent hits on the same wire, so that those with low pulse heights would not be found, but this could result in the loss of genuine second hits, which are also likely to have low pulse heights.

For the third level trigger tracking, it has been found that ignoring second hits at separations of less that 100 ns gives a 10% increase in speed with no vertex loss and no significant track loss.

4.10 Summary of Results from 1993 DSP Data

- Residuals of long tracks provide a very effective diagnostic of systematic effects in the CTD. Underestimation of drift time or distance will give a hit a negative residual, overestimation, a positive residual.

- There is a systematic positive shift in the residuals of saturated pulses and a negative shift in the residuals of very small pulses. These effects can be understood in terms of the arrival time mismeasurement due to changes in pulse shape. Indirectly, proximity to a cell boundary and the effect of a previous hit on the same wire can also result in smaller than average pulses with negative residuals.

- Some systematic effects are caused by deviations from the planar drift approximation. These occur where the drift paths of the ionisation electrons are not straight, and where the drift velocity is non-uniform.

- The residuals of hits close to cell boundaries exhibit a systematic negative shift, which is consistent with a change in drift velocity due to the non-uniformity of the electric field in this region.

- A major source of systematic effects is the angle between the track, at the position of a given hit, and the plane of drift. This is quantified in ZEUS by ψ'. For hits on tracks making shallow angles to the plane of drift (large abs(ψ')), there is a tendency for drift distance to be underestimated, and also for pulses to be broken up, resulting in spurious multiple hits. Both of these effects are more pronounced for negative tracks than for positive tracks. In addition, for negative tracks the ionisation from hits close to cell boundaries is more likely to be split between cells than it is for positive tracks. These factors introduce a charge dependence to track reconstruction quality, with negative tracks being systematically less well reconstructed than positive tracks.

- There are more cases than expected of multiple hits on the same wire, with the second hit typically in close proximity to the first, their frequency of occurrence depending on ψ'. Spurous second hits are often wrongly assigned to tracks.

- Corrections for systematic effects have been implemented in the reconstruction, and have contibuted to an improvement in the hit resolution from about 270 μm to less than 200 μm for long tracks.

Chapter 5

CTD Data for Physics Analysis

5.1 The Role of the CTD within ZEUS

Since the days of bubble chambers and photographic emulsions, the main focus of High Energy Physics experiments has tended to be on the detection of charged particle tracks. More recently, however, calorimetry has come to play an increasingly dominant role. The ZEUS detector is certainly a case in point, with its high resolution 4π uranium calorimeter. Event kinematics and most event classifications are obtained primarily on the basis of calorimeter data. Indeed during the first year of running, in 1992, little else of ZEUS was fully operational.

Data obtained from tracking is in many ways complementary to calorimeter data. The calorimeter can measure the total energy in an event, but tracking is needed to give the vertex position. This is required in order to accurately assign angles to energy deposits, so that event kinematics can be reconstructed. Tracking can also unambiguously assign energy to a vertex. Calorimetry provides information about all particles, charged or neutral, but cannot identify individual particles. Tracking can identify individual charged particles, and determine their position of origin, momentum and trajectory. Particle identification by dE/dx is also possible.

Analysis of ZEUS 1992 data was essentially based on calorimeter information. It was nonetheless necessary to use the CTD tracking, incomplete though it was, in order to obtain a reliable vertex position measurement. In 1993, with the CTD fully instrumented, a whole new range of physics analysis possibilities opened up.

5.2 The Necessity for Reliable Vertexing

None of the benefits of having a sophisticated tracking chamber can be attained without first good track reconstruction and reliable vertexing. If a track is not assigned to a vertex, then for the purpose of physics analysis, it disappears.

5.2.1 Vertexing with the 1993 Detector Configuration

A feature of HERA kinematics is that much of the energy tends to be emitted at small angles, particularly for the relatively low x, Q^2 region that is accessible with 1993 data. Particles associated with the proton remnant are scattered far forwards, while , at low Q^2, the electron is deflected at a very small angle to the rear. At very low x many of the particles associated with the current also tend to be emitted at small backward angles.

The tracking in ZEUS was designed to be done by a combination of inner tracking detectors – the VXD, close to the interaction point, the CTD, for detecting tracks at moderate and large angles, and the FTD and RTD to pick up small-angle tracks to the front and rear.

In the event, neither the FTD nor RTD were operational during 1993, while the VXD worked intermittently. Therefore the only tracking data consistently available as input to the vertex fit and physics analysis was that from the CTD.

5.2.2 From Track to Vertex

The previous chapter described the processes by which electronic signals read out from the CTD are converted into measurement of time, and thence position, of the hits which form the basis for reconstructing the trajectories of any charged particles passing through the CTD.

Two independent approaches to the procedure of track finding and fitting were concurrently employed by ZEUS during 1993, one [24] based on the Kalman filtering technique, the other [25] based on a helix fit. (The results presented here are based on the first of these. However, both methods were used thoughout the analysis in the following chapters, and no major incompatibilities were found.)

The vertex fit was performed with the fitted tracks using the perigee parametrisation [26]. After determining the vertex position, the track parameters at the vertex were re-evaluated.

5.2.3 What Kind of Tracks are Lost?

If some tracks are wrongly excluded from the vertex, it is important to determine whether this is a general inefficiency, or whether there is a bias against certain types of tracks.

The previous chapter examined some causes of systematic track mismeasurement. Errors from a track fit can propagate to the vertex fit, so it is reasonable to suppose that a poorly measured track is more likely to be rejected by the vertex fitting than is a well measured one.

Tracks which pass through the CTD at shallow polar angles leave few hits and are obviously difficult to measure well.

Low P_T tracks curl, so the track angle problems described in chapter 4 come into play. Where the tangent to the track curvature becomes parallel to the drift plane of the ionization, track reconstruction fails completely, so that a 2π curl is split by the reconstruction into two or more separate tracks.

Visual inspection of event displays [27] has revealed that when two or more tracks are close together, misassignment of hits can often cause exclusion of tracks from the vertex.

5.2.4 Observations from the 1993 Data

Figure 5.1 shows, from 1993 ZEUS DIS data (see chapter 6, section 6.3 for selection details), how the fraction of tracks assigned to the vertex, out of the total in the event, varies with θ, P_T and number of degrees of freedom (NDF). Of course these quantities are interrelated.

As expected, tracks at shallow polar angles are more likely to be left off the vertex, as are tracks with low P_T. However it should be remembered that these characteristics are also typical of slow protons from beam-gas and interactions with detector material, in which case they are rightly excluded from the vertex.

The tracking acceptance cuts adopted by ZEUS for 1993 data, which are described in section 5.3.3 of this chapter, are shown by the dotted lines in figures 5.1(a) and 5.1(b).

In figure 5.1(c) it is noticeable that tracks with very large NDF are less likely to be assigned to the vertex than are tracks with moderately large NDF. This points to a possible problem with the vertex fit, caused by the fact that very well measured tracks are liable to be highly constrained and therefore more likely to be rejected.

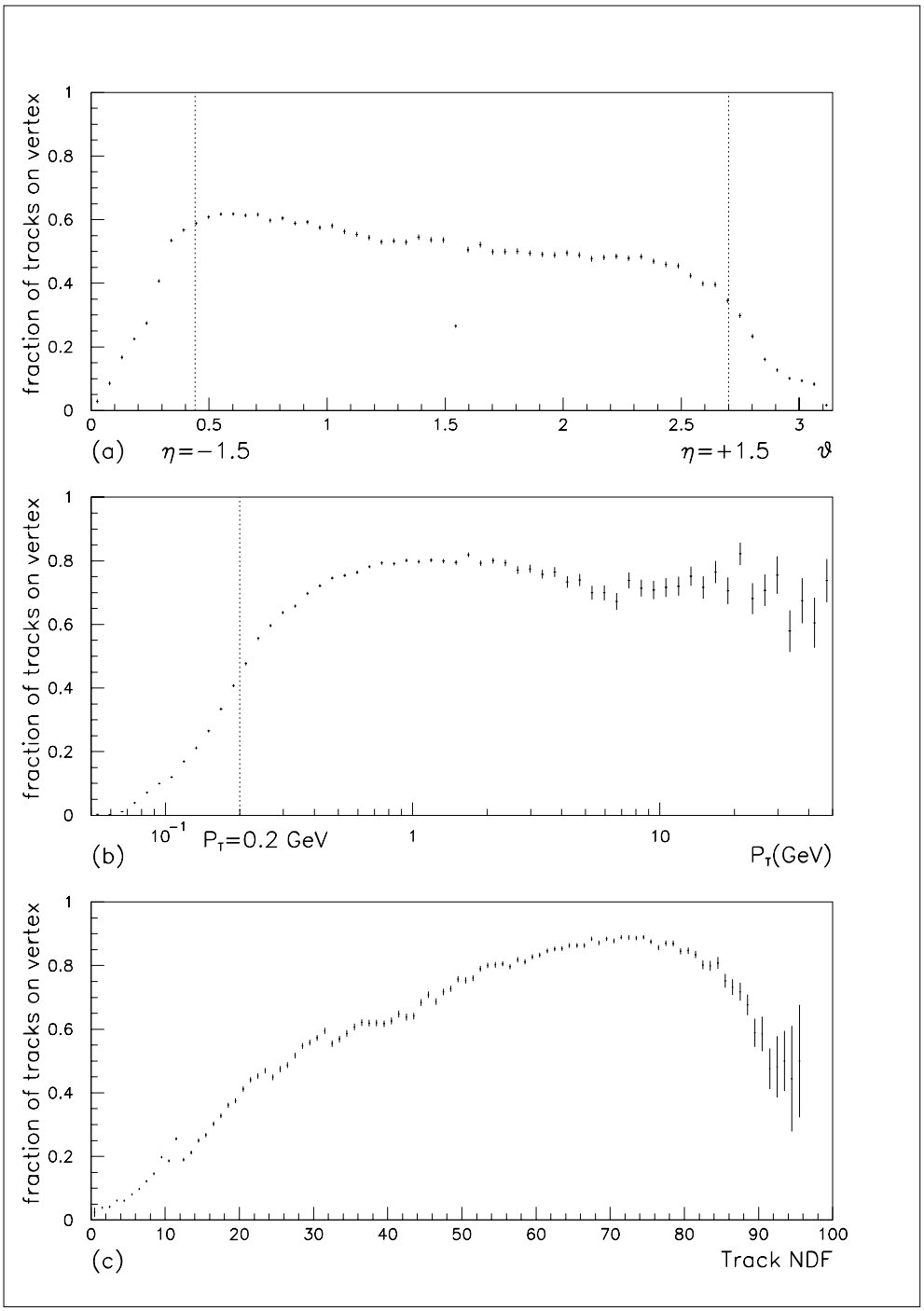

Figure 5.1: *How the probability of a track being assigned to the vertex varies (a) with its polar angle, (b) with its P_T, (c) with its NDF. The dotted lines represent the acceptance cuts which were later imposed on physics analysis.*

5.3 Believable Tracking

5.3.1 Systematic Effects on Positive and Negative Tracks

As discussed in chapter 4, section 4.7.5, one of the major causes of systematic track mismeasurement, the ψ' effect, is related to track curvature, and distinguishes between positive and negative tracks. Hits on negative tracks tend to have a larger systematic shift in position, as well as a smaller pulse height and therefore lower hit efficiency. The pulses are also more likely to be broken up into spurious double hits, compounding the difficulties of the track reconstruction.

From figure 5.2 it can be seen that positive tracks do indeed appear to be better measured than negative tracks, in terms of the number of hits assigned. Of tracks with a NDF of 80 or more (including VXD hits), two-thirds are positive.

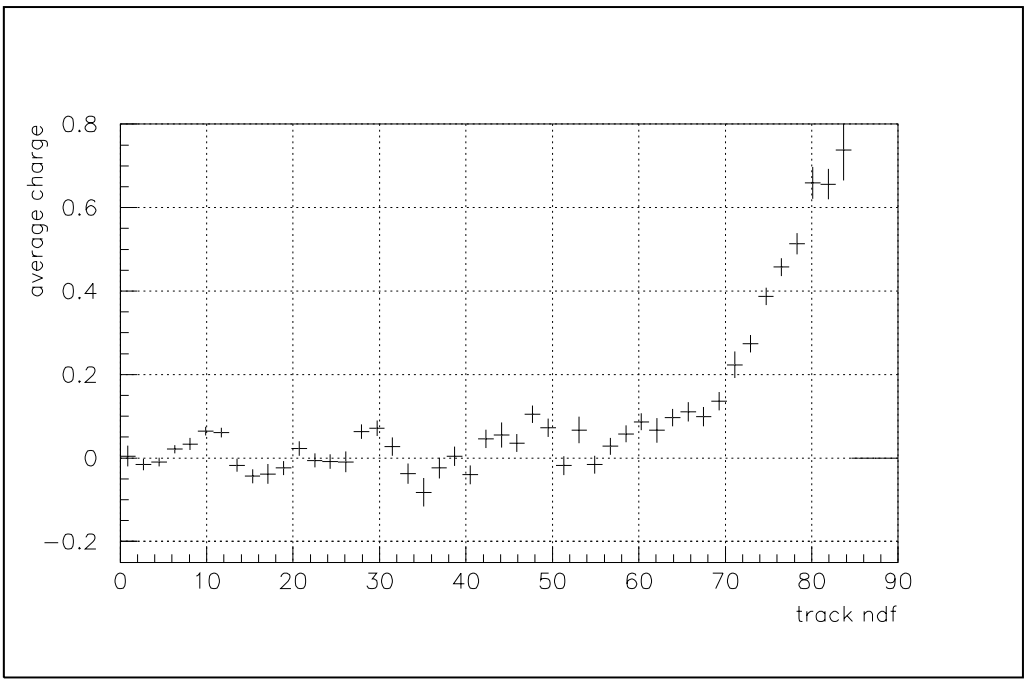

Figure 5.2: *Average track charge versus NDF. Of the tracks with large NDF, comparatively few are negative. The jagged structure at lower NDF values reflects the superlayer structure of the CTD.*

Figure 5.3 shows the NDF versus $charge/P_T$ for tracks which have been assigned to the vertex and which have reached the outermost superlayer of the CTD. If the hit-finding and track reconstruction were 100% efficient, these tracks would each be expected to have 72 FADC hits plus additional z-by-timing hits and VXD hits. Here, again, it is clear that negative tracks are on average less well reconstructed than positive tracks, having fewer hits.

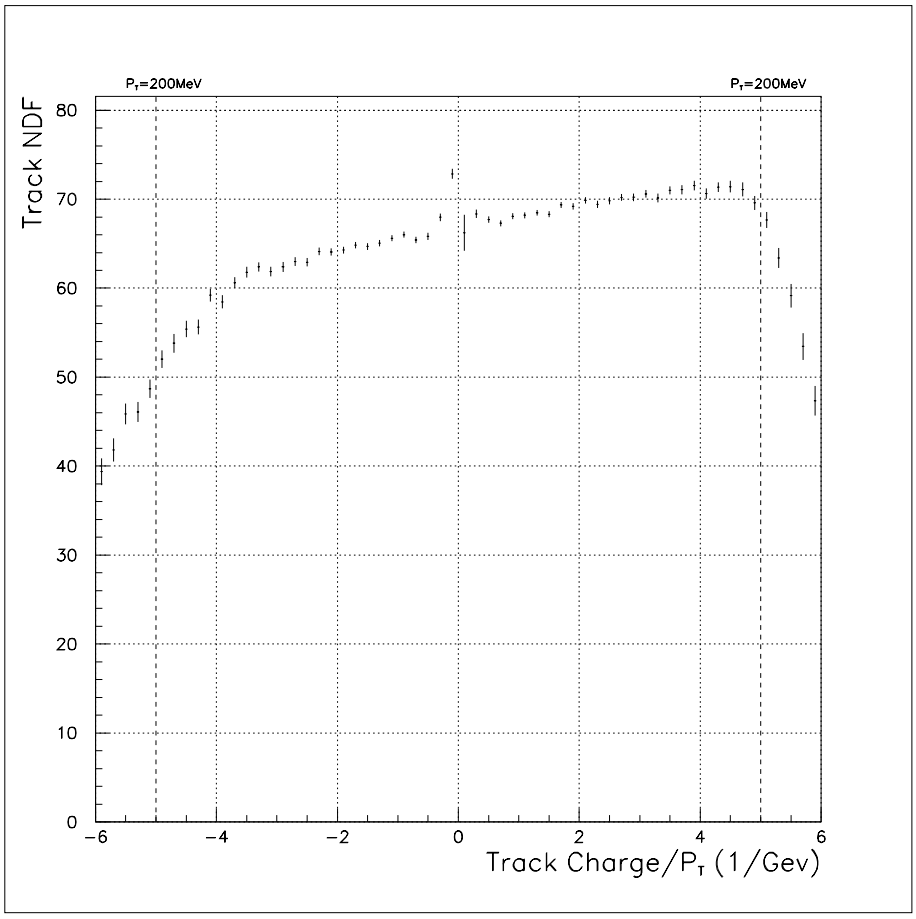

Figure 5.3: *Average NDF versus track charge/P_T, for tracks assigned to the event vertex which have reached the outermost superlayer of the CTD.*

For values of P_T below 200 MeV, the average NDF falls dramatically, for both positive and negative tracks, but in this region, too, positive tracks have systematically more hits than negative tracks. These curling low P_T tracks tend to have hits at extreme values of the ψ' angle, where hits are generally badly measured and more likely to be excluded from the track. So although these tracks reach the outermost superlayer they have fewer hits than do straighter tracks. This is particularly true for low P_T negative tracks.

Tracks with values of P_T below about 180 MeV curl too tightly to be able to reach the outermost CTD superlayer.

5.3.2 Measured Net Charge of Events

Difference in the measurement quality of positive and negative tracks raises concerns about negative tracks being systematically excluded from the vertex. Fortunately, this does not appear to be the case.

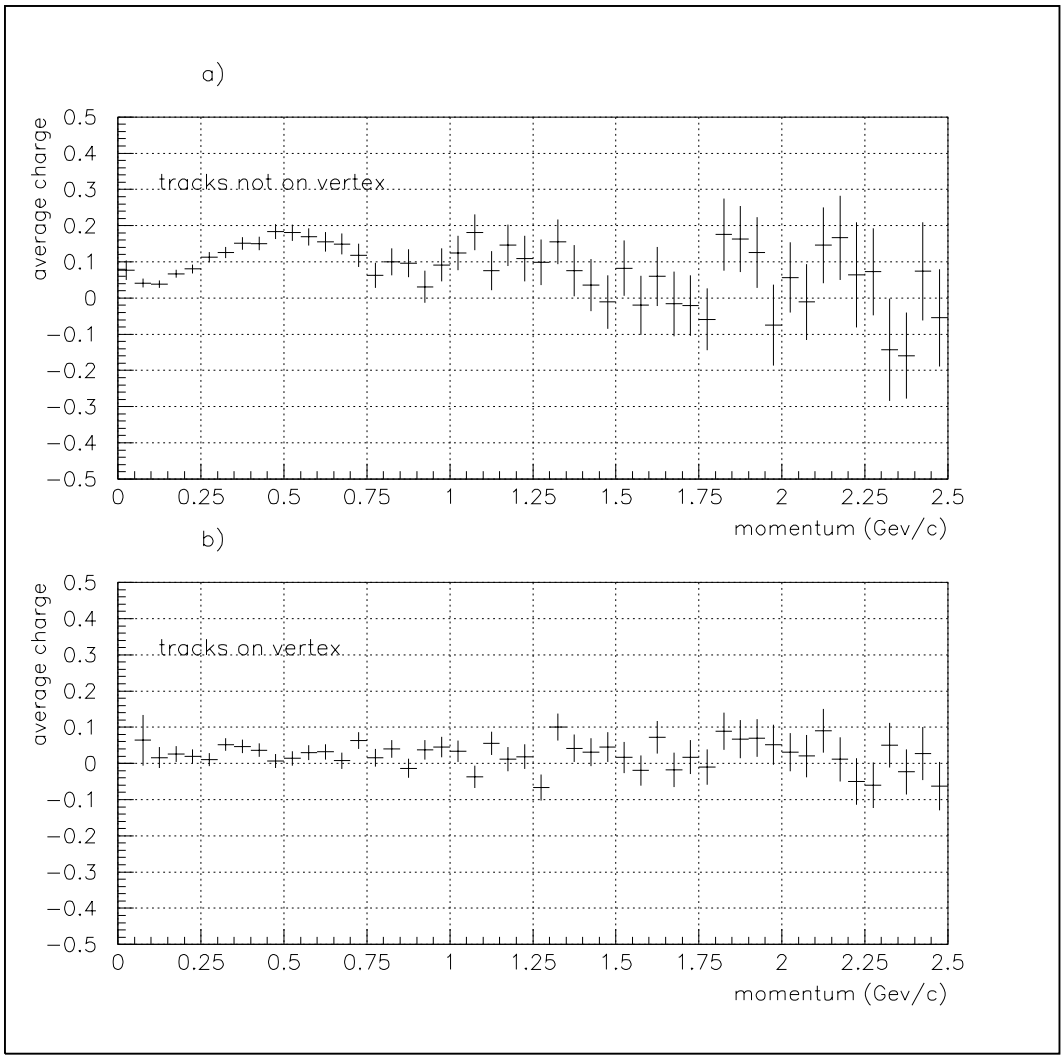

Figure 5.4: *Average charge versus momentum (a) of tracks left off the event vertex, (b) of tracks assigned to the event vertex. Although positive tracks are better reconstructed than negative tracks, they do not appear to be preferentially assigned to the vertex*

Figure 5.4(a) shows that tracks excluded from the vertex have a slight tendency to be low-momentum positive tracks, such as one would expect from protons coming from interactions with material in the detector. Figure 5.4(b) shows that regardless of the systematic effects, positive and negative tracks are assigned

to the vertex in equal proportions.

Figure 5.3 contains only tracks which have been assigned to the vertex. That a considerable systematic difference in reconstruction quality between positive and negative tracks shows up in this sample is evidence in itself that the poorer quality has not caused significant rejection of negative tracks.

So it seems that although negative tracks are less well measured than positive tracks, they are unlikely to be completely lost from the event.

5.3.3 Track Quality Cuts

After the systematic effects on tracking became evident, it was felt that until such time as they were better understood, and able to be simulated in Monte Carlo, it was safest to restrict physics analysis involving CTD tracks to the regions which were least sensitive to these systematics. The following two cuts:

- $P_{T_{track}} > 200 MeV$, and
- $-1.5 < \eta_{track} < 1.5$

were therefore recommended [28] and generally adopted by ZEUS for tracking analysis of 1993 data.

More recently, following implementation of these effects in the simulation, it has been advised [29],[30] that these cuts are no longer necessary for analysis of data from 1994 or later.

5.3.4 Tracks as Physics Objects

An electron and proton collide, sending a spray of charged particles through the CTD. Ionisation drifts to sense wires. Pulses are read out by the CTD electronics. Digitised data is written to a DST tape, and so the event is encrypted.

These past two chapters have effectively been working backwards from the recorded digitisations, reconstructing the pulses, tracks and, finally, the interaction vertex.

Having gained some understanding of these processes and, importantly, some awareness of possible pitfalls, it is time to move on, from thinking of tracks in terms of hits, wires and chamber geometry, to thinking of them in terms of the physics objects which produced them.

The following chapters constitute an analysis of the charged hadronic final state of DIS events observed at ZEUS during 1993, with the first data available from the fully-instrumentated CTD.

Chapter 6

DIS Events at ZEUS

6.1 What Does DIS Look Like at ZEUS?

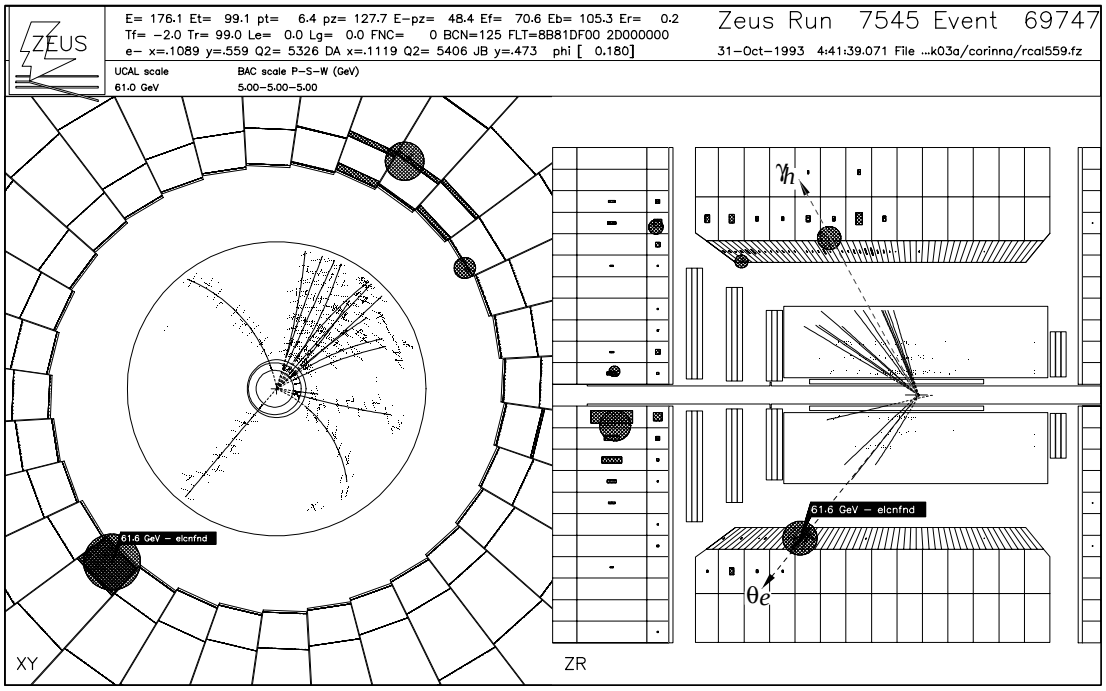

Figure 6.1: *A DIS event with $Q^2 = 5393 GeV^2$. The scattered electron and current jet are clearly defined in both tracking and calorimeter. The dashed arrows in the Z-R view show the reconstructed electron and quark angles*

In a DIS event at HERA, an electron with energy E_e of 27 GeV collides with a proton with energy E_p of 820 GeV travelling in the opposite direction, causing a quark to be ejected from the proton. In the final state the electron is scattered into the ZEUS detector at some polar angle θ_e and with energy E'_e, while the quark is emitted at a polar angle γ_h and has energy F, as shown in figure 6.3. The inequality between the initial energies E_e and E_p results in a large forward

boost in the HERA laboratory frame, causing the spectator quarks from the proton (the target remnant) to go into the forward beampipe.

The scattered electron can usually be easily identified and accurately measured using the ZEUS calorimeter.

The struck quark hadronises. If it is sufficiently energetic, i.e., in events with a large enough value of F, the hadrons will typically form a single well-defined jet, closely correlated in direction with the original quark, and, balancing P_T, at 180° in azimuth from the scattered electron.

This is the "classic" type of DIS event associated with HERA, an example of which is seen in figure 6.1. However, comparatively few of the events in the 1993 ZEUS DIS sample are of this nature.

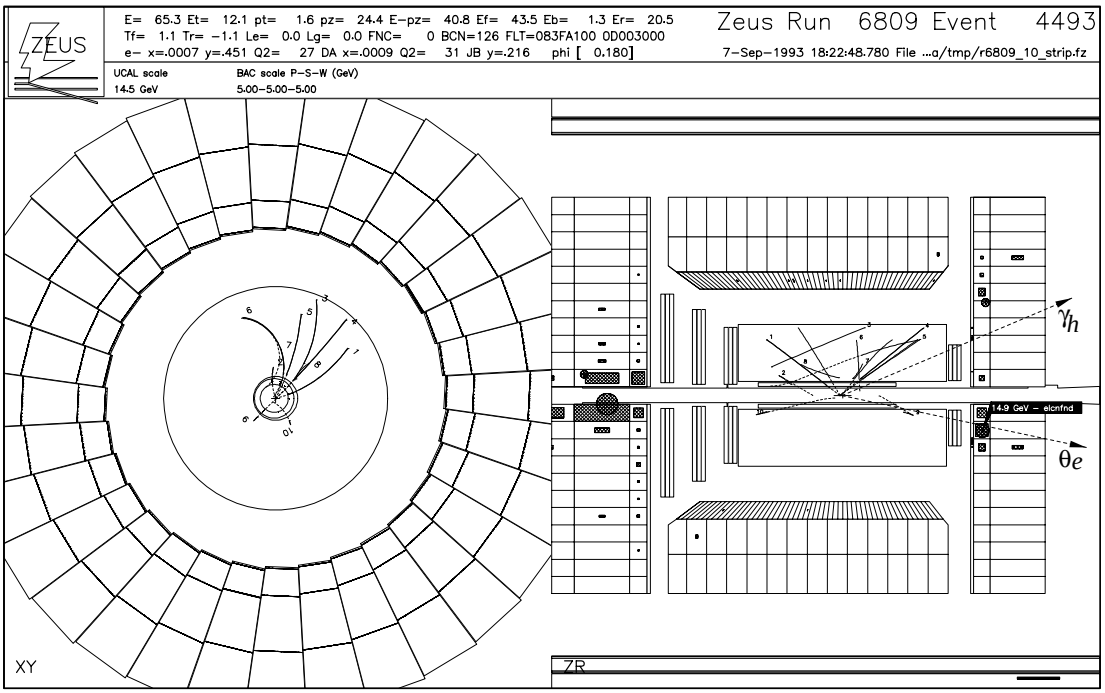

Figure 6.2: *A DIS event with $Q^2 = 31\,GeV^2$. The dashed arrows in the Z-R view show the reconstructed electron and quark angles. There is a spread of energy between the current and target directions. The electron has grazed the CTD, leaving a badly-measured track which has been excluded from the event vertex.*

Figure 6.2 shows the kind of DIS event more frequently encountered at HERA. The cross-section for DIS being inversely proportional to Q^4, the 0.55 pb^{-1} of data taken during 1993 yielded, after the selection procedures described in section 6.3 less than 3000 events with Q^2 greater than 100 GeV^2. Over 90% of the selected events – 26200 out of 28700 – have Q^2 values of less than 100 GeV^2. As there is a lower cut on Q^2 of 10 GeV^2 (section 6.3) a typical event therefore has a Q^2 value of some tens of GeV^2. (The distribution in x and Q^2 of the selected DIS

events is shown in figure 6.5, section 6.3.)

In this region, as with higher Q^2, the scattered electron is readily identified and well measured by the calorimeter, although more often than not it is outside the CTD tracking acceptance range.

The hadrons are another story. The QCD Compton or boson-gluon fusion processes, initial and final-state QCD radiation, final-state colour string interactions, and various non-perturbative hadronisation effects lead a wide variety of event topologies. In polar angle there is often a spread of energy between the current and target. Some of these events have just one or two poorly defined tracks, while others have a bewildering tangle. From the point of view of the calorimeter, it is open to definition whether the event has one jet, two or none at all.

However, even for such seemingly confused events, sensible kinematic measurements can be obtained from the calorimeter energy flow, while subsequent tracking analysis yields results which are consistent with those obtained from the calorimeter.

Moreover, while these events may not always be easy to understand individually, high-statistics analysis of their energy or momentum flow can provide considerable insight into the underlying QCD interactions which give them their somewhat complicated appearance.

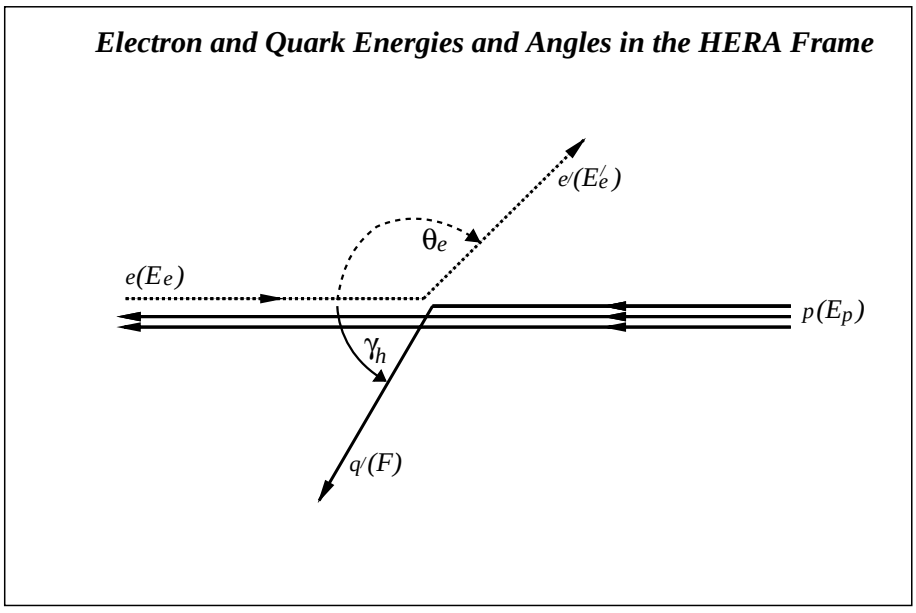

Figure 6.3: *DIS quark-parton model kinematics in the HERA laboratory frame, showing the scattering angles γ_h and θ_e of the electron and quark.*

6.2 Reconstruction of x and Q^2 at ZEUS

In the previous section two initial state and four final state variables were mentioned.
These are

E_e : Energy of the Initial Electron,
E_p : Energy of the Initial Proton,
E'_e : Energy of the Final Electron,
θ_e : Polar Angle of the Final Electron,
F : Energy of the Struck Quark, and
γ_h : Polar Angle of the Struck Quark.

However, since the standard variables used in DIS analysis are x and Q^2, these must be reconstructed in some way from the quantities measured in the detector. This is by no means a trivial task. Fortunately, since only two final state variables are necessary, and there are four to choose from, there are a number of possible options which can be selected according to the particular needs of the measurement.

6.2.1 Electron Method

The conventional method, employed in fixed target experiments, has been to use the angle θ_e and energy E' of the scattered lepton.

$$y_{elec} = 1 - \frac{E'_e(1 - cos\theta_e)}{2E_e} \tag{6.1}$$

$$Q^2_{elec} = 2E_eE'_e(1 + cos\theta_e) \tag{6.2}$$

$$x_{elec} = \frac{E_e}{E_p}\frac{E'_e(1 + cos\theta_e)}{2E_e - E'_e(1 - cos\theta_e)} \tag{6.3}$$

This method has the advantage that E'_e and θ_e can be obtained directly from measurement of a single energy deposit in the calorimeter (provided, of course, that the electron has been correctly identified).

However, there are some disadvantages. While it gives accurate reconstruction of Q^2, the accuracy of determination of x is poor for low values of y [31]. Moreover, the reconstructed event kinematics are extremely sensitive to systematic effects on the measurement of the electron. Of course, it cannot be used when the electron is not observed in the detector, either in charged current events, where the outgoing lepton is a neutrino, or at sufficiently low values of Q^2 ($\leq 4\,GeV^2$) for θ_e to be below the calorimeter acceptance.

6.2.2 Jacquet-Blondel Method

Use of the quantities F and γ_h associated with the struck quark presents the obvious difficulty that the quark is not directly observed. Ideally, F and γ_h might be obtained from measurement of the current jet but, as discussed in section 6.1, at HERA the current jet is seldom well-defined for Q^2 below $10^2\ GeV^2$.

Fortunately momentum conservation ensures that knowledge of F and γ_h is retained in the combined energies and momenta of the hadrons whether there is one jet, more than one jet, or no obvious jet at all.

Using the Jaqcuet-Blondel method [32], it is possible, therefore, to obtain x and Q^2 by summing over all energy deposits in the calorimeter, excluding that associated with the scattered electron.

$$y_{JB} = \frac{\Sigma_i(E_i - Pz_i)}{2E_e} \tag{6.4}$$

$$Q^2_{JB} = \frac{(\Sigma_i Px_i)^2 + (\Sigma_i Py_i)^2}{1 - y_{JB}} \tag{6.5}$$

$$x_{JB} = \frac{Q^2_{JB}}{s\ y_{JB}} \tag{6.6}$$

This method assumes that the vector sum of P_T associated with the target remnant can be neglected.

6.2.3 Measurement of γ_h

Expressed explicitly in terms of F and γ_h, equations 6.4 and 6.5 are equivalent to

$$y_{JB} = \frac{F(1 - cos\gamma_h)}{2E_e} \tag{6.7}$$

$$Q^2_{JB} = \frac{F^2 sin^2\gamma_h^2}{1 - y_{JB}} \tag{6.8}$$

from which

$$cos\gamma_h = \frac{Q^2_{JB}(1 - y_{JB}) - 4E_e^2 y^2_{JB}}{Q^2_{JB}(1 - y_{JB}) + 4E_e^2 y^2_{JB}} \tag{6.9}$$

Combining this formula with equations 6.4 and 6.5 gives

$$cos\gamma_h = \frac{(\Sigma_i Px_i)^2 + (\Sigma_i Py_i)^2 - (\Sigma_i(E_i - Pz_i))^2}{(\Sigma_i Px_i)^2 + (\Sigma_i Py_i)^2 + (\Sigma_i(E_i - Pz_i))^2} \tag{6.10}$$

Assuming that the vector sum P_T of the spectator jet and the jet mass can be neglected, it can be shown [33],[34] that the right hand side of equation 6.10 is equivalent to the energy weighted cosines of the current jet.

This method of extracting γ_h has the advantage of being relatively insensitive to fluctuations in energy measurement, even if part of the current jet is lost in the beam pipe [33].

6.2.4 Double-Angle Method

Combining γ_h, obtained as above, with θ_e gives a third possible way of reconstructing x and Q^2 [33].

$$Q^2_{DA} = \frac{4E_e^2 sin\gamma_h(1+cos\theta_e)}{sin\gamma_h + sin\theta_e - sin(\theta_e+\gamma_h)} \tag{6.11}$$

$$x_{DA} = \frac{E_e}{E_p}\frac{sin\gamma_h + sin\theta_e + sin(\theta_e+\gamma_h)}{sin\gamma_h + sin\theta_e - sin(\theta_e+\gamma_h)} \tag{6.12}$$

$$y_{DA} = \frac{sin\theta_e(1-cos\gamma_h)}{sin\gamma_h + sin\theta_e - sin(\theta_e+\gamma_h)} \tag{6.13}$$

At ZEUS it has been found that the double-angle method gives the best overall resolution in x and Q^2 over most of the kinematic plane. It has the advantages of being insensitive to the overall energy scale of the calorimeter, and of being less sensitive than other methods to QED radiative effects.

The double-angle method is used for reconstruction of event kinematics in this analysis.

6.3 Data Selection

A total integrated luminosity of $\approx 554\ nb^{-1}$ was recorded by ZEUS during 1993. Over 6 million events passed the third level trigger, described in chapter 2. Of these about 1.1 million were selected for the DIS group. These were written to a Data Summary Tape (DST) after which further selection took place offline to remove the considerable amount of remaining background contamination.

Background events may be roughly divided into two categories;

- those which are not valid events for the purpose of any physics analysis, either because they were not the product of genuine e-p collisions or because the detector was malfunctioning at the time, and
- those which result from e-p collisions but are the product of some process other than DIS.

There now follows a description of the principle sources of background and the selection procedures used to remove them.

6.3.1 Removal of Non-Physics Background

Detector Operation

The minimum requirement of detector functionality for this analysis was that:

- the CTD should be at full high voltage with no large dead regions and with fully operational readout;
- the magnet should be switched on;
- the calorimeter and its readout should be operational without a significant number of dead channels; and
- the luminosity monitor should be functioning.

Runs not satisfying these conditions were removed from the event sample.

Beam-induced interactions

A significant source of background is *beam-gas*, caused by interactions between the proton bunch and residual gas molecules in the beam-pipe vacuum. There can also be collisions between stray protons and beam-line components. Beam gas events typically have a large number of tracks at shallow polar angles with an apparent upstream vertex, and large early-arriving energy despoits in RCAL (see below).

Additional background is caused by the *halo muons* resulting from decaying pions created in beam-wall or beam-gas collisions. Halo muons are characterised

by energy deposited along the length of the calorimeter and in the muon chambers, and by an absence of CTD activity in the interaction region. Halo muons can also collide with beam-line components producing a forward-going spray of secondary particles similar to a beam-gas interaction.

Synchrotron radiation from the electron beam is predominantly produced in the curved sections of HERA, far from the experiments. A series of masks and collimators in the electron accelerator absorb the synchotron emissions and considerably reduce the rate of this type of background.

Calorimeter timing

A powerful means of distinguishing genuine e-p collisions from the beam-induced background is provided by calorimeter timing. The time measurements in the various regions of the calorimeter are offset, with respect to the HERA clock, so that anywhere in the calorimeter the measured arrival time of particles originating from the nominal interaction point is $t = 0$. Thus for genuine e-p collisions the the time measured by the FCAL and RCAL are $T_F = T_R = 0$. In contrast, for proton beam gas events which occur upstream from the interaction region, energy arrives in RCAL typically 10 ns earlier.

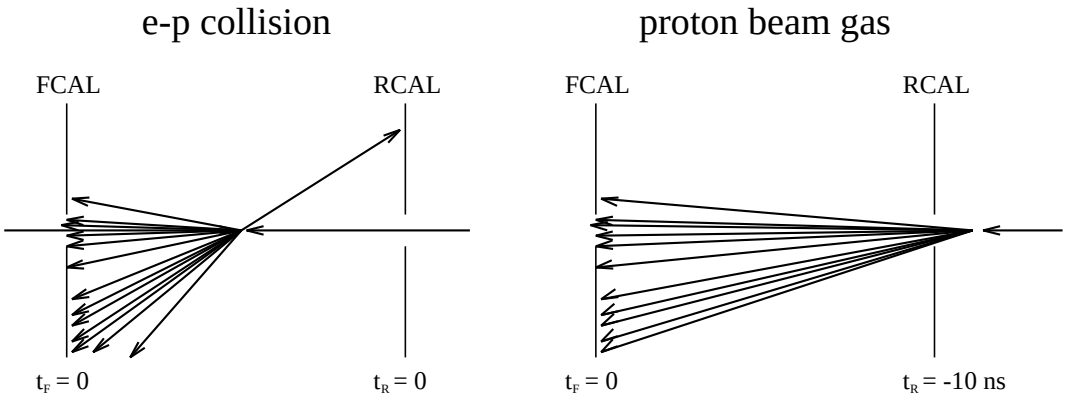

Figure 6.4: *Using calorimeter timing to eliminate beam-induced background.*

The event selection used in this thesis required that:

$$|t_R| < 3\ ns \qquad E_{RCAL} > 5\ GeV$$
$$|t_F - t_R| < 5\ ns \qquad E_{RCAL} < 5\ GeV$$

For high Q^2 events the electron is scattered into the BCAL or FCAL, and there is often very little energy in the RCAL. A looser timing cut for $E_{RCAL} < 5\ GeV$ is therefore required to prevent the rejection of high Q^2 events.

Event Vertex Position

The importance of reliable vertex measurement has been discussed in the previous chapter. Cosmic rays, and interactions of beam-associated particles with material inside the detector, are removed from this event sample by a requirement for the vertex position, obtained from the tracking system, to satisfy

$$-50 < z_{vtx} < 40\ cm \qquad \text{and} \qquad r_{vtx} = \sqrt{x_{vtx}^2 + y_{vtx}^2} < 10\ cm.$$

6.3.2 Removal of Non-DIS Physics Background

QED Compton

Elastic QED Compton events, $ep \rightarrow ep\gamma$, are used for luminosity measurement but are an unwanted background for DIS analysis These events were removed from the event sample using offline algorithms based on their event topology of two calorimeter energy deposits balanced in P_T, one with an associated track.

Photoproduction

The largest background to DIS comes from photoproduction. Due to the high cross-section for low-Q^2 interactions, ep physics is dominated by events for which the exchanged photon is quasi-real ($q^2 = -Q^2 \approx 0$). In this analyis there is a requirement that

$$Q^2 > 10\ GeV^2,$$

so for correctly reconstructed events the borderline region between photoproduction and DIS is avoided.

However errors in reconstruction can result in photoproduction events with low Q^2 values being misidentified as DIS events with higher Q^2 values. The main causes of this background and means of removing it are discussed below.

Electron Identification

In photoproduction events the electron is scattered at too shallow an angle to be detected in the calorimeter, so, while about 20% of photoproduction events are tagged by the luminosity monitor, the chief means of distinguishing photoproduction from neutral current DIS events is the absence of a scattered electron in the detector.

At ZEUS electrons are identified using calorimeter information alone. The identification procedure [35] is based on the differences between the shower profiles formed by electrons, hadrons and muons.

Photoproduction events can be mistaken for DIS if an energy deposit in the electromagnetic calorimeter, possibly the result of a π^0 decay, is wrongly identified as belonging to an electron. This is a problem at low x, Q^2, where both γ_h and θ_e

point towards the rear of the detector, so that there is an overlap of the regions in which the electron and hadrons are observed.

In light of the magnitude of the photoproduction background, the choice of electron-finding algorithm for use in this analysis (EEXOTIC) was on the basis of purity rather than efficiency. Studies using Monte Carlo techniques [36] have shown that at $E'_e = 10 GeV$ EEXOTIC has an efficiency of 67% and purity of 97%. For $E'_e > 20\ GeV$ the efficiency and purity are above 98% and 99% respectively.

The electromagnetic showers from π^0 decays typically have lower energy than genuine scattered electrons, except at high y, so a cut on the measured energy of the scattered electron helps to reduce the background. For this study the electron was required to have

$$E'_e > 10\ GeV.$$

Low x, Q^2 events with fake electrons in the forward direction are removed by requiring

$$y_{elec} < 0.95$$

The expected rate for genuine DIS events in the excluded kinematic region is extremely low. For $E'_e > 10\ GeV$ this cut has no effect on electron candidates with $\theta > 42.8°$, and therefore there is no danger of removing events with genuine electrons in the BCAL and RCAL.

Momentum Conservation – δ

Photoproduction background can be further reduced using the quantity

$$\delta = \Sigma_i (E_i - Pz_i + 2E_\gamma) \tag{6.14}$$

where the sum is over all calorimeter cells, E_i is the measured energy in cell i, Pz_i is given by $E_i cos\theta_i$, and where E_γ is the energy measured in the photon calorimeter of the luminosity monitor.

If all outgoing particles from an ep collision were observed in the detector, momentum conservation would require that

$$\Sigma_i (E_i - Pz_i) = (E_p + E_e) - (Pz_p - Pz_e) = 2E_e \tag{6.15}$$

or, allowing for intial state radiation of a photon of energy E_γ,

$$\Sigma_i (E_i - Pz_i + 2E_\gamma) = 2E_e \tag{6.16}$$

Since particles in the forward beam pipe, having $E \approx Pz$, make little contribution to the above sum, for neutral current DIS events δ should have a value of nearly twice the electron beam energy. Photoproduction events typically have significantly lower values of δ due to the scattered electron being undetected in the calorimeter.

This analysis required that

$$\delta > 35\ GeV.$$

6.3.3 Removal of Events with Reconstruction Problems

In some categories of event the kinematic variables cannot be reconstructed with sufficient reliability to allow inclusion in a physics analysis.

Hadronic Activity

The accuracy of recontruction using the *double-angle* method (section 6.2.4) is limited by the accuracy with which γ_h can be reconstructed. Reconstruction of γ_h from the Jaquet-Blondel variables (equation 6.10, section 6.2.3) deteriorates when there is little hadronic P_T, a condition which also gives a low value of y_{JB} (equation 6.4). This analysis therefore required that

$$y_{JB} > 0.04$$

to exclude events with insufficient hadronic activity in the detector to enable reliable reconstruction.

Electron Acceptance

In events where the electron is scattered at a shallow angle so that it is detected in the RCAL close to the beam pipe hole, the shower in the calorimeter may be partially lost, leading to degradation of measurement of the electron energy and angle. To remove events with this kind of acceptance problem, the impact point of the scattered electron was required to be more than a minimum distance away from the beam pipe hole specified by the box cut:

$$|x| > 16\ cm\ and\ |y| > 16\ cm.$$

In addition, since there is a close correlation between θ_e and Q^2 (section 7.1.3), the requirement that $Q^2 > 10\ GeV^2$ (section 6.3.2) effectively rules out the kinematic region for which electron acceptance in the calorimeter is problematic.

6.3.4 Selected Final DIS Sample

After the above selection procedures, 28700 events remained in the sample. Figure 6.5 shows how they are distributed in x and Q^2 (as reconstructed by the double-angle method), and in relation to a set of bins, described in section 7.4.1, which are extensively used within ZEUS physics. Some further cuts were imposed at a later stage to satisfy tracking acceptance requirements specific to momentum flow studies. They are described in sections 7.3.

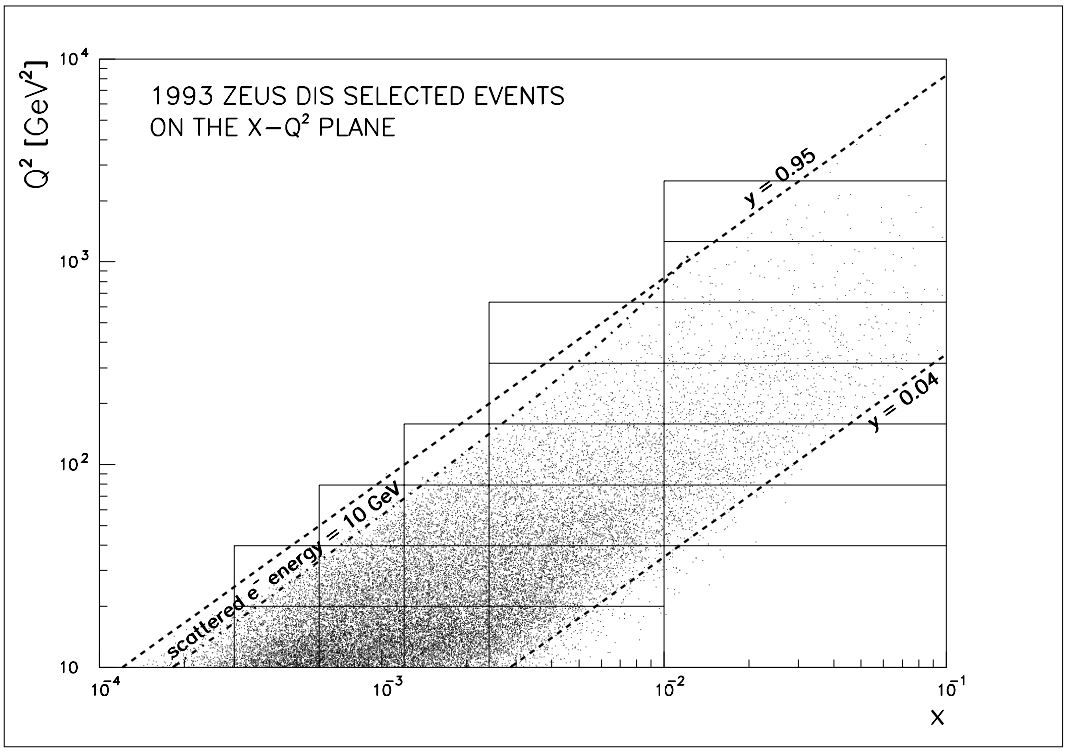

Figure 6.5: *Events passing the DIS selection criteria, shown on the x-Q^2 plane. Also shown are the standard ZEUS DIS analysis bins.*

6.4 Monte Carlo Simulation

6.4.1 Event Simulation

Physics Simulation

Monte Carlo simulation is a valuable tool for the analysis of high energy scattering experiments. A Monte Carlo event generator simulates physics processes by selecting the event type and computing its relevant subprocesses according to the cross-sections predicted by a given theoretical model.

Simulation of DIS takes place in three steps. First the exact matrix element, which may include first-order QCD corrections, is calculated. Then the higher order corrections, giving rise to a parton cascade, are simulated using models based on the Leading Log Approximation (LLA) [37]. Finally nonperturbative hadronisation into the colourless final state and subsequent decays of short-lived particles are simulated.

The result is a complete set of four-vectors of the final state particles, which can then be input into the detector simulation program.

Detector Simulation

As mentioned in chapter 4, the action of the ZEUS detector is simulated by the MOZART Monte Carlo, based on GEANT. Four-vectors from the event generator are tracked through the detector, fully simulating interactions with material in the detector, acceptance, detector response and signal quality. Triggering is also simulated, by the ZGANA [14] program.

In addition to the four-vector "truth" information, MOZART outputs "raw data" digitisations which are in an identical form to those originating from the readout electronics of the genuine ZEUS detector. The MOZART output is thus able to be processed by the same offline reconstruction software (ZEPHYR) as is used for real raw data.

6.4.2 Monte Carlo Models

Three Monte Carlo datasets were used in this analysis, each based on a particular theoretical prescription. They are as follows.

ARIADNE

The ARIADNE dataset consists of 200,000 neutral current DIS events with $Q^2 > 4GeV^2$. The proton structure function was parametrised by MRSD-' [38], a set of parton distribution functions which have been found to give a good description of the HERA measurement [7],[8] of the proton structure function.

The hard scattering process was generated using LEPTO 6.1 [39]. Interfaced to LEPTO, ARIADNE 4.03 [40] was used to simulate the QCD cascade, in accordance with the colour-dipole model (CDM), in which the gluon emission is treated as dipole radiation from a point-like struck quark and an extended proton remnant. Recursively, further dipoles may form between the gluon and struck quark, and between the gluon and proton remnant.

Boson-gluon fusion is not included in the CDM, so a provision within ARIADNE was used to add this process as given by the first order matrix element within LEPTO.

Initial and final state photon radiation effects were accounted for by the HERACLES 4.4 program [41], which was interfaced to LEPTO via the DJANGO 6.0 [42] program.

The formation of colourless hadrons from the final state partons was via the Lund string model [43], as implemented in the JETSET [44] program. In this model, the colour force acts as a "string" between one quark and another. As the quarks move apart, the string is stretched until it is energetically more favourable for a new pair of quarks to be formed in between them, causing the string to "break" into colourless hadrons.

MEPS

A second sample of 200,000 DIS events with $Q^2 > 4GeV^2$ was generated, with the proton structure function parametrised by the GRV(LO) [45] parton distribution functions. Once again LEPTO was used to calculate the hard scattering processes, and as before HERACLES was used for the electroweak corrections.

For this dataset the parton cascade was simulated within LEPTO itself, using an option in which the initial and final state parton showering is restricted in phase space by the first-order matrix element. This configuration is generally referred to as "Matrix Element plus Parton Showers" (MEPS).

Again, at the hadronisation stage the Lund string model was used.

HERWIG

The HERWIG 5.7 generator [46] was used to produce a third sample, consisting of 100,000 DIS events with $Q^2 > 4GeV^2$, using the MRSD-' structure function parametrisation, this time without electroweak corrections.

In the HERWIG model the QCD cascade is modelled using parton showers alone. For the nonperturbative hadronisation a cluster model [47] is used instead of string fragmentation.

Chapter 7

Momentum Flow in the Laboratory Frame

7.1 Introduction to Energy/Momentum Flows

7.1.1 A Test of QCD Radiation

Although many of the events observed in ZEUS during 1993 do not have well-defined jets, the angle γ_h, equivalent to that of the struck quark in the naive quark-parton model, can nonetheless be reconstructed from the distribution of hadronic energy in the calorimeter, and with sufficient accuracy to be used routinely in the reconstruction of ZEUS event kinematics.

This demonstrates that even in the rather "messy" events encountered particularly at low Q^2, a correlation with the kinematics of the original collision is still very much in evidence.

The nature of this relationship is complicated. While there are apparent variations with x and Q^2 introduced by the boost from a virtual photon-proton aligned frame to the HERA lab frame, there are also intrinsic x and Q^2 dependences resulting from hard and soft QCD processes. Different theories of QCD interaction make different predictions about the distribution of energy in the detector, so studying energy or momentum flow provides a useful way of discriminating between models.

7.1.2 Energy Flow in the HERA Frame

In the simplest case of the quark-parton model, with independent fragmentation of the struck quark and target, most of the energy in the detector, excluding that associated with the electron, is correlated with the direction of the struck quark. Energy associated with the target generally disappears into the forward beam pipe.

Colour-string interaction between the struck quark and spectator quarks produces some energy in between the current and target.

Higher-order QCD processes introduce the possibility of more than one jet, and make correlation of energy with the current direction less pronounced.

7.1.3 Evolution of γ_h and θ_e with x and Q^2

The appearance in the detector of the hadronic energy flow is affected by γ_h. As γ_h decreases, separation between the current and target peaks decreases. At small and large values of γ_h effects of detector acceptance become significant, particularly for tracking.

Figure 7.1 shows how γ_h and θ_e vary with x and Q^2 within the kinematic region covered by the standard ZEUS DIS analysis bins. It can be seen that the quark angle γ_h decreases (moves forward in the detector) with increasing x at constant Q^2 and increases (moves backward in the detector) with increasing Q^2 at constant x. The electron angle θ_e increases with increasing x at constant Q^2 and decreases with increasing Q^2 at constant x. The dominant overall effects are the x dependence of γ_h and the Q^2 dependence of θ_e. This is shown in figure 7.2. The hadron and electron angles are expressed in terms of their corresponding pseudorapidity variables, η_h, given by $-ln(tan\frac{\gamma_h}{2})$, and η_e given by $-ln(tan\frac{\theta_e}{2})$. In figure 7.2 η_h is plotted against $log_{10}x$, integrated over all Q^2, and η_e against $log_{10}Q^2$ integrated over all x.

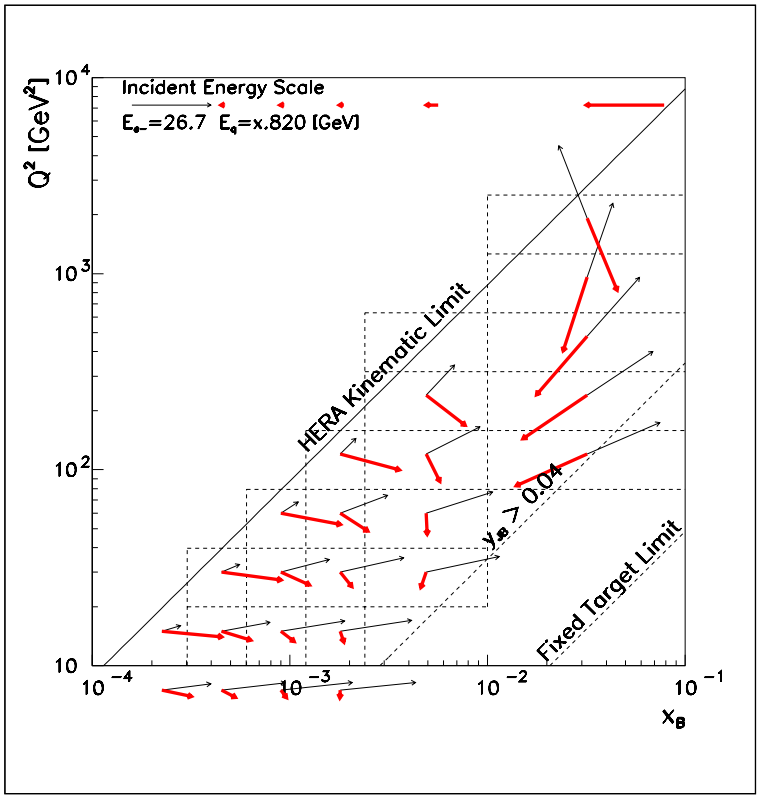

Figure 7.1: *Kinematic vectors showing the average angle and energy of the scattered electron (θ_e,E'_e) and struck quark (γ_h,F) in the standard ZEUS DIS analysis bins.*

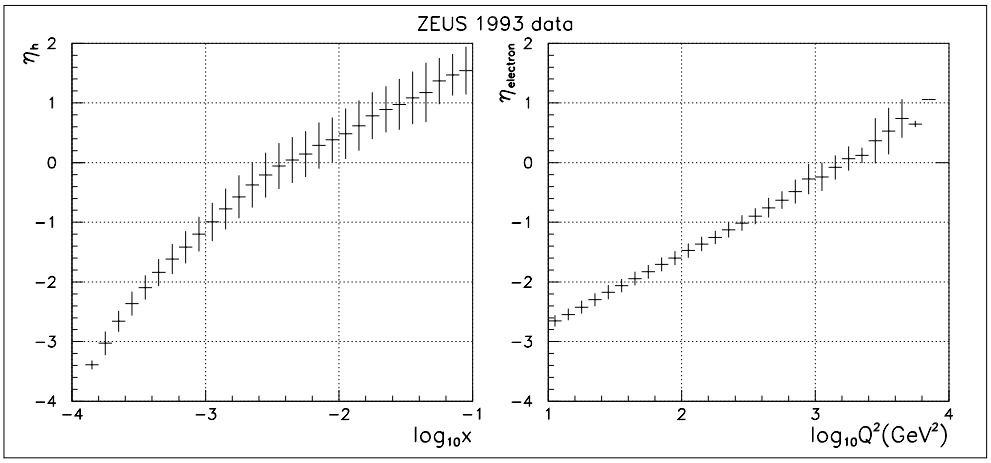

Figure 7.2: Left*: Correlation of the hadron angle η_h with x.* Right*: Correlation of the electron angle η_e with Q^2. The error bars show the spread of the distribution.*

7.2 Measurement of Momentum Flow

7.2.1 Why Use Charged Tracks?

Energy flow can be measured in the calorimeter in terms of cell angle (defined by a line from the event vertex to the geometric centre of the cell) and energy, or alternatively in the CTD in terms of track angle and momentum. Each has advantages and drawbacks; the reason for the complexity of high energy physics detectors such as ZEUS is, of course, the complimentarity of the information which the various sub-detectors provide.

The calorimeter can measure the total energy flow, from charged and neutral particles, between 2.2° and 176.5° in polar angle. The tracking acceptance range is far more limited (see below), and tracking can detect only charged particles. However, tracking can assign energy to individual particles, and can differentiate between energy originating from the event vertex and that coming from elsewhere.

Tracking gives better angular resolution than calorimetry, particularly in azimuth, where tracking resolution is at its best, whereas, in the calorimeter, there is a loss resolution for low momentum charged particles due to curvature in the magnetic field.

For 1993 tracking data, there is the added interest that this is the first available ZEUS data with fully operational tracking. Previous chapters have been devoted to technical aspects of tracking, and possible sources of systematic error have been discussed. However, the ultimate test of the tracking is whether or not it enables a physics analysis. The study of momentum flows also provides an interesting opportunity to see whether the calorimeter and CTD give a consistent picture of ZEUS events.

7.2.2 Momentum Flow Variables

The focus of this thesis is on tracking data, so the flow variables are defined below in terms of measured angle and momentum of a charged track. However, they are equally valid for calorimeter cell angle and energy. For both calorimeter and tracking, the reference angles γ_h (or η_h) and $\phi_{electron}$ are obtained using calorimeter data. Measurement of γ_h is described in chapter 6, section 6.2.3. The electron x-y co-ordinates are obtained from calorimeter measurement, and from these $\phi_{electron}$ is measured with respect to the tracking vertex.

Pseudorapidity – $\Delta\eta$

Looking at polar angle correlations with γ_h, it is customary to use pseudorapidity, which is relatively insensitive to longitudinal boosts. The pseudorapidity η of a

track at polar angle θ is given by

$$\eta = -ln(tan(\frac{\theta}{2})) \tag{7.1}$$

so that the hadron angle, expressed in pseudorapidity, is

$$\eta_h = -ln(tan(\frac{\gamma_h}{2})) \tag{7.2}$$

The separation in pseudorapidity between a given track and η_h is now defined as

$$\Delta\eta = \eta_{track} - \eta_h. \tag{7.3}$$

Tracks which are correlated with the nominal direction of the struck quark will have a distribution in $\Delta\eta$ which peaks at zero. Tracks associated with the target will generally be at very small angles to the forward proton direction, giving large values of η and positive values of $\Delta\eta$. For the kinematic range encompassed in this study, the electron is typically further back in the detector than the struck quark, i.e, θ_e, measured with respect to the forward proton direction, is usually larger than γ_h. Therefore electron tracks will have negative values of $\Delta\eta$.

The momentum flow is obtained by weighting the particle flow by track momentum P. Momentum associated with the current gives a peak at zero, momentum associated with the target peaks at large positive values, while momentum associated with the scattered electron gives a peak at negative $\Delta\eta$.

Normalised by the total number of events N_{evts} in a given x-Q^2 bin, the particle and momentum flows, as functions of $\Delta\eta$, are defined as $\frac{1}{N_{evts}}\frac{dN}{d\Delta\eta}$ and $\frac{1}{N_{evts}}\frac{dP}{d\Delta\eta}$ respectively.

Azimuth – $\Delta\phi$

In azimuth, P_T conservation ensures that the nominal direction of the struck quark is 180° from that of the scattered election. Azimuthal correlation of hadron tracks with the struck quark direction is therefore indicated by a peak at π in the distribution of $\Delta\phi$, transverse momentum correlation by a peak in the P_T-weighted distribution of $\Delta\phi$, where

$$\begin{aligned} \Delta\phi = \quad & |\phi_{track} - \phi_{electron}| \qquad for\ |\phi_{track} - \phi_{electron}| < \pi \\ & 2\pi - |\phi_{track} - \phi_{electron}| \quad for\ |\phi_{track} - \phi_{electron}| > \pi \end{aligned} \tag{7.4}$$

such that $\Delta\phi$ always runs from 0 to π. The P_T associated with the current produces a peak at $\Delta\phi = \pi$, whereas P_T associated with the target has no azimuthal correlation and forms a uniform pedestal to the distribultion. The P_T associated with electron tracks gives a spike at $\Delta\phi = 0$.

Normalised by the number of events N_{evts} in an analysis bin, the particle and momentum flows, as functions of $\Delta\phi$ are given by $\frac{1}{N_{evts}}\frac{dN}{d\Delta\phi}$ and $\frac{1}{N_{evts}}\frac{dP_T}{d\Delta\phi}$ respectively.

7.3 CTD-Specific Selection Requirements

As discusssed in chapter 5, the absence of tracking chambers to the front and rear of the detector limited the polar-angle acceptance for tracking, providing something of a challenge for 1993 ZEUS tracking studies.

The selection procedures described in chapter 6 were designed to provide a sample of good-quality DIS events, with minimum background contamination, for general analysis. For analysis using CTD tracks, further selection cuts are advisable to take account of CTD acceptance and to exclude poor-quality tracks.

7.3.1 Track Quality Cuts

In chapter 5 it has been shown that there is a significant deterioration on the quality of tracking where P_T is low or where the polar angle is shallow, and that it is gererally sensible to restrict analysis to tracks with $P_T > 200MeV$ and $-1.5 < \eta_{track} < 1.5$.

These cuts have been adopted by ZEUS as a guideline for tracking studies in general. However, requirements vary according to the nature of the analysis.

For momentum flow studies there are the particular considerations that

- due to the momentum weighting, measurement of momentum flow is disproportionately affected by badly measured high-momentum tracks, and is vulnerable to the effects spurious straight tracks,

- measurement of momentum flow is relatively insensitive to the effects of individual badly measured low-momentum tracks, and

- given that the limits on η_h need to be be considerably tighter than those on η_{track} (see below), a cut of $|\eta_{track}| < 1.5$ cut is rather restrictive.

For this study the cut of $|\eta_{track}| < 1.5$ was replaced by a cut of $NDF > 10$. This cut requires a track to pass through at least the first two superlayers of the CTD, extending the hard limit on polar angle to $-1.9 < \eta_{track} < 1.9$, and also eliminates, at all measured values of η, the problematic "ficticious" tracks, composed of a few hits, which can have very large measured momentum. It is sufficiently loose that there is little effect from the systematic reduction in the NDF of negative tracks, discussed in chapter 5, which was not incorporated into the 1993 detector simulation.

The $P_T > 200\ MeV$ cut was retained. An additional cut of $P < 50\ GeV$ was imposed, to eliminate spikes in the momentum flow caused by a a very few straight tracks with random measured momentum values of $\sim 10^2$ or $\sim 10^3\ GeV$.

7.3.2 Effects of Acceptance on Momentum Flow

For momentum flow analysis, in addition to the question of loss or degradation of individual tracks, there is the event-wide consideration of possible bias to the momentum flow distribution if the reference angle, η_h, is close to or beyond the tracking acceptance limit.

It is therefore necessary, in addition to restricting analysis to the kinematic regions in $x - Q^2$ for which tracking acceptance is generally good, to impose hard limits on the permitted values of η_h.

7.3.3 Limits on η_h

For this study, η_h was restricted to between -1.25 and $+1$. This gives almost a unit of pseudorapidity between the maximum value of η_h and the upper edge of the tracking acceptance.

However, at large positive values of $\Delta\eta$, i.e. in the direction of the remnant, there are unavoidable acceptance losses which are described in section 7.8.2.

The minimum value of η_h is closer the lower edge of the tracking acceptance.

Due to the forward shift of the current peak, described in section 7.5, there are very few hadron tracks observed with negative values of $\Delta\eta$. This is observed in ZEUS data (section 7.6), and in both the generated and reconstructed Monte Carlo distributions (section 7.8.2). As a result it is reasonable to assume that, provided that η_h is not outside of the tracking acceptance range, losses in the rear direction are small.

The negative limit on η_h, therefore, can be extended to -1.25 without introducing a significant bias to the momentum flow. This allows analysis to cover a wider range in x.

7.4 Analysis Bins

7.4.1 Standard ZEUS DIS Bins

Initial consideration of analysis bins for this study was based on a set of bins, first adopted to measure the proton structure function, F_2, using 1992 data [7], which are now in standard use among many ZEUS physics analysis groups.

x			Q^2 (GeV^2)		
0.0003	–	0.0006	5	–	10
0.0006	–	0.0012	10	–	20
0.0012	–	0.0024	20	–	40
0.0024	–	0.01	40	–	80
0.01	–	0.1	80	–	160
0.1	–	1.0	160	–	320
			320	–	640
			640	–	1280
			1280	–	2560
				$>$	2560

Table 7.1: *ZEUS DIS analysis bins in x and Q^2.*

The choice of analysis bins at low (x, Q^2) was motivated by the resolution in x and Q^2 obtained from reconstruction by the double-angle method. At higher values of x and Q^2 the bin sizes are larger to allow higher event statistics in each bin.

However, these bins tailored primarily to the requirements of ZEUS calorimeter data. Many bins are severely eroded, some completely depopulated, when tracking acceptance, and in particular the η_h cut, is taken into account.

7.4.2 Event Acceptances in Analysis Bins

Good event acceptance in each analysis bin is important if, as is the case for this study (section 7.8.2), detector effects are to be corrected using Monte Carlo techniques which correct the data back to the full phase space defined by a given

x-Q^2 region. If the $x - Q^2$ distribution in a reconstructed bin is significantly different from that in the corresponding true bin, it is difficult, comparing the two distributions, to separate detector effects from kinematic effects. Furthermore, correcting back to a region of phase space which is unobserved in the data introduces a dependence on the model used to generate the Monte Carlo distribution.

A Monte Carlo study was undertaken at the generator level using ARIADNE (section 6.4.2) to measure acceptance due to the combined effects of the kinematic cuts used in event selection, which are

$0.04 < y < 0.95$

$E'_e > 10\ GeV$

$-1.25 < \eta_h < 1.0.$

Event acceptance in each analysis bin is defined as

$$Acceptance = \frac{No.\ of\ events\ which\ satisfy\ cuts}{No.\ of\ events\ generated} \tag{7.5}$$

The results are seen in figure 7.3.

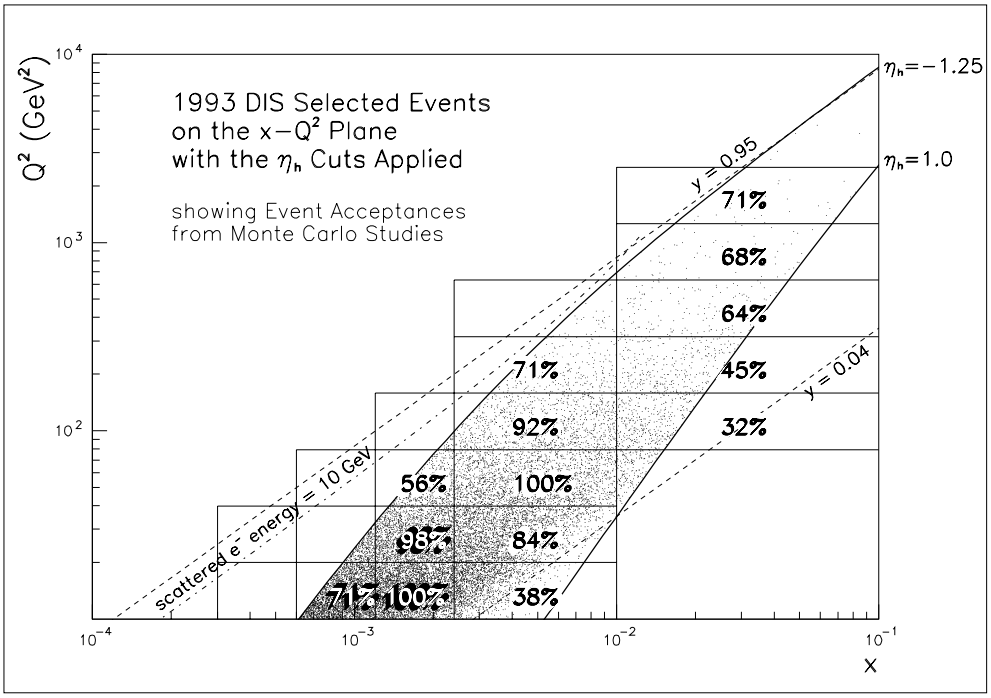

Figure 7.3: *Events passing the DIS selection criteria, described in Section 6.3 , shown on the x-Q^2 plane, with additional cuts in η_h to minimise bias to momentum flows within the tracking acceptance range. Also shown are event acceptances in the standard ZEUS DIS analysis bins.*

The Effect of the η_h Cut

The effect of the η_h cut on the selected DIS sample is dramatically evident in figure 7.3. The lowest $x-Q^2$ bin has been completely depopulated, while acceptance in the highest x bins is generally poor.

Since this thesis investigates the x-dependence of momentum flow, and the changes which occur as γ_h moves progressively forward in the lab frame, it is desirable to retain as wide a range in x with as can accomodate the requirement for good event acceptance within each defined kinematic region.

To achieve this, the upper two x bins in table 7.1 were modified from

$$x = 0.0024 - 0.01,\ x = 0.01 - 0.1$$

to

$$x = 0.0024 - 0.0072,\ x = 0.0072 - 0.03$$

Any $x - Q^2$ bin for which the event acceptance was less than 67% was then removed from the analysis.

Figure 7.4 shows the modified x bins and event acceptances in the x-Q^2 bins which were retained for the analysis.

7.4.3 Final Choice of Bins

The resulting four analysis bins were used for this study are defined by their x values, integrated over all Q^2 bins for which acceptance was reasonable. Tabulated below are the x bins and their corresponding Q^2 ranges.

x	$Q^2\ (GeV^2)$
0.0006 – 0.0012	10 – 20
0.0012 – 0.0024	10 – 40
0.0024 – 0.0072	20 – 160
0.0072 – 0.03	80 – 1280

Table 7.2: *Final choice of analysis bins in x, integrated over the Q^2 bins for which acceptance is reasonable.*

Event acceptances in these bins, all of which are over 70%, are shown in figure 7.5.

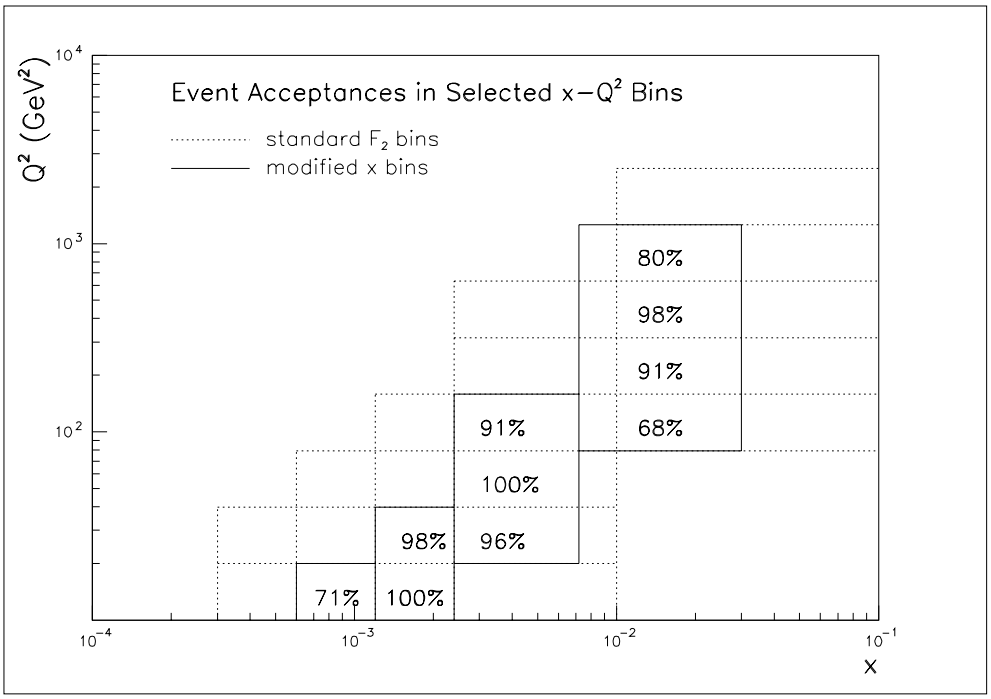

Figure 7.4: *Event acceptances in each x-Q^2 bin, after modification of the x bins to take account of tracking acceptance.*

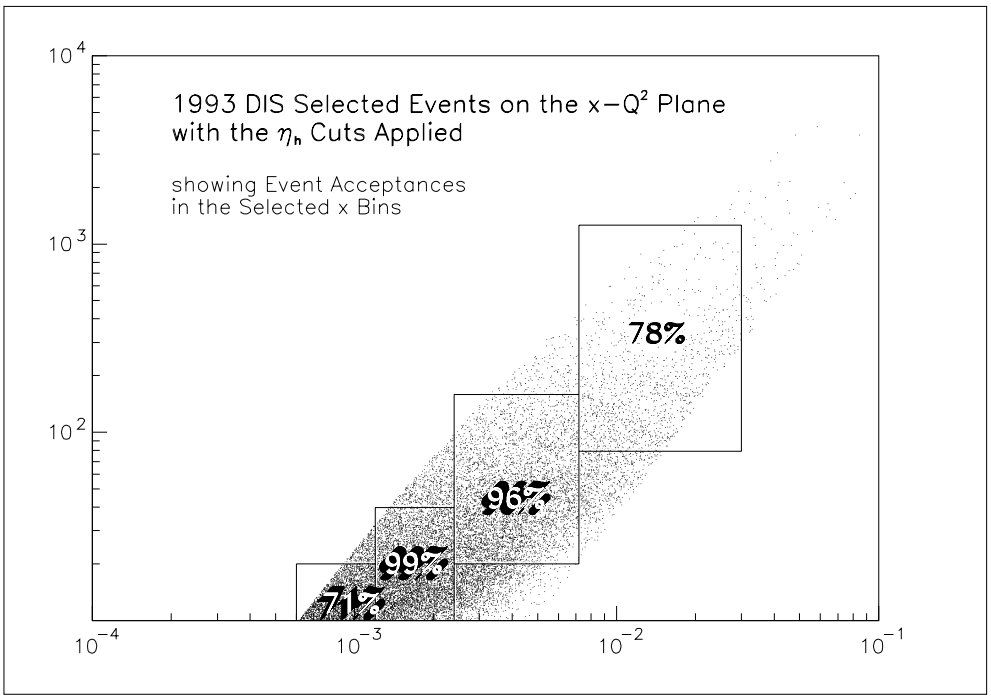

Figure 7.5: *Event acceptances in the x bins chosen for the momentum flow analysis.*

7.5 Momentum Flows in Pseudorapidity

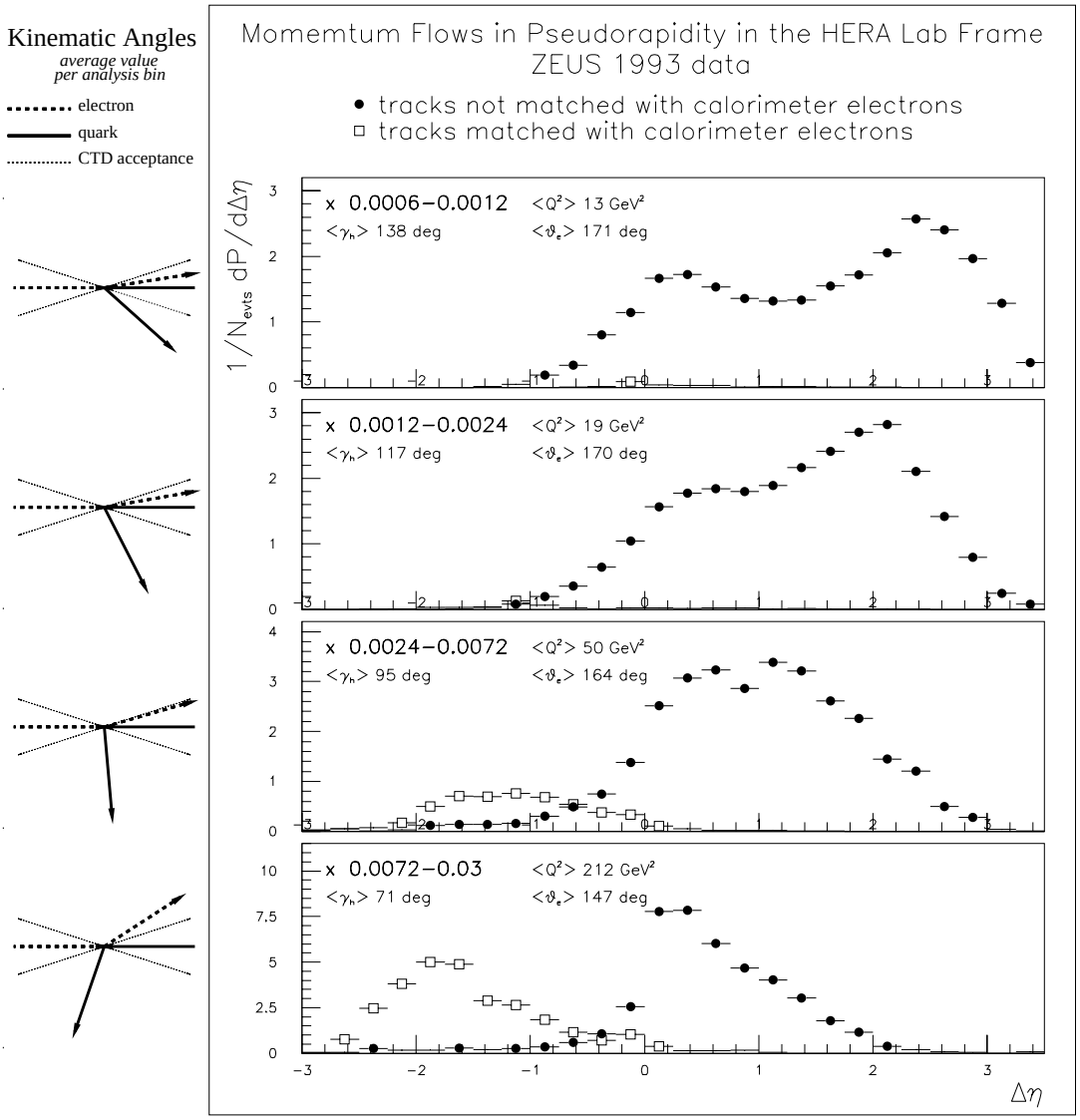

Figure 7.6: *Momentum flow versus $\Delta\eta$, uncorrected for detector effects. On the left, the solid and dashed arrows represent the average values for γ_h and θ_e respectively, for each x bin.*

Figure 7.6 shows momentum flow versus $\Delta\eta$ for 1993 ZEUS DIS data, without any corrections for event selection or detector acceptance, in the four x bins described in section 7.4.3.

Separate distributions are shown of electron tracks, which were excluded from subsequent analysis, and of hadron tracks.

Electron tracks were identified by "matching" [48] with the energy cluster in

the calorimeter which had been identified as belonging to the scattered electron (section 6.3.2).

The trajectories of all charged tracks within a cone of 15° of the electron cluster were extrapolated to the calorimeter using Runge-Kutta-Nystrom integration to take into account the affect of the magnetic field. A track and cluster were considered to be "matched" if they were separated by 20 cm or less.

All tracks which had not been matched with calorimeter electrons were regarded, in subsequent analysis, as hadron tracks.

7.5.1 Hadron Tracks

The hadron momentum flow with respect to pseudorapidity has a characteristic two peaked structure. One peak is close to $\Delta\eta = 0$, indicative of track momentum correlated with the nominal direction of the struck quark, while the second is at large η, (limited by acceptance), as would be expected from tracks associated with the target, correlated with the direction of the proton and the forward beam pipe.

In the lowest x bin of figure 7.6, the struck quark and target remnant are far apart in polar angle (and therefore pseudorapidity) in the HERA lab frame. In this bin γ_h points backwards in the detector, at a large angle (138° average) from the proton direction. Consequently the current and target peaks are well-separated in $\Delta\eta$.

A notable feature is that the peak associated with the current is not centred at zero but is shifted forward by half a unit of rapidity in all but the highest bin. This has also been observed in other energy flow studies with the calorimeter [49],[50] and with charged tracks [50]. This forward shift of the current peak, together with the not inconsiderable energy observed between the current and target, is believed to be caused by soft QCD radiation. In this context, the predictions of Monte Carlo models is discussed in section 7.7.

Moving upwards in x, γ_h moves forwards in the lab, so that each successive bin brings the target and current peaks closer together in $\Delta\eta$, while an increasing part of the target is lost beyond the forward tracking acceptance region.

In the highest x bin, γ_h points forwards, with an average value of 71°. In this bin the target peak is not visible, and, as will be shown, the current peak also begins to be affected by tracking acceptance. The forward shift of the current peak observed in the lower bins is absent here, the peak of the distribution being close to zero. This has also been observed in calorimeter studies [49], and is expected, due to the relatively high average x and Q^2 of this bin. At higher x, Q^2 the kinematics of the scattering are less affected by gluon radiation between the current and the proton remnant, and so the forward shift of the current peak is reduced.

The height of the current peak increases progressively from the lowest bin to the highest. The average value of Q^2 increases from 13 GeV^2 in the lowest x bin to 212 GeV^2 in the highest. At higher values of Q^2, as the electron is scattered

further forward in the detector, and its P_T increases. The momentum of the hadronic system also increases, balancing in P_T with the electron.

7.5.2 Electron Tracks

The scattering angle of the electron in the HERA lab frame, and hence the CTD acceptance for the electron track, is strongly dependent on Q^2.

For the two lowest bins in figure 7.6, the average Q^2 is below 20 GeV^2, and most of the electrons are outside of the CTD acceptance. In these two bins, therefore, very few tracks are matched with calorimeter electron deposits, and very few tracks appear in the in the negative region of $\Delta\eta$ where electron tracks would be expected.

The second highest bin has an average θ_e of 164°, which is on the borderline of CTD acceptance. The highest bin, for which hadron track acceptance is poor, has good acceptance from the point of view of electrons. For these two highest bins, matching of tracks with calorimeter electron deposits gives a distinctive distribution of electron tracks, with a well-defined peak shifted by about two units of pseudorapidity backwards from the current peak.

7.6 Diffractive DIS Events

An unexpected class of events has been observed at HERA, initially in 1992 by ZEUS [51] and confirmed by H1 [52]. These events have the characteristics of diffractive DIS. They comprise about 7 –8% of the ZEUS 1993 DIS sample.

Diffractive processes are generally understood to proceed through the exchange of a colourless object, with the quantum numbers of the vacuum, and which carries energy-momentum, generically called the pomeron. However, the true nature of the pomeron is far from clear.

The absence of colour flow between the struck quark and the proton gives a distinctive event topology characterised by a large gap in rapidity between the forwardmost energy associated with the current hadronic final state and the energy associated with the proton remnant. These events are therefore often referred to as Large Rapidity Gap (LRG) events.

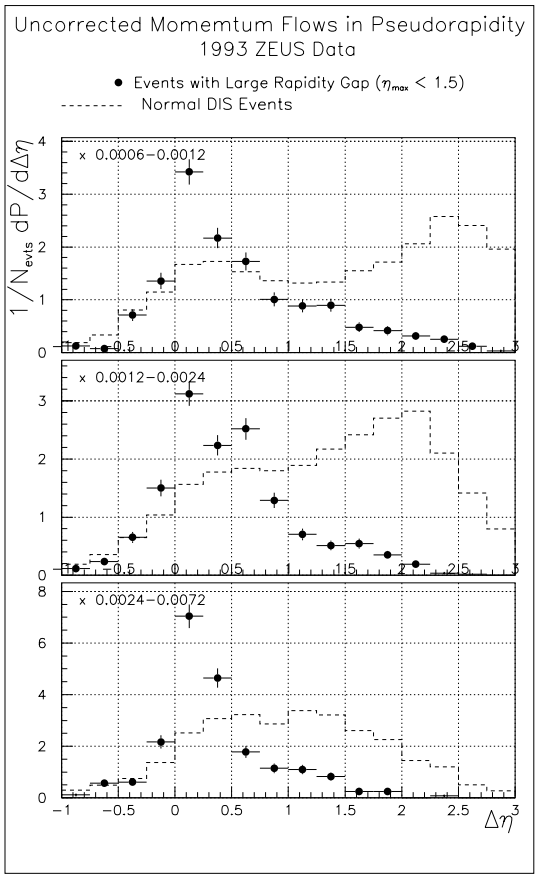

Figure 7.7: *Momentum flow versus $\Delta\eta$ for diffractive DIS events.*

Diffractive DIS events are defined in this analysis as those for which there are no energy deposits above 0.4 GeV detected in the calorimeter at values of pseudorapidity greater than 1.5.
Normal DIS events have large energy deposits surrounding the forward beam pipe, associated with QCD radiation from the target remnant. Figure 7.7 shows track momentum flow versus $\Delta\eta$ for events which have been classified as diffractive events on the basis of calorimeter data. It is immediately apparent that for these events the tracking gives a similar picture to the calorimeter, showing very little momentum in the forward direction. The momentum flow is strikingly different from that of normal DIS events (superposed). There is a complete lack of energy in the target direction. The current peak is far more pronounced than for normal DIS events, and there is no forward shift, the peak being at $\Delta\eta = 0$ even for the lowest x bin.

These characteristics, which have also been observed in energy flow studies with calorimeter data [49],[50], are consistent with there being reduced QCD radiation between the current and target.

7.7 Comparison with Monte Carlo Models

7.7.1 Momentum Flow Comparisons

The momentum flow distributions shown in figure 7.6 were compared with the corresponding distributions obtained from Monte Carlo datasets based on three theoretical models, HERWIG, ARIADNE and MEPS, described in section 6.4.2, after they had been passed through a full simulation of the detector, trigger, offline reconstruction and offline selection. The results are shown in figure 7.8.

ARIADNE and HERWIG both describe the current peak well. In the lowest bin, HERWIG overstimates the forward region associated with the remnant, while in the second lowest bin ARIADNE underestimates it. The MEPS distribution seriously underestimates the forward region in both of the lower two bins, and in the second lowest bin appears also to underestimate the forward shift of the current peak.

In the second highest bin, little of the forward region is within range of the CTD tracking, but that which is appears to be underestimated by all three Monte Carlo models. In the highest bin only the current peak is visible within the CTD. HERWIG and ARIADNE describe the data well but MEPS makes the peak narrower and higher than is observed in the data.

7.7.2 Particle Flow Comparisons

The unweighted particle flow distributions of figure 7.9 show how multiplicity is distributed in $\Delta\eta$.

Comparing figures 7.8 and 7.9, it is noticeable that there are distinct current and target peaks in the momentum flow but not in the particle flow. The particle flow is essentially flat in the forward direction, within the limits of detector acceptance. This shows that the region of pseudorapidity between the current and remnant is fairly uniformly populated by particles. The current and target peaks result not from greater concentrations of particles, but from a tendency for high momentum particles to be preferentially aligned with the current and target directions.

ARIADNE gives the best description of the data in the lower two bins. In these two bins the number of tracks in the forward region appears to be overestimated by HERWIG and severely unserestimated by MEPS which also appears to underestimate the forward shift of the curent peak. MEPS also overestimates the currest peak in the second highest bin.

7.7.3 Observations

The MEPS distributions seen in figures 7.8 and 7.9 suggest that this model does not provide enough gluon radiation at low x, Q^2. This is indicated by the lack

of tracks and momentum in the forward direction, compared to the data, and by the underestimation of the forward shift of the current peak. For HERWIG, the change in momentum flow with Q^2 is greater than is seen in the data, the forward region being overestimated in the lowest bin, the current peak too pronounced in the highest, while the middle two bins describe the data well. ARIADNE appears give the best overall description of the data, particularly at low x.

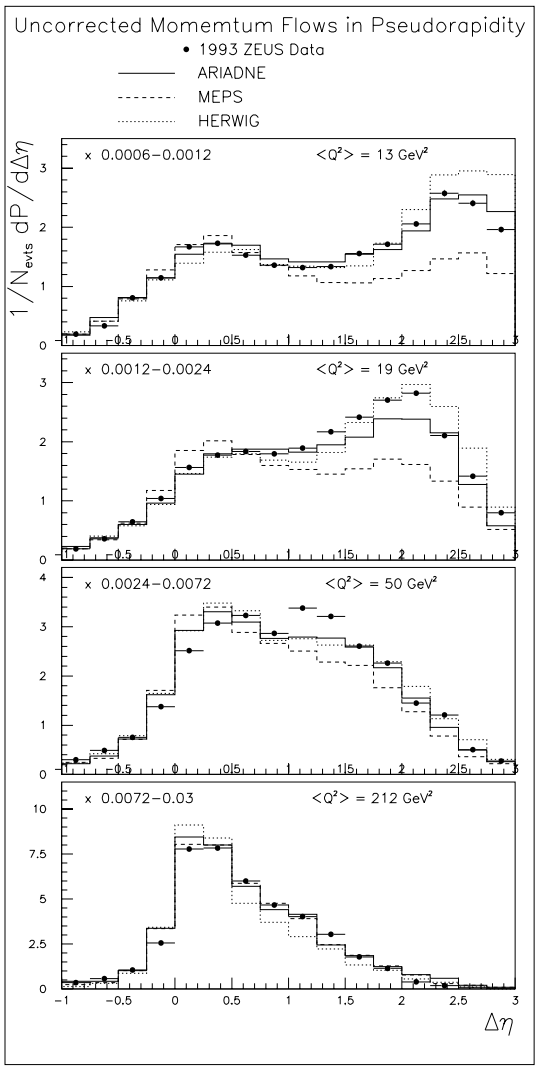

Figure 7.8: *Momentum flow versus $\Delta\eta$ showing 1993 ZEUS data and the Monte Carlo predictions of three theoretical models.*

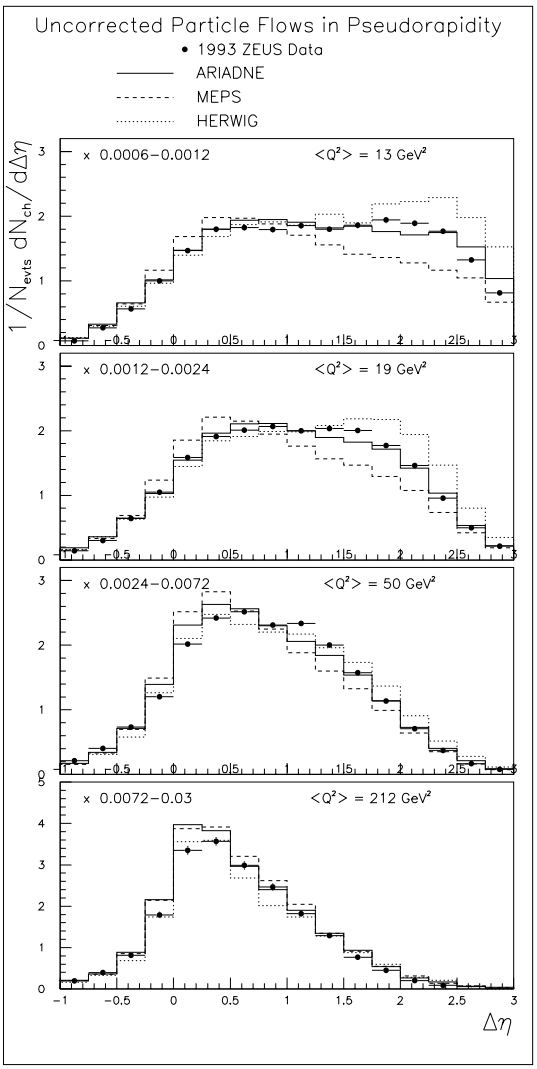

Figure 7.9: *Particle flow versus $\Delta\eta$, showing 1993 ZEUS data and the Monte Carlo predictions of three theoretical models.*

7.8 Correcting for Detector Effects

7.8.1 CTD Acceptance in $\Delta\eta$

The distributions of momentum and particle flow versus $\Delta\eta$ predicted by the ARIADNE simulation at the hadron level are compared, in figures 7.10 and 7.11, with the distributions obtained after passing the ARIADNE data through the full detector simulation.

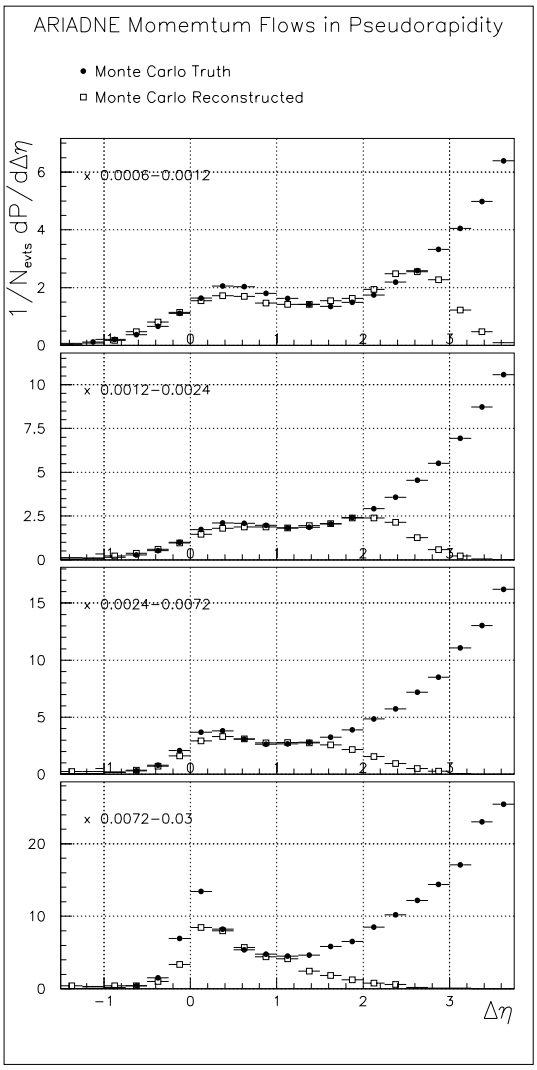

Figure 7.10: *True and reconstructed momentum flow versus $\Delta\eta$.*

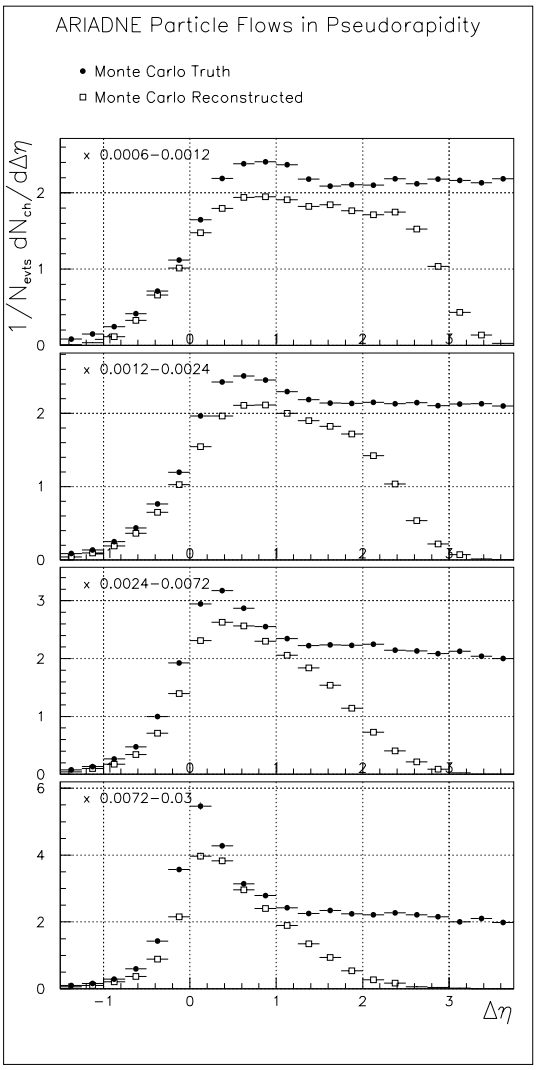

Figure 7.11: *True and reconstructed particle flow versus $\Delta\eta$.*

The forward acceptance limit is clearly evident here. At large positive values of $\Delta\eta$, most of the high-momentum particles associated with the remnant are

outside the tracking range. With increasing x, and inceasing η_h, the upper limit in $\Delta\eta$ of CTD acceptance decreases. While in the lowest bin a significant part of the remnant is observable in the CTD, moving upwards in x progressively more of it is lost, until, in the highest bin, only the current peak is visible.

In all but the highest bin, detector effects in the region of the current peak appear to be small.

In the highest bin there appears, in the region of $\Delta\eta = 0$, to be a significant loss of particles and a proportionately greater loss of momentum. Since the selection cuts on η_h should ensure that this region is well within the boundaries of CTD acceptance, the systematic loss of high momentum tracks here is not easily understood. It is best explained in terms of problems which occur at the pattern recognition stage of track reconstruction when there are three or more straight tracks close together, a topology associated with the well-colimated high P_T jets which are characteristic of this highest x-Q^2 bin.

As explained in chapter 3, the even-numbered "stereo" superlayers of the CTD give track segments with azimuthal offsets, from which, in the course of the track fit, the z position of the hits can be obtained. Three or more tracks close together can result in irresolvable ambiguities in the association of stereo segments with tracks. Wrong association of stereo segments can result in tracks being broken, or excluded from the vertex due to mismeasurement in z.

7.8.2 The Correction Factor Technique

Detector and reconstruction effects were taken into account by the bin-by-bin application of correction factors, $F_P(i)$ for momentum flow and $F_n(i)$ for particle flow.

The correction factors were obtained from Monte Carlo, using the ARIADNE sample which gave the best overall description of the data. The generated momentum and particle flows,

$$\frac{1}{N_{gen}}\frac{dP_{gen}}{d\Delta\eta_{gen}} \quad and \quad \frac{1}{N_{gen}}\frac{dn_{gen}}{d\Delta\eta_{gen}},$$

were compared with the observed momentum and particle flows,

$$\frac{1}{N_{obs}}\frac{dP_{obs}}{d\Delta\eta_{obs}} \quad and \quad \frac{1}{N_{obs}}\frac{dn_{obs}}{d\Delta\eta_{obs}},$$

N_{gen} being the number of *generated* events in a given analysis bin in *generated* x-Q^2,
N_{obs}, the number of *observed* events in the corresponding analysis bin in *reconstructed* x-Q^2,
P_{gen} and n_{gen}, the *generated* momentum and multiplicity,
P_{obs} and n_{obs}, the *reconstructed* momentum and multiplicity,
$\Delta\eta_{gen}$, the *generated* value of η_{track} minus the *generated* value of η_h, and
$\Delta\eta_{obs}$, the *reconstructed* value of η_{track} minus the *reconstructed* value of η_h.

Within each x-Q^2 bin, the two sets of correction factors $F_P(i)$ and $F_n(i)$ in bins i of $\Delta\eta$ were obtained by dividing the normalised *reconstructed* momentum (multiplicity) by the normalised *generated* momentum (multiplicity).

For each bin $\Delta\eta(i)$,

$$F_P(i) = \frac{N_{gen}}{N_{obs}} \frac{dP_{obs}}{dP_{gen}}(i), \tag{7.6}$$

$$F_n(i) = \frac{N_{gen}}{N_{obs}} \frac{dn_{obs}}{dn_{gen}}(i). \tag{7.7}$$

The correction factors defined by equations 7.6 and 7.7 account for the effects of detector acceptance, event reconstruction and selection, track reconstruction and selection, QED radiative effects, migration between x, Q^2 bins, migration between bins in $\Delta\eta$ and K^0 and Λ decay products assigned to the primary vertex.

For this correction factor technique to be valid, i.e to prevent the corrected data from being biased by the Monte Carlo model used to correct the data, $F_n(i)$ and $F_P(i)$ should be $\simeq 1$.

7.8.3 Correction Factors for 1993 ZEUS Data

Figures 7.12 and 7.13 show the correction factors obtained for the 1993 ZEUS data by the method described above. In the lowest bin the correction factors $F_P(i)$ are consistently $\simeq 1$ for $-1.0 < \Delta\eta < 2.5$, and $F_n(i)$ are consistently $\simeq 1$ for $-1.75 < \Delta\eta < 2.5$. For $\Delta\eta > 2.5$ the affect of the forward CTD acceptance limit is seen in the rising values of F_P and F_n.

Moving upwards in x, in the next bin the forward acceptance limit is seen at a lower value of $\Delta\eta$, as the a steep rise in the values of F_P and Fn commences at $\Delta\eta = 2.0$. Below this value the correction factors are consistently $\simeq 1$.

In the second highest bin the correction factors begin to rise in value at $\Delta\eta = 1.5$.

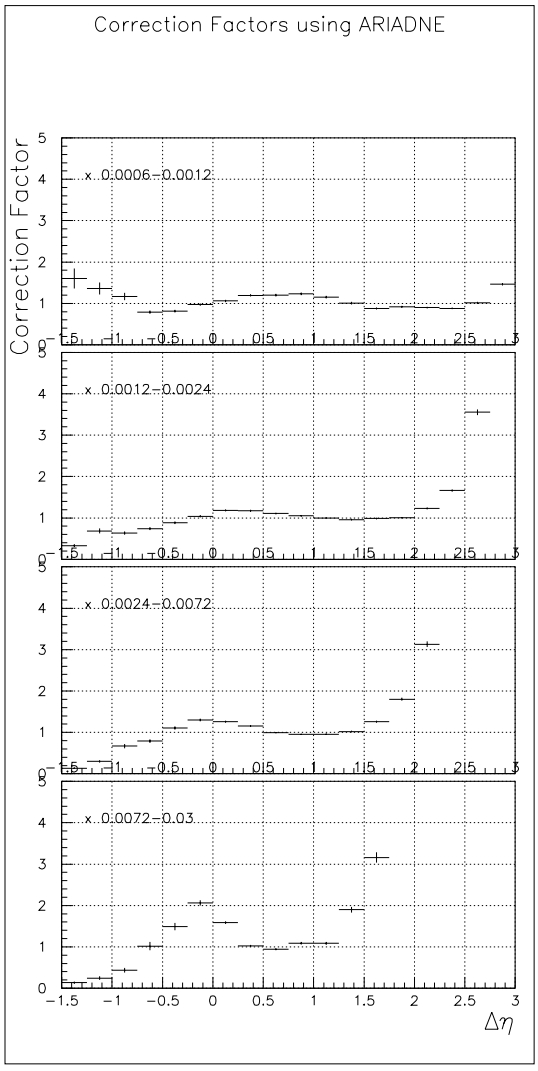

Figure 7.12: *Correction factors for momentum flow versus* $\Delta\eta$.

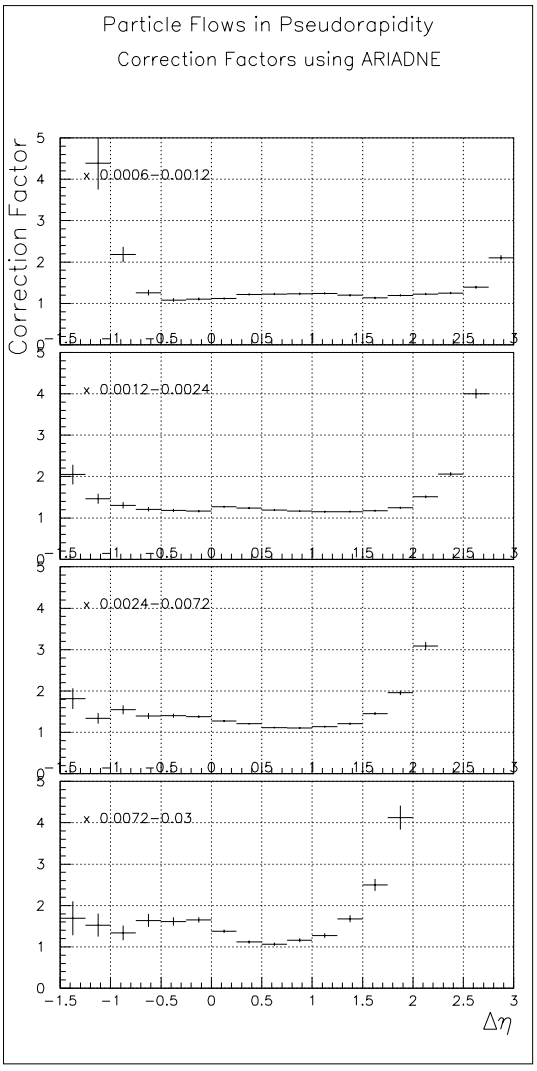

Figure 7.13: *Correction factors for particle flow versus* $\Delta\eta$.

In the highest bin the rise begins at $\Delta\eta = 1.0$, and the behaviour of the correction factors over the whole range, for F_P in particular, is somewhat erratic. At the peak at $\Delta\eta = 0$ where the track reconstruction problems outlined in section 7.8.1 come into play, the correction factor for the momentum flow is $\simeq 1.6$, while the correction factor for the preceding bin at $\Delta\eta = -0.25$, where both the generated and reconstructed distributions are rising steeply, is $\simeq 2$.

7.8.4 Corrected Results

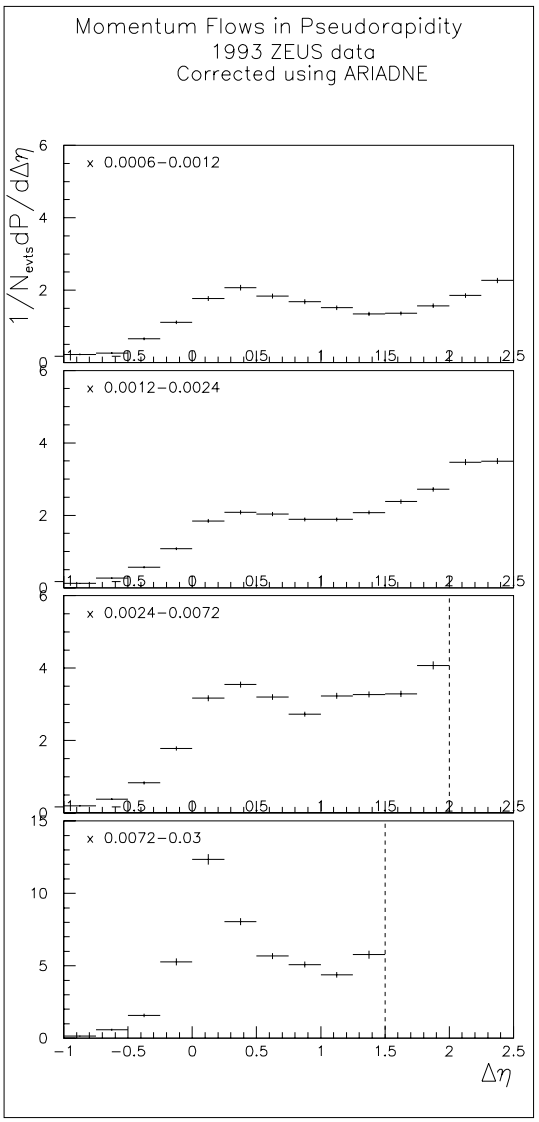

Figure 7.14: *Momentum flow versus $\Delta\eta$, corrected for detector acceptance.*

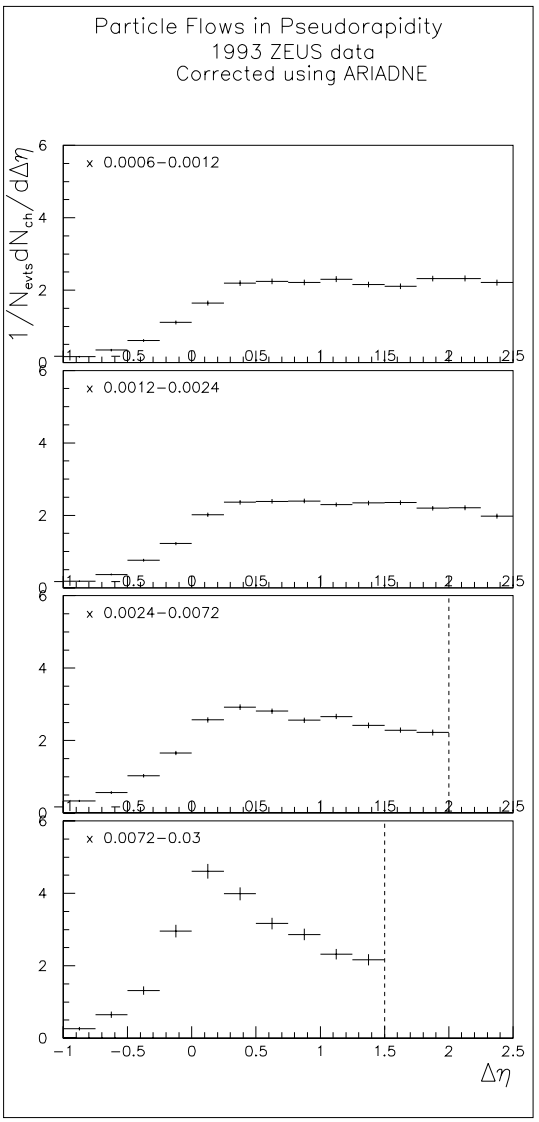

Figure 7.15: *Particle flow versus $\Delta\eta$, corrected for detector acceptance.*

Figures 7.14 and 7.15 show the momentum and particle flow distributions for the 1993 ZEUS data corrected for detector effects. In regions where the corrections factors were consistently greater than 2 (indicated by dotted lines in figures 7.14 and 7.15), results obtained from the correction factor technique would have been meaningless and therefore no attempt was made to correct the data.

7.9 Momentum Flows in Azimuth

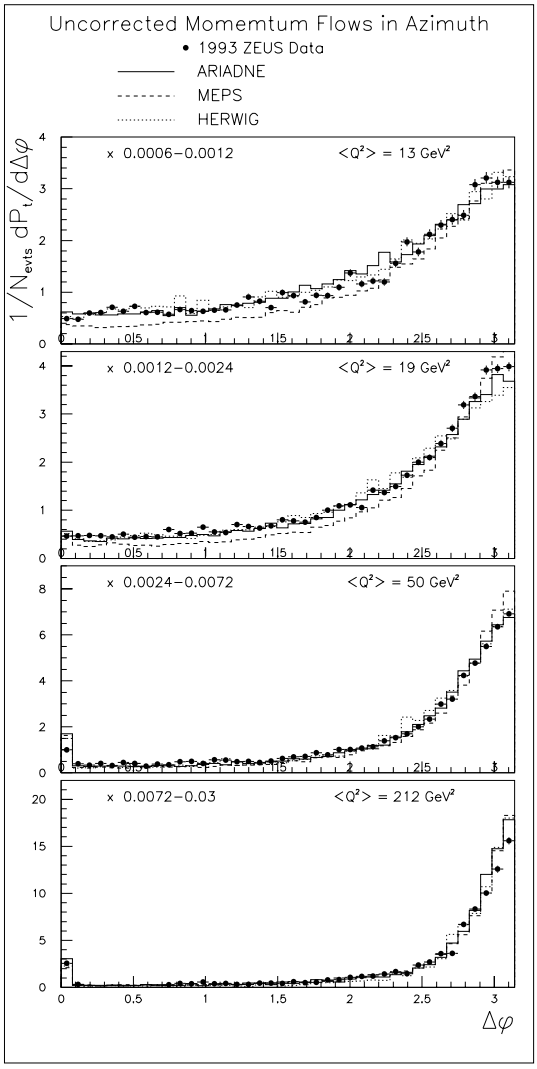

Figure 7.16: *Momentum flow versus $\Delta\phi$, (excluding matched electron tracks) showing 1993 ZEUS data and Monte Carlo predictions.*

In azimuth, the momentum flow with respect to $\Delta\phi$ (as defined in section 7.2.2) is expected to show a peak at $\Delta\phi = \pi$, since the vector sum of momenta of the current particles must balance in P_T with the scattered electron. Momentum associated with the remnant, having no constraints on azimuthal orientation, should form a flat pedestal to the distribution. Figure 7.16 shows the azimuthal momentum flow observed in the 1993 ZEUS data, compared, at the detector level, to the Monte Carlo predictions of ARIADNE, MEPS and HERWIG.
The data exhibits the expected peak at $\Delta\phi = \pi$, and in the two lowest bins, the pedestal associated with the remnant. In the higher x bins, as less of the remnant is seen in the CTD, the pedestal diminishes and the peak becomes more pronounced. The momentum flow in the peak increases, which is expected as the current has more energy at higher Q^2, and becomes more collimated, signifying that events with distinct jets are prevalent in this region. There are no significant differences between the ARIADNE and HERWIG distributions, and both describe the data well. For MEPS the underestimation of the forward region in $\Delta\eta$ shown in figure 7.8 corresponds in $\Delta\phi$ to an underestimation of flat region away from the peak.

7.10 Correlations between $\Delta\eta$ and $\Delta\phi$

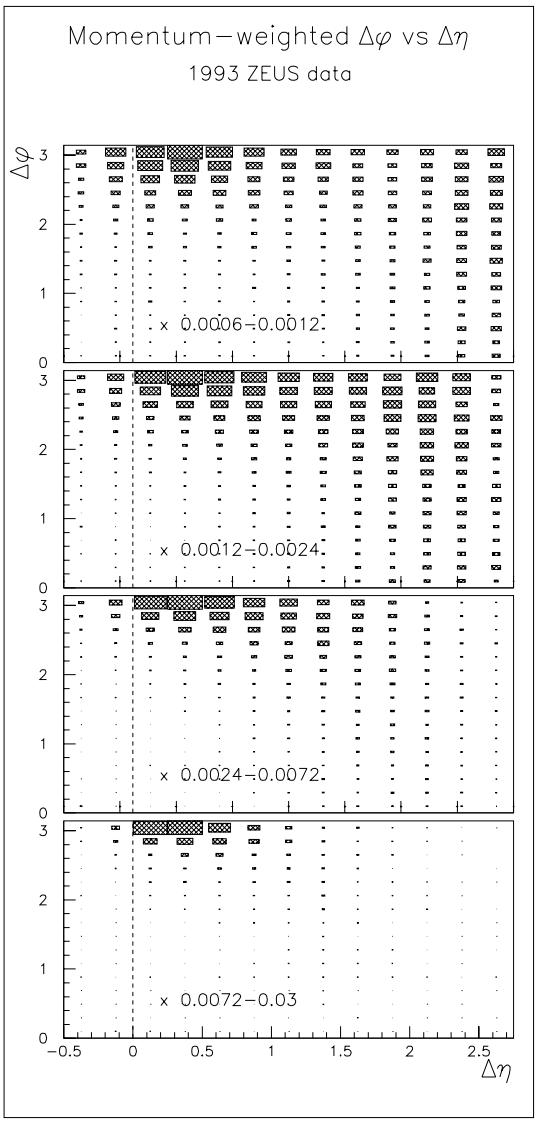

Figure 7.17: *Correlation between $\Delta\phi$ and $\Delta\eta$ in uncorrected ZEUS 1993 DIS data.*

Figure 7.17 shows the momentum flow in the $\Delta\phi$-$\Delta\eta$ plane, for 1993 ZEUS data which has not been corrected for detector effects. The most noticeable feature of these distributions is the correlation between $\Delta\eta$ and $\Delta\phi$ in the region of the current peak. Here, again, it is clear that the current peak is shifted forward from the QPM expectation of $\Delta\eta = 0$, but in azimuth occupies the expected region of $\Delta\phi = \pi$.

In the lower two bins of lower x, mometum flow associated with the remnant appears as a region of random azimuthal distribution at large $\Delta\eta$. For the higher x bins the remnant region is outside of the CTD acceptance.

It is interesting that a degree of correlation with $\Delta\phi = \pi$ extends forward well beyond the region of the current peak, and is discernable up to $\Delta\eta \approx 2$, which means that at two units of pseudorapidity forward from the nominal quark direction, the momentum flow is still affected in some way by the current.

This is perhaps the result of colour flow between the struck quark and the remnant, and of the forward pulling of the current peak, and is discussed further in the next chapter.

Chapter 8

The Breit Frame

8.1 A Choice of Frame

8.1.1 Limitations of the Laboratory Frame

In the previous chapter the hadronic final state of DIS events was analysed in terms of momentum flow in the HERA laboratory frame, using tracking data from the ZEUS CTD. It was observed that, even for classes of event for which little jet-like structure was expected, track momentum was concentrated in a cone in η-ϕ corresponding to the nominal direction of the struck quark, and in a forward peak at large η, flat in ϕ, as would be expected from particles originating from the target remnant. A " ridge" of momentum, azimuthally correlated with the struck quark, extended in η between the current and target peaks, evidence of QCD "string" interactions. At higher x, Q^2 the current peak became more pronounced, while the effects of QCD radiation appeared to be reduced.

Analysis in the laboratory frame of the evolution of QCD effects with x,Q^2 is compounded by the difficulty of disentangling these effects from those caused by the x,Q^2 dependence of HERA event kinematics. Moreover, HERA is the first ever DIS experiment conducted with colliding beams. There is no obvious precedent in deciding what is the most suitable frame, and different types of analysis may be suited to different frames.

8.1.2 Comparing DIS with Annihilation

In a study of the hadronic final state, the results available from other experiments in energy ranges comparable to that of HERA are those from e^+e^- colliders. Both annihilation and DIS can be used to study the action of the QCD forces which arise as quarks are pulled apart from one another at high energies, and to gain some insight into the dynamics of the underlying interactions through observation of the distribution of momentum among the final-state hadrons.

An important distinction between e^+e^- annihilation and DIS, when both types of experiment are viewed in terms of interactions between partons, is that in the latter case the particles are in contact both before and after the collision, so that the effect of initial-state QCD radiation becomes significant.

Comparing measurements of the hadronic final state from the two processes, their similarities and differences can be investigated. It is of interest to determine whether, in the colour field resulting from the splitting apart of proton constituents (quark and diquark in the quark-parton model), the hadronisation process operates in the same manner as it does in the colour field formed between a newly-created quark-antiquark pair.

Unlike HERA, e^+e^- experiments are well suited to analysis in the laboratory frame. They are symmetric. The outgoing particle and antiparticle form two distinct hemispheres and a well-defined "thrust" axis. For a given beam energy the value of $Q^2{=}s{=}W^2$ is fixed.

At HERA events are asymmetric, and there is not an obvious choice of axis. Both Q^2 and W^2 vary from event to event, as well as being different from each other. While this provides a valuable opportunity to measure evolution through a large range in Q^2 (or W^2) within a single experiment, it complicates analysis in the laboratory frame.

8.1.3 Why the Breit Frame?

Two frames widely-used in HERA physics analysis are the hadronic (γ^*-p) centre-of-mass frame and the Breit frame, both of which are aligned along the direction of the virtual photon.

Of the two, the hadronic centre-of-mass frame is perhaps intuitively easier to understand. The incoming proton and photon each have energy $W/2$, and, in the final state, the event is symmetric, each hemisphere having energy $W/2$. The disadvantage of the hadronic centre-of-mass frame is that, although the struck quark and remnant are back-to-back, the two event hemispheres bear no physical correspondence to the region associated with the struck quark and that associated with the remnant; the direction of the virtual photon is clearly defined but the direction of the QCD colour flow is not.

In the Breit, or "brick wall" frame, the struck quark rebounds from the virtual photon, totally reversing its momentum, while the course of the target remnant is unaltered. The final-state quark and the remnant therefore move apart in opposite directions, a configuration which, although appearing almost counter-intuitive, permits direct comparison with the laboratory-frame final state of annihilation experiments.

The Breit frame differs from the hadronic centre-of-mass frame by a longitudinal boost, so that the left-right symmetry is lost. More importantly the negative

hemisphere – the *current region*– is uniquely associated with the struck quark, the positive hemisphere – the *target region* – is associated with the remnant, and the colour "string" operates along the virtual photon axis.

8.1.4 Kinematics of the Breit Frame

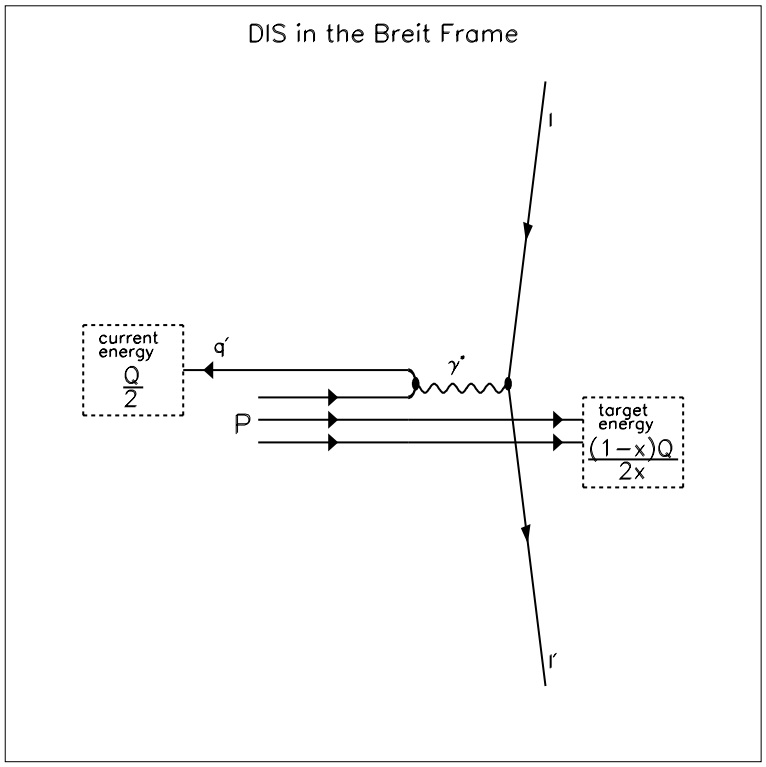

Figure 8.1: *Kinematics of DIS in the Breit frame, according to the quark-parton model.*

Breit frame kinematics are determined by the requirement that the momentum $p_q^{*\prime}$ of the outgoing quark must be equal in magnitude and opposite in direction to the momentum p_q^* of the incoming quark. For this the 4-momentum q^* of the virtual photon must be completely spacelike:

$$\begin{aligned} q^* &= (0,0,0,-Q) \\ p_q^* &= (Q/2,0,0,Q/2) \\ p_q^{*\prime} &= (Q/2,0,0,-Q/2) \end{aligned}$$

Since $p_q^* = xP^*$ (for the quark-parton model), the energy of the struck quark and remnant, $E_q^{*\prime}$ and $E_{remnant}^*$, are given by

$$E_q^{*\prime} = xP^* = \frac{Q}{2} \tag{8.1}$$

$$E_{remnant}^* = (1-x)P^* = \frac{(1-x)Q}{2x} \tag{8.2}$$

In the standard Breit frame configuration used for HERA analysis, the virtual photon is aligned with the Z axis, such that the struck quark travels in the negative z direction ($p_{z_q}^* = -Q/2$), the target remnant in the positive direction ($p_{z_{remnant}}^* = (1-x)Q/2x$). Thus the left hemisphere (current region) of the event is populated by the fragmentation products of the struck quark, while the right hemisphere (target region) is populated by fragmentation products of the target remnant.

For the electron, energy conservation requires that $E_e^{*\prime} = E_e^*$. The electron comes in from the target region, with $p_{z_e}^* = -Q/2$, and is scattered back into the target region with $p_{z_e}^* = +Q/2$.

The electron angle in the Breit Frame, θ_e^*, is given [53] by

$$cos\theta_e^* = \frac{Q}{2E_e^*} \simeq = \frac{y}{2-y} \tag{8.3}$$

For the kinematic region covered by this analysis, the average value of y is about 0.15, for which $\theta_e^* \simeq 85°$. The scattered electron angle is therefore almost perpendicular to the Z-axis, so that it is just inside the border of the target region.

8.2 From the Lab Frame to the Breit Frame

8.2.1 General Transformation to the Breit Frame

Calculating the Lorentz Boost Variables

The standard Lorentz boost, for a particle with energy E and three-momentum $\vec{p}$ in the laboratory frame, and with energy E^* and three-momentum $\vec{p}^*$ in the Breit frame, is

$$E^* = \gamma(E - \vec{\beta}.\vec{p}) \tag{8.4}$$
$$\vec{p}^* = \gamma(\vec{p} - \vec{\beta}E) \tag{8.5}$$

If the particle has mass M and is at rest in the Breit frame, γ and β can be expressed as

$$\vec{\beta} = \frac{\vec{p}}{E} \tag{8.6}$$
$$\gamma = \frac{1}{\sqrt{1 - |\vec{\beta}|^2}} = \frac{E}{M} \tag{8.7}$$

from which, the boost to the Breit frame of DIS events is given by

$$\vec{\beta} = \frac{\vec{q} + 2x\vec{P}}{q_0 + 2xP_0} \tag{8.8}$$
$$\gamma = \frac{q_0 + 2xP_0}{\sqrt{Q^2 + 4x^2m_P^2}} \tag{8.9}$$

where $q = (q_0, \vec{q})$ and $P = (P_0, \vec{P})$ are the laboratory-frame four-momenta of the virtual photon and incident proton respectively.

Alignment with Breit Frame Axes

The Lorentz boost is followed by rotations

1. through $\pi - \Theta^*$, to align the virtual photon with the negative Z axis, and
2. through $-\Phi^*$ to orient the plane of the incident and outgoing electron with the Breit X-Z plane, so that the electron is scattered at an angle of $\phi^* = \pi$,

where Θ^* and Φ^* are the polar and azimuthal angles made by the virtual photon with respect to the Breit Frame axes.

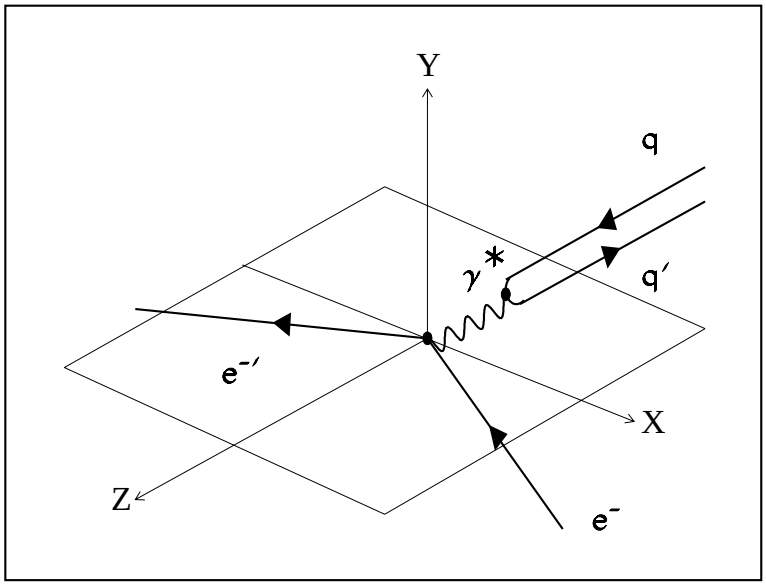

Figure 8.2: *Alignment of e^-, γ^* and q with the Breit frame axes.*

8.2.2 Transformation of ZEUS events to the Breit Frame

The method described above requires, both for the boost and the rotation, knowledge of the virtual photon four-momentum components. In this analysis these are determined from the reconstructed energy and momentum of the scattered electron.

For each event, the position of the electron, in the ZEUS system, is obtained from calorimeter measurement, and the polar and azimuthal angles are calculated with respect to the tracking vertex.

The electron energy, E'_e, is derived from the double-angle measurement of Q^2 (equation 6.11) described in chapter 6, section 6.2.4:

$$E'_e = \frac{Q^2_{DA}}{2E_e(1 + cos\theta_e)} \tag{8.10}$$

The use of this method, rather than direct calorimeter measurement of E'_e, reduces sensitivity to the absolute energy scale of the calorimeter.

Knowing E'_e, θ_e and ϕ_e, it is trivial to calculate the electron four-momentum and hence, from momentum conservation, the four-momentum of the virtual photon.

This allows β to be calculated using equation 8.8, after which the four-vector of each reconstructed track which has been assigned to the primary vertex is boosted to the Breit frame. The track four-vectors are obtained from the momentum, polar and azimuthal angle measurements fitted at the vertex, with the energy calculated on the assumption of pion mass.

8.2.3 Modified Breit Frame Kinematics

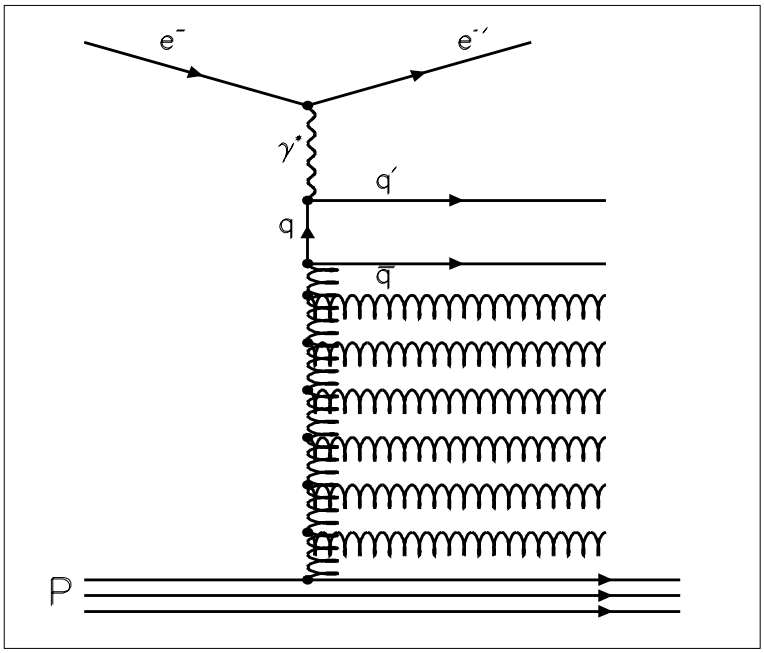

Figure 8.3: *Feynman diagram of DIS off a sea quark, accompanied by initial-state gluon radiation.*

In the kinematic region, $x < 0.03$, which is the subject of this study, the dominant process is that in which the virtual photon interacts with a sea quark, accompanied by initial-state gluon radiation. This is shown in figure 8.3. Since the sea quark is a constituent of a $q\bar{q}$ pair which is not massless, the quark-parton model kinematics are modified, and momentum associated with the struck quark is pulled towards the direction of the remnant.

The formulation of the Breit frame kinematics, described in section 8.1.4, is based on the quark-parton model. For a more complicated interaction involving a massive $q\bar{q}$ system and a "gluon ladder", the definition of the Breit frame is less clear-cut, since the two properties,

(a) that the struck quark is completely back-scattered, and

(b) that the virtual photon is completely spacelike,

no longer coincide.

In this analysis, the Breit frame kinematics are obtained from the virtual photon four-vector via measurement of the scattered electron, as described in section 8.2.2. Therefore the Breit frame is effectively defined by the second of the above two properties – that the virtual photon is completely spacelike.

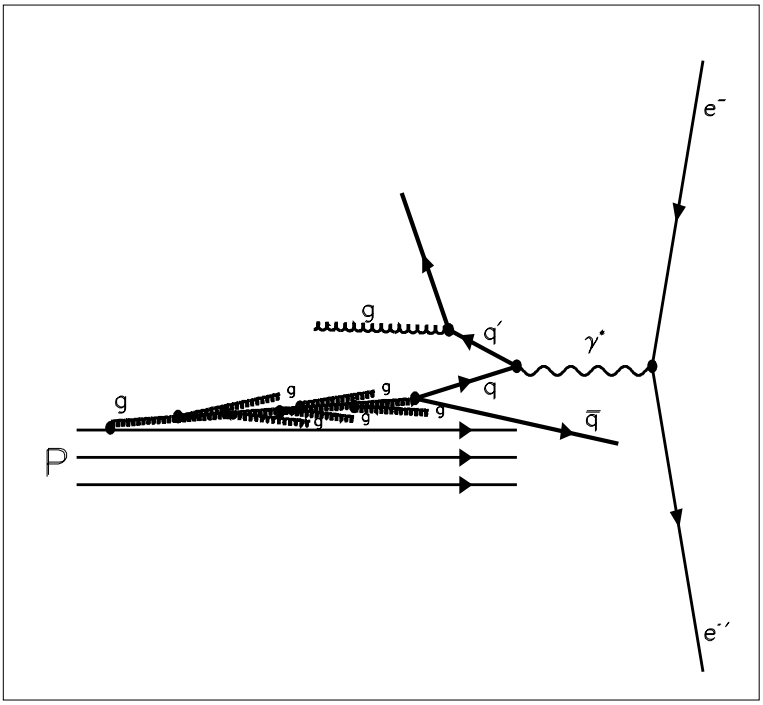

Figure 8.4: *Kinematics in the Breit frame for an electron scattered off a sea-quark, connected to the proton by a cascade of initial-state gluon radiation. The collinearity of the quark-parton model is lost.*

In what may be viewed as a boson-gluon fusion process, the t-channel gluon, which is essentially collinear with the incoming proton, evolves into a quark-antiquark pair (figure 8.4).

One constituent of the $q\bar{q}$ system interacts with a virtual photon, with four-momentum $(0, 0, 0, -Q)$, and is scattered.

If Q is large compared with the invariant mass of the $q\bar{q}$ system, and the interacting quark is on-shell, the kinematics resemble those of the quark-parton model, the quark coming in with $E_q^* \approx p_{z_q}^* \approx Q/2$ and being back-scattered with $E_q^{*\prime} \approx Q/2$, $p_{z_q}^{*\prime} \approx -Q/2$.

If the $q\bar{q}$ system has invariant mass of the same order as Q, collinearity in the Breit frame is lost and p_T becomes significant.

If the virtuality of the quark were unchanged by the scattering, it would come in with $p_{z_q}^*$ of $+Q/2$ and be scattered with $p_{z_q}^{*\prime}$ of $-Q/2$. Since there would also be a non-p_z component, the struck quark would have energy $E_q^{*\prime} > Q/2$ and be rotated with respect to the nominal current direction (the negative Z-axis).

However, to allow p_T in the $q\bar{q}$ system, the internal quark line must have spacelike virtuality, i.e. an invariant mass $m^2 = \hat{t} < 0$, given by

$$\hat{t} = (q^* - p_q^{*\prime})^2, \tag{8.11}$$

where q^* and $p_q^{*\prime}$ are the four momenta of the virtual photon and struck quark respectively.

In terms of energy, p_z and p_T,

$$\hat{t} = (-E_q^{*\prime}, -p_{T_q}^{*\prime}, (-Q - p_{z_q}^{*\prime}))^2 \tag{8.12}$$

so, assuming the outgoing quark to be on-shell,

$$\hat{t} = -Q(2p_{z_q}^{*\prime} + Q) < 0 \; . \tag{8.13}$$

Rearranging,

$$p_{z_q}^{*\prime} = -\frac{Q}{2} - \frac{\hat{t}}{2Q} > -\frac{Q}{2} \; . \tag{8.14}$$

When $\hat{t}$ is non-zero the internal quark line is off-shell, so four-momentum conservation no longer specifies that it has energy $Q/2$, or that it is completely back-scattered in p_z. The longitudinal momentum of the outgoing quark is shifted forward with respect to the QPM expectation, so that it is pulled towards the target.

An alternative argument [49] is sometimes presented in terms of the $q\bar{q}$ mass squared, $\hat{s}$. However, considering $\hat{t}$ focusses more clearly on the quark struck by the photon, and dispells any ambiguities caused by considering its partner antiquark to be associated with the target, rather than current, fragmentation region.

8.3 Mapping $\Delta\eta$-$\Delta\phi$ to the Breit Frame

It is informative to see how the "current" and "target" peaks observed in the laboratory-frame momentum flow correspond to the Breit-frame current and target regions, and how the laboratory $\Delta\eta$-$\Delta\phi$ plane transforms to the Breit Frame.

8.3.1 Redefinition of $\Delta\phi$

The definition of $\Delta\phi$ used in this chapter is somewhat different to that employed previously. In chapter 7, $\Delta\phi$ was defined, according to equation 7.4, as the absolute value of the difference in ϕ between any given track and the scattered electron, so that $\Delta\phi$ ran from 0 to π, and the struck quark had a nominal value of $\Delta\phi = \pi$.

Here, $\Delta\phi$ (as shown in figures 8.6 and 8.7) is redefined as the azimuthal angle of a given track measured with respect to the nominal azimuthal direction of the struck quark (which is opposite in azimuth to the measured value of the scattered electron). Now, $\Delta\phi$ runs from $-\pi$ to π, and the struck quark has a nominal value of $\Delta\phi = 0$, and is therefore centred at (0,0) in $\Delta\eta$-$\Delta\phi$ space.

8.3.2 Mapping $\Delta\eta$-$\Delta\phi$ to η^*

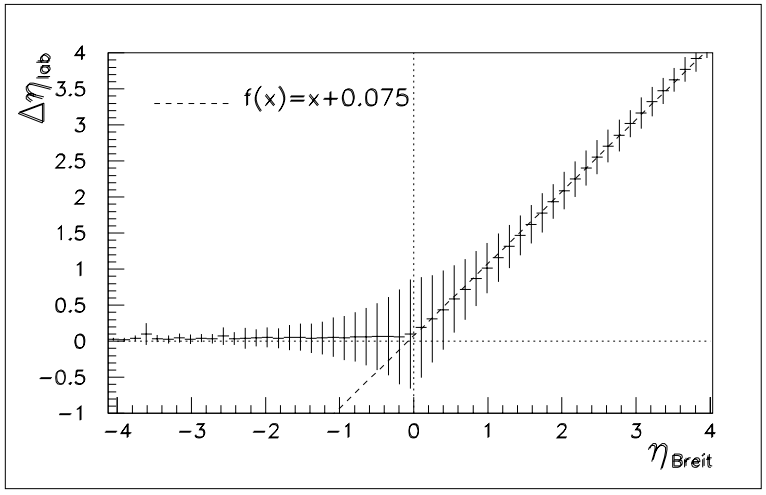

Figure 8.5: *Laboratory frame $\Delta\eta$ versus Breit frame η^* for four-vectors generated by ARIADNE and boosted by the procedures described in section 8.2. The error bars show the spread of the distribution.*

In the Breit frame neither tracks associated with the struck quark nor those with the target remnant have any preferred azimuthal orientation. In the Breit current region, the laboratory quantities $\Delta\eta$ and $\Delta\phi$ become folded together. Progressively smaller values of $r = \sqrt{\Delta\eta^2 + \Delta\phi^2}$ correspond to progressively more

negative values of η^* in the Breit frame, and (0,0) in the $\Delta\eta$-$\Delta\phi$ plane ($r = 0$) maps to $\eta^* = -\infty$.

Tracks associated with the remnant are expected to have an effectively random azimuthal distribution in both the laboratory and Breit frames. As the remnant is aligned with the positive Z-axis in both frames, the boost for tracks assigned to the Breit target region is mainly longitudinal. For tracks at large positive η, the laboratory frame value of $\Delta\eta$ corresponds quite closely to the Breit frame η^*, as is seen in figure 8.5.

8.3.3 Current-Target Demarcation in $\Delta\eta$-$\Delta\phi$ Space

Figure 8.6 shows the momentum flow in the laboratory $\Delta\eta$-$\Delta\phi$ plane , for tracks which, when boosted to the Breit frame, are assigned to the current region, and, separately, for tracks assigned to the Breit target region.

The Breit current and target regions map to two distinct regions of $\Delta\eta$-$\Delta\phi$ space. The boundary between the Breit current and target regions ($\eta^* = 0$) maps to an ellipse on the $\Delta\eta$-$\Delta\phi$ plane, with one focus at (0,0). The Breit current region corresponds to the area inside the ellipse, the target region to the area outside it.

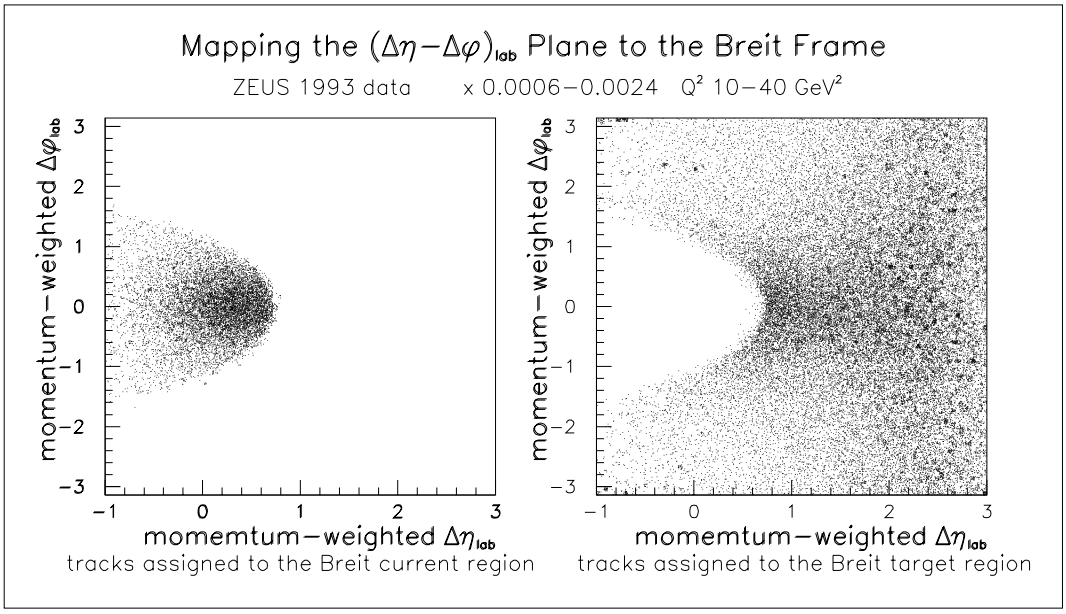

Figure 8.6: *Momentum flow in laboratory frame $\Delta\eta$-$\Delta\phi$ space,* left *for tracks which, if boosted to the Breit frame, are assigned to the current region, and* right *for tracks which are assigned, in the Breit frame, to the target region.*

Migration from the Current to the Target Region

It is most noticeable in figure 8.6 that the momentum peak associated with the struck quark is not centered at (0,0), and appears to overlap into the target region. This is due to the forward shift in $\Delta\eta$ which was observed in chapter 7.

As discussed there, and in section 8.2.3 above, DIS events at low x are dominated by sea-quark and gluon interactions. If the invariant mass squared of the $q\bar{q}$ system is comparable in magnitude to Q^2 the struck quark is pulled towards the remnant. This results in some of the final-state hadrons resulting from fragmentation of the struck quark being assigned to the target – rather than current – region in the Breit frame.

Migration of tracks between the current and target regions can, in addition, be caused by reconstruction errors – either by mismeasurement of the track θ in the laboratory frame or by errors in the reconstruction of the event kinematics leading to wrong construction of the Breit frame axes. It has been observed [54] that migration from the current to the target exceeds migration from the target to the current, and is greatest in the lowest x-Q^2 bins, where it can be as much as 25%

It should be noted that whereas migration due to reconstruction errors can be corrected using Monte Carlo techniques (section 7.8.2), migration due to the effects of quark masses cannot.

Correlations in $\Delta\phi$ in the Target Region

Since the fragmentation products of the remnant are expected to be randomly distributed in $\Delta\phi$, any correlation seen in target-region tracks with $\Delta\phi = 0$ can be a sign either that fragmentation products of the struck quark have migrated to the target region, or that some of the tracks associated with the remnant have been pulled towards the direction of the current, due to the effects of the colour flow between the struck quark and the remnant.

In the case of a BGF interaction, any such colour flow observed in the CTD would be between the backward-going struck quark and its forward-going partner. Particles associated with the initial-state gluon cascade tend to be colinear with the proton direction, and therefore typically have large positive $\Delta\eta$. While some of these particles produce tracks, usually of high momentum, in the forward region of the CTD, most of the gluon fragmentation region is outside the CTD acceptance.

In figure 8.6, the azimuthal distribution of tracks assigned to the target region shows a concentration at $\Delta\phi = 0$. This is most pronounced at low $\Delta\eta$, where the most obvious cause is migration from the current region. However a degree of correlation persists up to and even slightly beyond $\Delta\eta = 2$, evidence of colour flow.

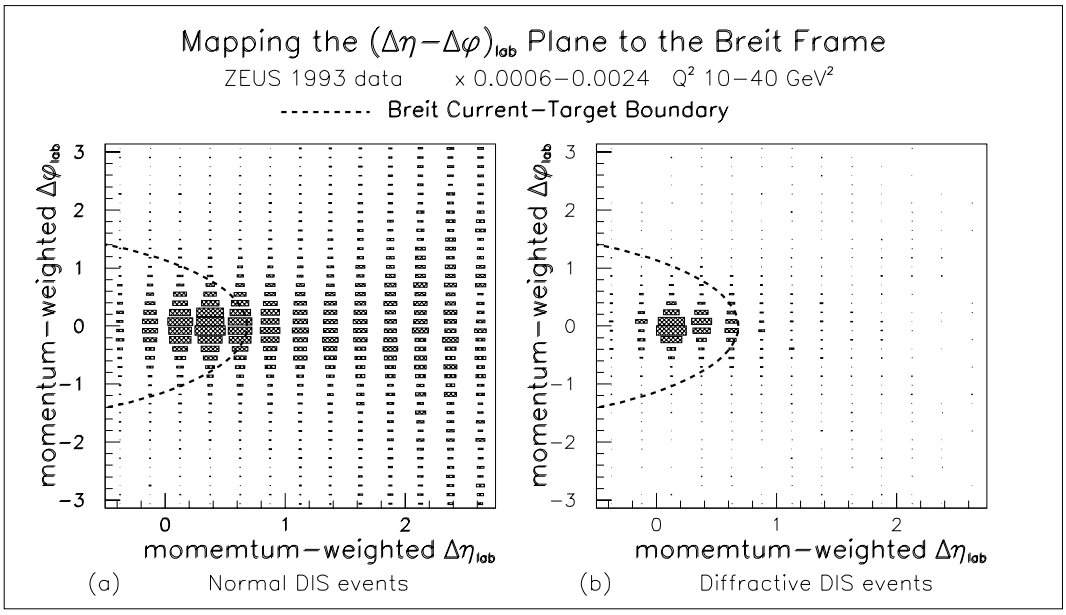

Figure 8.7: *Momentum flow in the $\Delta\eta$-$\Delta\phi$ plane, comparing* (a) *normal DIS events with* (b) *diffractive DIS events. The dotted lines show the Breit frame current-target boundary mapped to laboratory frame $\Delta\eta$-$\Delta\phi$ space.*

8.3.4 Comparing Diffractive and Non-Diffractive Events

Diffractive DIS events, in this analysis identified on the basis of "rapidity gap" criteria (chapter 7, section 7.6), are believed to involve exchange of a pomeron, which, being colourless, does not give rise to an initial-state parton cascade. The resulting $q\bar{q}$ which interacts with the virtual photon has far less virtuality than one belonging to a gluonic interchange. As a result the struck quark kinematics at the γ^*-q vertex can be expected to show far less deviation from the quark-parton model than is the case for normal DIS events.

In figure 8.7 the momentum flow in the $\Delta\eta$-$\Delta\phi$ plane for diffractive events is compared with that for normal DIS events, for events with x ranging from 0.0006 to 0.0024.

The difference is striking. For diffractive events, the greatest concentration of momentum is contained within the section of $\Delta\eta$-$\Delta\phi$ space which corresponds to the Breit current region, and the current peak is much closer to (0,0) than is the case for normal DIS events. Momentum assigned to the Breit target region is spread diffusely over the $\Delta\eta$-$\Delta\phi$ plane.

These events thus show very little evidence of colour flow or initial-state QCD radiation, which is consistent with the hypothesis that they are caused by the exchange of a colourless object (pomeron) in the t-channel.

8.4 The Effect of the Boost on Energy Scale

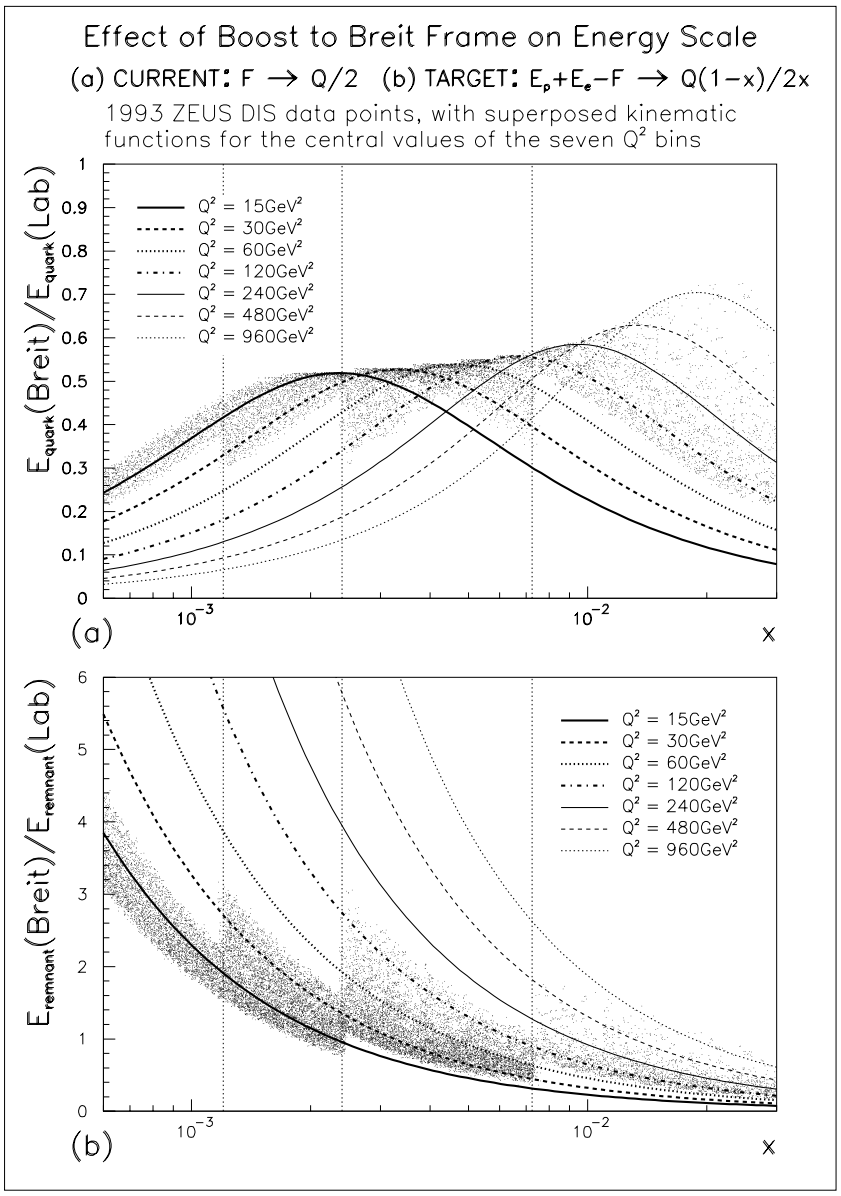

Figure 8.8: *Energy transformation of (a) the struck quark and (b) the remnant from the laboratory frame to the Breit frame. The data points show the* event *kinematics of the selected 1993 DIS sample.*

Figure 8.8 shows how the energies of the current and target, obtainable from x, Q^2 and the incoming beam energies, transform to the Breit frame. The factor by which they change is plotted, as a function of x, for the central value of each of the Q^2 bins used in this analysis. The data points are the E_{Breit}/E_{lab} scaling factors corresponding to the x, Q^2 values of the events selected for this analysis.

In the laboratory frame the current has energy F and the target therefore has

energy $E_P + E_e - F$. In the Breit frame the current has energy $Q/2$ and the target, energy $Q(1-x)/2x$. In the x, Q^2 range under consideration here, F is larger than $Q/2$; the current energy is reduced by the transformation to the Breit frame, typically by about a factor of two. The target, by contrast, can be highly energetic in the Breit frame, depending on x. In the lowest x bin the target can have a Breit-frame target energy of more than four times its laboratory-frame value. Thus, except perhaps in the highest x bin, the energy of the current transforms very differently to that of the target. This introduces a strong η^* dependence to the energy transformation of individual particles.

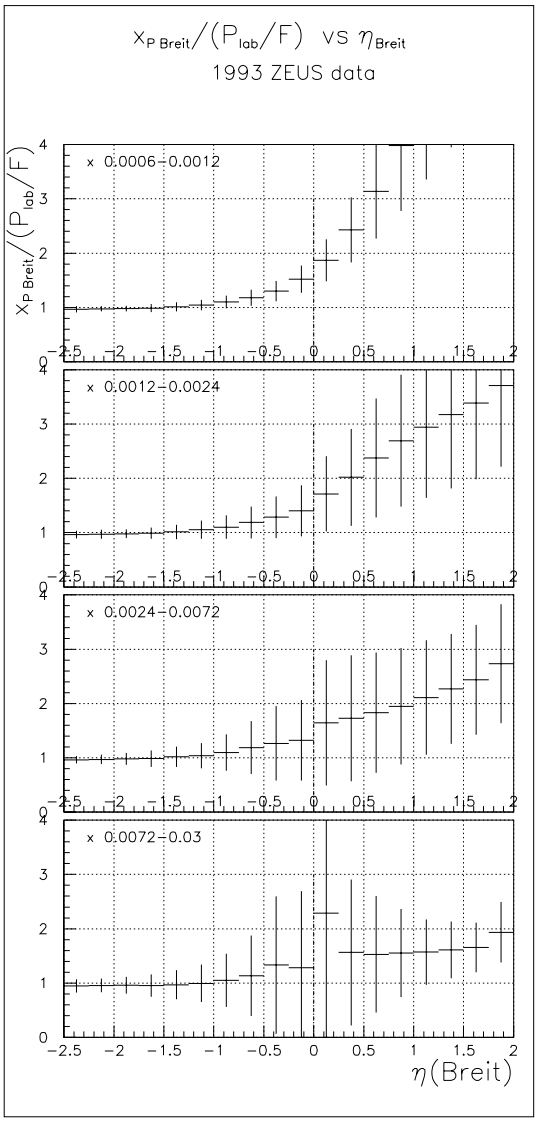

Figure 8.9: *Ratio of the Breit-frame to laboratory-frame fractional momenta versus η^*.*

The energy of a final-state hadron which is closely aligned with the current direction (large negative η^*) transforms similarly to that of the struck quark, while the energy of a hadron following the proton direction (large positive η^*) transforms in the same manner as that of the remnant. In between, for hadrons which are less closely aligned with either current or target, the ratio of Breit to laboratory-frame energy increases rapidly with η^*.

Figure 8.9 compares the Breit-frame quantity $x_P = 2P_{Breit}/Q$ (see section 8.6) – which is the track momentum expressed as a fraction of the total momentum of the current – with the corresponding laboratory-frame quantity, P_{lab}/F, and shows how the ratio between the Breit-frame and laboratory-frame values varies with η^*. If a given particle transforms in the same way as the struck quark, its fractional momentum should be the same in both frames. For tracks with $\eta^* < -1$ this appears to be the case, the Breit-frame to laboratory-frame ratio being consistently close to unity. Further forward, the η^* dependence is very apparent, particularly for low x where the difference between the current and target energies is greatest.

8.5 Momentum Flow versus η in the Breit Frame

8.5.1 Where is the Current Peak?

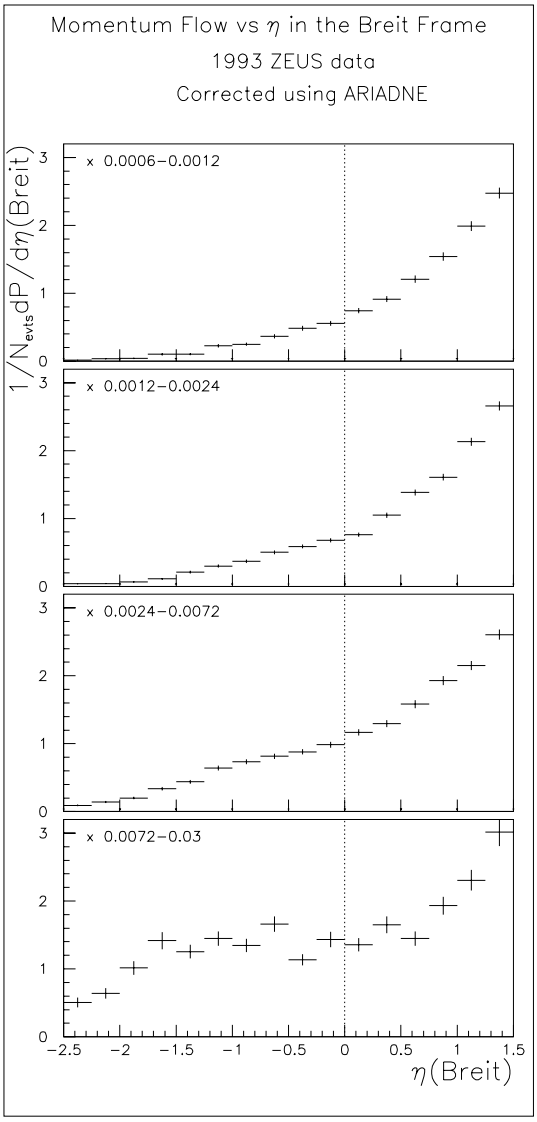

Figure 8.10: *Momentum flow versus η in the Breit frame, corrected for detector effects using ARIADNE.*

Figure 8.10 shows the Breit-frame momentum flow versus η^*, in the usual four x bins. The boundary between the current and target regions ($\eta^* = 0$) is indicated by a vertical dotted line.
Qualitatively these distributions look very different from the corresponding laboratory frame ones in figure 7.14 of chapter 7, section 7.8.4. Whereas in the laboratory frame there are distinct peaks associated with the current and target, in the Breit frame this structure is absent, except perhaps for the highest x bin. For the three lower x bins the only obvious characteristic is that of increasing momentum at higher values of η^*.
It may at first seem strange, even ironic, that, in the very frame which has been selected for its property of isolating the fragmentation region of the struck quark, the momentum flow should show neither a current peak nor any obvious demarcation of the region in between the current and the target. The fact that the current peak appears to be "washed out" in the Breit frame, while it is clearly visible in the laboratory frame even at low x-Q^2, can be understood as the result of several contributing factors, as discussed below.

8.5.2 Effects of the Transformation on Momentum Flow

In the laboratory frame, the current is restricted to a finite region of pseudorapidity, centered (for the QPM) at $\Delta\eta = 0$. The corresponding Breit frame region is infinitely large, so that the tracks following the nominal struck quark direction are spread out at large negative values of η^*, making the current peak less

pronounced.

As discussed in the previous section, at low x the energy difference between the struck quark and target remnant is far greater in the Breit frame than in the laboratory frame. In the laboratory frame the dip in momentum flow which separates the current and target peaks is in the region of $\Delta\eta \approx 1.5$. This corresponds in the Breit frame (figure 8.5) to a similar value of η^*. Here, due to the comparatively higher energy of the target, the transformation to the Breit frame scales up the momentum by a factor which increases progressively with η^*, and this "undoes" the effect of the dip seen in the laboratory frame in this region.

So whereas the laboratory frame kinematics tend to accentuate the current and target peaks and the division between them, in the Breit frame these characteristics become far less pronounced.

8.5.3 Effects of QCD Radiation on Momentum Flow

In the Breit frame, the QPM configuration should nonetheless give distinct current and target hemispheres, less pronounced than in in the laboratory frame but with some depletion of momentum flow in the boundary region between the current and target in the region of $\eta^* = 0$. In the highest x bin, where the typical event topology is closest to that of the quark-parton model, there is evidence of these characteristics.

In the lower x bins, the effect of initial state QCD radiation is to fill in any remaining dip. In the laboratory frame the current peak is shifted forward from $\Delta\eta = 0$, towards the region which corresponds, in the Breit frame, to the current-target boundary at $\eta^* = 0$ (figure 8.7). So the boundary region is populated at low x-Q^2 by particles associated with the forward-shifted current and also by soft gluon emissions.

At low x-Q^2 the momentum flows of the current and target regions appear to completely merge; the dominant feature of the overall momentum flow is the large difference in energy between the current and target.

8.6 From Quark to Hadrons

8.6.1 Fragmentation

In the previous chapter and in the previous sections of this chapter the hadronic final state has been discussed in terms of event topology and momentum flow. However, with a tracking detector it is also possible to describe the final state explicitly in terms of particles, and to determine how the final-state energy is distributed among its constituent charged hadrons. This is hoped to provide some insight into the underlying sequence of processes by which a parton evolves into a colourless hadronic system. The totality of these known and unknown processes, from perturbative gluon branching to non-perturbative hadronisation, is termed *fragmentation.*

8.6.2 Characteristics of the Fragmentation Function

In this context, a scaled momentum variable commonly used in e^+e^- annihilation experiments [55],[56],[57] is $x_P = 2P/\sqrt{s}$, where P is the momentum of a given charged hadron. For the simple QPM case an $e^+e^- \rightarrow q\,\bar{q}$ event consists of two outgoing quarks back-to-back, each with energy $\sqrt{s}/2$, so that x_P may be regarded as the fraction of the original quark's momentum taken by a hadron, i.e. $x_P \approx P_{hadron}/P_{quark}$. The distribution

$$D(x_P) = \frac{1}{N_{evts}} \frac{dn_{ch}}{dx_P} \tag{8.15}$$

is known as the *charged fragmentation function.* This distribution has a peak at low x_P, falling steeply as x_P increases. The depletion of particles at high x_P indicates that, in the development of a cascade and in the hadronisation process, the initial parton energy is shared among many softer particles. Through an iterative process of branching and showering, the energy remaining for the production of further particles is successively reduced. At some point the remaining energy becomes sufficiently close to the hadron rest mass, m_0, for further subdivision to be curtailed. This puts a limit on the multiplicity, which is the integral of $D(x_P)$, and also results in a depletion of particles with very low x_P.

The position and height of the peak are therefore dependent on the available energy ($\sqrt{s}/2$ in the e^+e^- case). This energy dependence is partly a consequence of the simple phase space considerations discussed above. What is of interest, however, is that it is also expected to show a sensitivity to QCD coherence effects [58].

At higher values of x_P, away from the peak, $D(x_P)$ scales, i.e., the distribution is independent of the value of P_{quark}.

8.6.3 Fragmentation Variables in DIS Breit System

As discussed in section 8.1.2, the kinematics of DIS are far more complicated than those of e^+e^- annihilation. The quantity P_{hadron}/P_{quark} is frame-dependent, and while the obvious energy scale for e^+e^-, set by the nominal value of P_{quark}, is $\sqrt{s}/2$, the appropriate energy scale for DIS is open to question. In the laboratory frame it is F, for the hadronic CMS, $W/2$, and for the Breit frame $Q/2$.

In section 8.1.3 it is argued that the most appropriate choice is the Breit frame, in which the negative hemisphere is identified with the fragmentation region of the QPM struck quark, and can be said to correspond to one hemisphere of the e^+e^- system.

In the Breit frame the nominal energy of the struck quark is $Q/2$, so that the scaled momentum variable is $x_P = 2P/Q$, where, as before, P is the hadron momentum. Where, for e^+e^-, the fragmentation function evolves with $\sqrt{s}$, in the DIS Breit system it is expected to evolve in a similar manner with Q. Figure 8.11 shows the $D(x_P)$ distributions, obtained from ZEUS DIS data, for the seven Q^2 bins (section 8.7.1) used in this analysis. The position and height of the peak show a clear Q^2 dependence, and the scaling at high x_P is also evident.

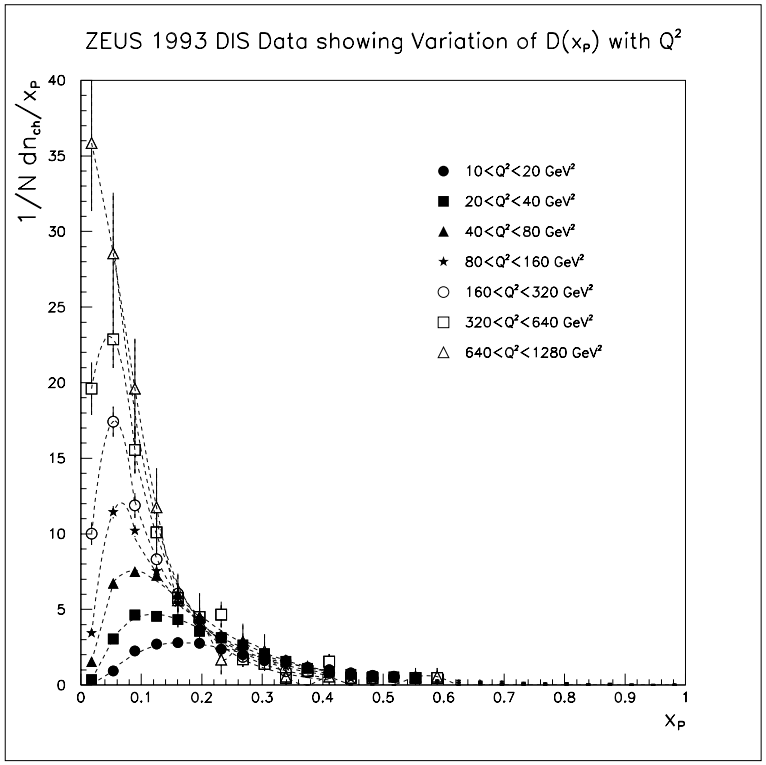

Figure 8.11: *Distributions of $D(x_P)$ in seven Q^2 bins. The dashed lines are arbitrarily fitted curves to guide the eye.*

8.7 How Fragmentation Depends on Q

8.7.1 Data Selection and Binning

In this analysis of fragmentation, the same dataset has been used as for the preceding analysis of momentum flow, selected according to the procedures outlined in chapter 6, section 6.3. However, the binning, described in chapter 7, section 7.4.3 has been slightly modified in order to accentuate the evolution with Q.

The individual x-Q^2 bins are unchanged, but whereas, previously, bins with different Q^2 but with a common x range were combined to form larger x bins, in this analysis bins with different x ranges but a common Q^2 range are grouped together.

This gives seven bins in Q^2, tabulated below.

Q^2 (GeV^2)	x
10 – 20	0.0006 – 0.0024
20 – 40	0.0012 – 0.0072
40 – 80	0.0024 – 0.0072
80 – 160	0.0024 – 0.03
160 – 320	0.0072 – 0.03
320 – 640	0.0072 – 0.03
640 – 1280	0.0072 – 0.03

Table 8.1: *Analysis bins in Q^2, integrated over selected ranges in x, used for the study of fragmentation.*

8.7.2 The Hump-Backed Plateau

The fragmentation function can also be expressed in the form

$$D(ln(1/x_P)) = \frac{1}{N_{evts}} \frac{dn_{ch}}{d\ ln(1/x_P)}. \tag{8.16}$$

Taking the logarithm of x_P expands the sensitive low x_P region around the peak; the logarithm of the reciprocal gives a quantity which is conveniently positive. The resulting distribution has a characteristic gaussian shape, often referred to as the "hump-backed plateau".

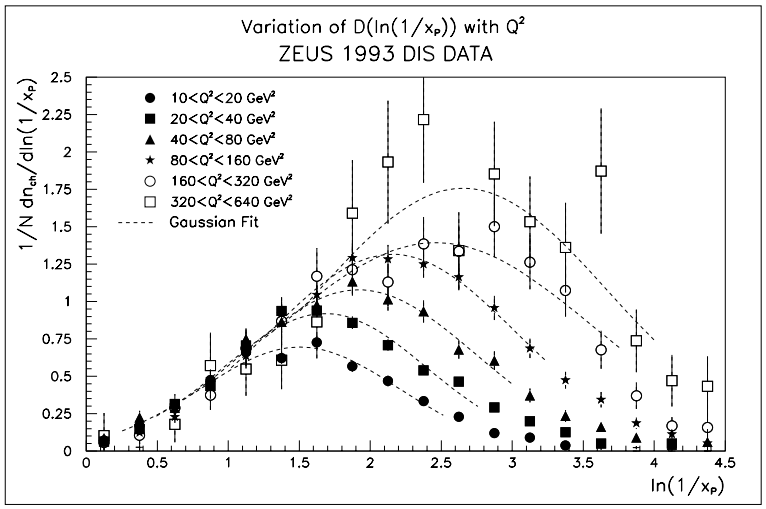

Figure 8.12: *Distributions of* $D(ln(1/x_p))$ *in six* Q^2 *bins.*

8.7.3 Kinematic Considerations

On purely kinematic grounds, the position of the peak should move upwards in $ln(1/x_P)$ as Q increases, since at larger Q there is more phase space for the production of hadrons with low x_P. For the same reason, the multiplicity is expected to increase with Q. The charged multiplicity is the integral of $D(ln(1/x_P))$, so the overall size of the distribution should increase as the peak, $ln(1/x_P)_{max}$, shifts towards higher values. This is seen in figure 8.12.

The effect of the hadron rest mass should begin to be significant at some $x_P \propto m_0/Q$, *i.e.*, at $ln(1/x_P) \sim ln\,Q$. Thus if kinematics were the only consideration, the position of $ln(1/x_P)_{max}$, as a function of $ln\,Q$, would be a straight line with a gradient of unity.

8.7.4 Incorporating QCD Coherence Effects

Coherence arises as a consequence of the quantum mechanical treatment of the cascade. As long wavelength gluons are unable to resolve individual colour charges of partons, the available phase space for soft gluon emissions is reduced to an angular-ordered region, due to destructive interference. Thus, coherence gives an additional constraint on the production of soft particles to that imposed by kinematics.

This causes $D(ln(1/x_P))$ to fall off more steeply at high $ln(1/x_P)$ so that the position of $ln(1/x_P)_{max}$ is shifted to a lower value. In this connection explicit predictions are made by the Modified Leading Log Approximation (MLLA) [59], assuming local hadron-parton duality [60].

Compared to the case where coherence is not assumed, the rate of growth of multiplicity with increasing Q is reduced, as is the gradient of $ln(1/x_P)_{max}$ versus $ln\,Q$.

8.7.5 Effects of Initial State Radiation

As has been discussed earlier in this chapter, the Breit frame kinematics, in their standard form, assume the QPM configuration. When higher order QCD effects are present, the struck quark is not back-to-back with the remnant but is shifted forwards, so that its fragmentation products can no longer be expected to be confined to the negative hemisphere of the event.

From the momentum flows of figure 8.10, at low x-Q^2, where the effects of initial state QCD radiation are large, current and target regions appear to merge, so that the division between them is somewhat arbitrary

Since initial state "gluon ladders" have no equivalent in e^+e^- annihilation, a question arises as to whether the comparison between the Breit current region of DIS and a single e^+e^- hemisphere becomes less valid at low x-Q^2.

The assignment to the target region of some proportion of the fragmentation products of the struck quark can be expected to cause a systematic loss of multiplicity from the current region at low x-Q^2, affecting the observed evolution of $< n_{ch} >$ with Q.

If the loss were systematically of soft or hard particles, the position of the $ln(1/x_P)_{max}$, and its apparent evolution with Q, would also be affected.

8.8 Fragmentation in ZEUS 1993 DIS Data

8.8.1 Detector Acceptance and Systematic Effects

Detector effects were taken into account by comparison with Monte Carlo data, using the bin-by-bin correction techniques described in chapter 7, section 7.8.2. As in the momentum flow analysis, the effects of detector acceptance, event reconstruction and selection, track reconstruction and selection, QED radiative effects, migration between x, Q^2 bins, and K^0 and Λ decay products were corrected for. The correction factors were flat in the region of the $D(ln(1/x_P))$ peak, typically with values in the region of ~ 1.3.

An additional effect, also corrected by this technique, is that of migration of tracks between the current and the target regions due to misconstruction of the boost to the Breit frame, which has been shown [54] to make the largest contribution to systematic errors in the Breit frame analysis.

As with the momentum flow analysis, ARIADNE was used to correct the data. The MEPS dataset was also used, to provide a systematic check. A second systematic check was made by comparing two methods of track reconstruction which were concurrently used by the ZEUS collaboration during 1993.

Effects on the values of both $ln(1/x_P)_{max}$ and the $< n_{ch} >$ were understandably largest in the higher Q^2 bins, where statistics were poorest and acceptance affects greatest.

Changes to $ln(1/x_P)_{max}$ were typically about 2–3% with the largest change, in the highest Q^2 bin, being 8%.

The effects on $< n_{ch} >$ were greater, typically in the region of 3–5%, the maximum being 16%.

8.8.2 Determination of $ln(1/x_P)_{max}$

The position of the peak of the $ln(1/x_P)$ distribution in each bin was determined by a gaussian fit over the range $\overline{ln(1/x_P)} - 1 < ln(1/x_P) < \overline{ln(1/x_P)} + 1$, where $\overline{ln(1/x_P)}$ is the statistical mean of the $ln(1/x_P)$ distribution in a given bin.

8.8.3 Evolution of $ln(1/x_P)_{max}$ with Q

Figure 8.13 shows how the position of the $D(ln(1/x_p)$ peak varies with Q. The ZEUS data points correspond to the central values of seven Q^2 bins used in this analysis. The error bars represent the systematic differences mentioned above, added in quadrature to the statistical errors.

The relationship between $ln(1/x_P)_{max}$ and Q is clearly linear. The gradient obtained from a fit to the ZEUS data was $b = 0.658 \pm 0.063$, which is significantly

less than the simple cylindrical phase space prediction of unity, and is consistent with the expected effects of QCD coherence.

Also shown are e^+e^- data from OPAL [56] and TASSO [55], for which $ln(1/x_P)_{max}$ has been redetermined by a gaussian fit, equivalent to that performed on the ZEUS data. The positions of these data points are seen to lie on the line produced by an extension of the fit to the ZEUS data.

The gradient given above also consistent with a value published by OPAL, $b = 0.637 \pm 0.016$, from a fit to the OPAL and TASSO data, where $ln(1/x_P)_{max}$ was extracted using an alternative method [61].

This suggests that the current region of the Breit system, for a DIS event, is indeed, for practical purposes, equivalent to one hemisphere of an e^+e^- annihilation event, and that the fragmentation of quarks in DIS is similar to that of quarks produced in e^+e^- annihilation.

The linearity of the fit, i.e, the consistency of the slope for both high and low Q^2 also suggests that the position of $ln(1/x_P)_{max}$ is relatively insensitive to the effects of migration of tracks to the target region caused by the effect of initial state QCD radiation on event kinematics.

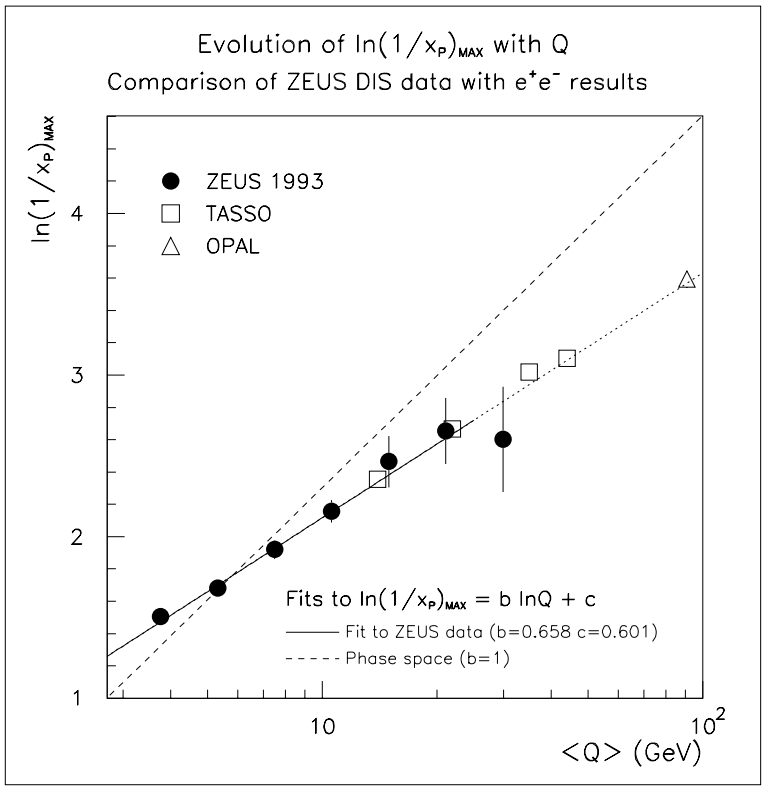

Figure 8.13: *Evolution of the peak of the $ln(1/x_p)$ distribution with Q in the Breit current region of ZEUS DIS events, compared with results from the e^+e^- experiments OPAL and TASSO*

8.8.4 Evolution of $< n_{ch} >$ with Q

Figure 8.14 shows how the mean charged multiplicity in the current region of ZEUS DIS events evolves with Q. As with figure 8.13, the ZEUS data points correspond to the central values of the seven Q^2 bins used in this analysis, and the error bars represent the systematic differences mentioned above, added in quadrature to the statistical errors.

Also shown are the data from e^+e^- experiments, [62],[56],[55],[63] for which the inclusive multiplicities have been halved to provide a comparison with the current region of DIS events.

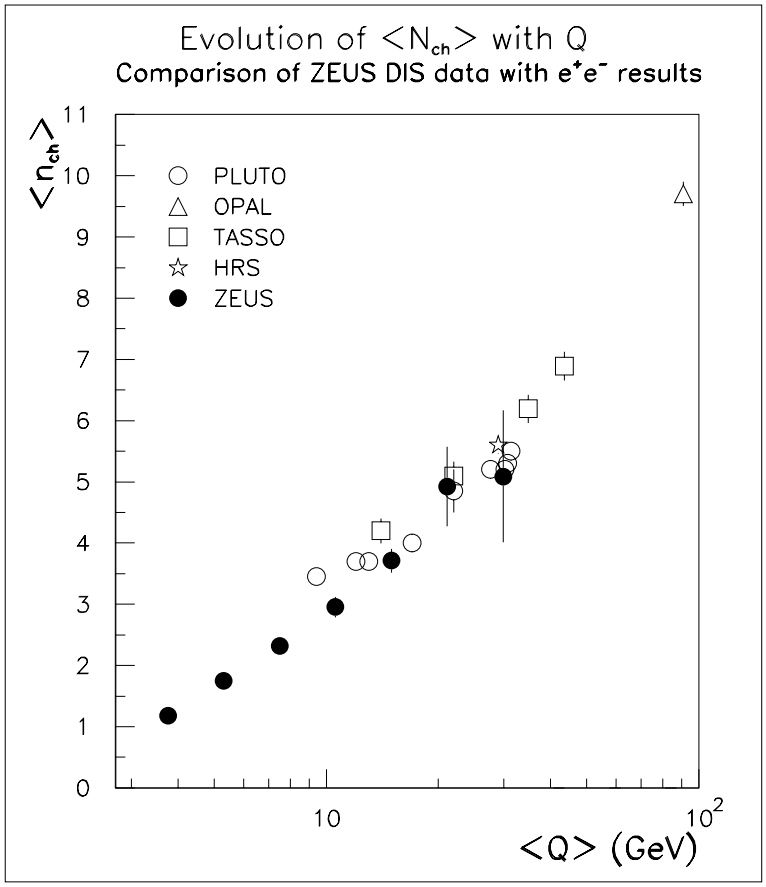

Figure 8.14: *Evolution of mean charged multiplicity with Q in the Breit current region of ZEUS DIS events compared with half the inclusive multiplicity of e^+e^- data.*

It is noticeable that, whereas at higher values of Q the ZEUS DIS data appears to be in good agreement with the e^+e^- data, at lower Q the ZEUS values appear to fall more steeply with decreasing Q than do the corresponding e^+e^- values. This effect, which has been observed in papers published by both the ZEUS and H1 collaborations [64], [65], can be considered to be a direct consequence of

initial state QCD radiation. As discussed in sections 8.7.5 and 8.2.3, this causes the momentum flow peak associated with the current to be shifted in the direction of the remnant, so that some of the tracks associated with the fragmentation of the struck quark are assigned to the target region.

In the most extreme situation the current region can be completely depopulated [66], which could never be the case for a hemisphere of an e^+e^- annihilation event. In this analysis, zero multiplicity in the current region was observed in 31% of the events in the lowest Q^2 bin, 17% of those in the second lowest bin, and 8% of those in the third lowest bin. For the second highest Q^2 bin it was less than 1%, while in the highest bin no events were observed to have the current region completely depopulated.

It is therefore fair to say that, from the point of view of multiplicity, the correspondence between the DIS Breit current region and one hemisphere of an e^+e^- event breaks down at low Q^2, but appears, from the limited statistics available from 1993 ZEUS DIS data, to be good at higher Q^2 where QCD radiation effects are less significant and the typical event topology is closer to the QPM expectation.

Chapter 9

Review

9.1 The Experimental Context

This thesis has been primarily an analysis of the tracking data taken by ZEUS in 1993 – the year in which HERA provided its first inverse picobarn of luminosity, and also the year in which the full readout electronics of the ZEUS Central Tracking Detector was installed.

As such, it has dealt equally with two interdependent concerns. One has been to understand the functioning of a new detector and to gauge the reliability of its data, the other, to learn something of the properties of charged tracks resulting from ep deep inelastic scattering, in the newly-accessible kinematic region $10^{-4} < x \leq 10^{-2}$, $10 < Q^2 \leq 10^3\ GeV^2$.

9.1.1 HERA and ZEUS

The first three chapters of this thesis dealt with the experimental set-up at HERA and ZEUS. Chapter 1 gave a description of the HERA accelerator ring and outlined the principal types of physics which can be investigated by colliding electrons with protons at a centre-of-mass energy of 296 GeV. The Deep Inelastic Scattering process was described, and the kinematic variables x, y and Q^2 were defined. In particular it was noted that at very low x, for which the cross-section is large, QCD corrections to the Quark-Parton Model become increasingly important, so that the kinematics of DIS in this region are expected to differ significantly from the QPM expectation.

Chapter 2 constituted a description of the ZEUS detector, its component subdetectors and its trigger and data acquisition system. In Chapter 3 the CTD and its 1993 operating conditions were described in more detail.

9.2 Detecting and Measuring Charged Particles

Chapter 4 investigated the properties of CTD hits, and possible causes of systematic mismeasurement of hits and tracks. Two studies were undertaken. The first of these was of the detailed FADC "pulse train" signals available from the preliminary 1992 test data. The second made use of "residuals" of hits on long tracks, possible only with the full tracking data of 1993.

9.2.1 Results from 1992 FADC Pulse Trains

From the 1992 pulse train data it was determined that the height of a pulse in the CTD was on average proportional to its integrated size, which confirmed that the use of pulse height as a basis for dE/dx measurement was justified. The main exceptions to this were, as anticipated, very large pulses for which the signal saturates the FADC, and pulses close to cell boundaries, where the signal can be split between two cells.

The effects of overlapping pulses were investigated by artificially overlaying the signals from two single pulses. From this study it was concluded that the two-track resolution of the CTD is the design value of 2.5 mm.

It was demonstrated that the arrival time of the second pulse tends to be overestimated, and its height underestimated. The magnitudes of these effects are dependent on the relative heights of the two pulses and on pulse separation. They are negligible for pulses separated by more than 7.5 mm.

It was found that the digital filter did not always have the desired effect of improving the two-pulse resolution and, since it also caused degredation of dE/dx measurement, its use was abandoned for the forseeable future.

9.2.2 Results from Studies of Residuals

Shifts in the residuals of hits on long tracks proved to be a very effective diagnostic of systematic effects in the CTD.

Mismeasurement of hit position can be caused either *(a)* by assignment of the wrong arrival time, which can happen when the pulse shape is different to that assumed, or *(b)* by an error in the conversion from time to distance, if either the drift path or velocity differs from that assumed. In this thesis, significant systematic effects attributed to *(a)* were observed in the residuals of hits from very small pulses and hits from saturated pulses, while effects attributed to *(b)* were observed in the residuals of hits close to cell boundaries and, importantly, hits on tracks at shallow angles to the plane of ionisation drift – the "ψ' effect" which introduces a difference in the reconstruction of positive and negative tracks.

Corrections for these systematic effects have been implemented offline, contributing to an improvement of about 70 μm in the hit resolution of long tracks.

Correlated with the ψ' effect, a tendency was observed for pulses to break up, producing spurious extra hits in close proximity to genuine hits. These additional noise hits cause confusion in pattern recognition; the third level trigger currently ignores any hit which follows within 100 ns of a previous hit on the same wire.

9.2.3 Tracks for Physics Analysis

Chapter 5 dealt with the assignment of tracks to the main event vertex and investigated the possibility of discrimination between positive and negative tracks, in light of the systematic effects identified in Chapter 4. Although positive tracks tended to be better reconstructed than negative tracks, there was no observable systematic loss of negative tracks from the event vertex. In general, tracks with $P_T > 200MeV$ in the polar angle region $-1.5 < \eta < 1.5$ were considered to be reliably measured for the purpose of physics analysis.

9.3 DIS Final-State Charged Hadrons

9.3.1 Event Reconstruction, Selection and Simulation

Chapter 6 of this thesis explained the methods employed at ZEUS to reconstruct event kinematics, the selection of the DIS event sample, and the removal of background events. The three Monte Carlo datasets used in this analysis, ARIADNE, MEPS and HERWIG, were also described.

9.3.2 Momentum Flow Analysis

The energy or momentum flow of the final-state hadrons of DIS events is sensitive to the effects of QCD corrections to the quark-parton model, which are important for the kinematic region under study in this thesis ($10^{-4} < x \leq 10^{-2}$, $10 < Q^2 \leq 10^3\ GeV^2$) where the proton structure is dominated by the sea quark and gluon density functions. Analysis of energy or momentum flow does not require jet identification, an advantage because events in this region often lack a clearly defined "jet" configuration in the HERA frame.

In Chapter 7, the momentum flow in pseudorapidity ($\Delta\eta$) of tracks assigned to the event vertex was measured with respect to the nominal direction of the struck quark defined by the event kinematics. These were reconstructed from the energy measured by the calorimeter, using the vertex position given by the tracking to define the angles. Track momentum flow in azimuth ($\Delta\phi$) was measured with respect to the scattered electron identified by the calorimeter.

Electron tracks were identified by matching with the calorimeter-identified electron, and were removed from the sample.

The hadronic momentum flow versus $\Delta\eta$ exhibited a characteristic two peaked structure, as had previously been observed in calorimeter energy flow studies. A forward peak at large $\Delta\eta$ was identified with the target remnant. The other peak, identified with the struck quark, was shifted forward from $\Delta\eta = 0$, which was also in agreement with previous calorimeter studies. This forward shift of the "current peak", which is believed to be caused by QCD radiation, was observed to be greatest at low x, Q^2, where QCD effects are most significant, and least at high x, Q^2. Effects of QCD radiation are also thought to be responsible for the momentum flow observed in between the two peaks.

The particle flow versus $\Delta\eta$ did not show separate current and target peaks.

Comparing the results of the three Monte Carlo models which were passed through the full detector simulation it was found that the ARIADNE sample, which was based on the colour dipole model with the boson-gluon process added, gave the best overall description of both the momentum and particle flow. In particular, the MEPS sample underestimated the forward flow at low x, Q^2, while the HERWIG sample overestimated it.

The ARIADNE sample was used to correct the ZEUS data for detector effects.

The momentum flow versus $\Delta\phi$ exhibited a peak opposite in azimuth to the scattered electron, as expected. This peak was more pronounced at higher x, Q^2. The ARIADNE and HERWIG samples both described the data well, MEPS less so.

The momentum flow in the $\Delta\eta$-$\Delta\phi$ plane showed an expected cone of momentum flow correlated in ϕ with the nominal struck quark direction and shifted slightly forward in $\Delta\eta$. There was also the forward peak in $\Delta\eta$ which, as might be expected for the target remnant, was flat in azimuth. Between them, however, a band of momentum flow showed a marked azimuthal correlation with the quark direction, even at quite large $\Delta\eta$, which could be interpreted as further evidence of colour flow between the current and target.

For "diffractive" DIS events, identified by a lack of calorimeter energy in the forward region, the tracking data confirmed a lack of forward momentum flow, while the current peak in showed very little forward shift in $\Delta\eta$. Both of these characteristics indicate reduced QCD radiation between the current and target.

In Chapter 8, the four-vectors of the reconstructed tracks were boosted to the Breit frame. Here, the struck quark completely reverses direction, having a pseudorapidity $\eta^* = -\infty$, so that the particles correlated in η-ϕ with the struck quark in the laboratory frame have large negative values of η^*, while particles correlated with the remnant direction have large positive η in both the laboratory and Breit frames.

In the Breit frame, the momentum flow versus η^* showed very little evidence of a current peak. The dominant feature, particularly at low x, was a pronounced forward peak due to the very high energy of the remnant in this frame.

9.3.3 Breit Frame Analysis of Fragmentation

In the Breit frame, the direction of the outgoing quark, in the QPM configuration, is given by the negative Z-axis and its energy is $Q/2$. The negative hemisphere of a DIS event, or *current fragmentation region*, is considered to consist of the final-state hadrons associated with the struck quark, and is equated with one hemisphere of an e^+e^- annihilation event. If a given hadron has momentum P, the scaled momentum variable $x_P = 2P/Q$ (or, for e^+e^-, $2P/\sqrt{s}$) can be regarded as the fraction of the original quark's momentum carried by the hadron. The scaled momentum distribution $D(\ln(1/x_P)) = 1/N_{evts}\, dn_{ch}/d\ln(1/x_P)$, or the *charged fragmentation function*, provides evidence of how the original quark evolves into the observed final-state hadrons.

In Chapter 8 of this thesis $D(\ln(1/x_P))$ was plotted in seven ranges of Q^2. As with the previous momentum flow distributions, the data were corrected bin-by-bin for detector effects using the ARIADNE Monte Carlo dataset.

The position of the peak of the distribution in each Q^2 range was determined by a Gaussian fit. The evolution of peak position with $\ln(Q)$ was observed to be linear; the fitted gradient, $b = 0.658 \pm 0.063$, was significantly less than the value

of unity expected from simple phase space considerations and was consistent with the expected effects of QCD coherence. It was also consistent with results from the e^+e^- experiments OPAL and TASSO.

The evolution with Q of the mean multiplicity $< n_{ch} >$ in the current region was plotted and compared with data from e^+e^- experiments. At higher values of Q there was good agreement, but at lower Q the ZEUS values were lower than those from e^+e^- annihilation. For the lowest values of Q, which also correspond to low x, there was no e^+e^- for direct comparison, but for a significant proportion of the ZEUS events zero multiplicity was observed in the current region, which could clearly not be the case for an e^+e^- event hemisphere.

This is believed to be caused by the QCD corrections to the QPM, responsible for the forward shift of the momentum flow peak observed earlier. When these QCD effects are present, the kinematics are altered so that the fragmentation region of the struck quark no longer coincides in the Breit frame with the negative hemisphere of a DIS event. These effects are less significant at higher x, Q^2, so the agreement between DIS and e^+e^- is better in this region.

Analysis of fragmentation in the Breit frame, therefore, confirms that at low x, Q^2 QCD radiation significantly changes the typical event configuration with respect to the QPM expectation. These effects systematically reduce the average multiplicity in the current region, but do not appear to significantly affect the $D(\ln(1/x_P))$ peak position or its evolution, which is consistent between both DIS and e^+e^- annihilation experiments.

Afterword

And so, we have begun to learn how to look at the structure of the proton and the interactions of its constituents through the "eye" of the ZEUS detector. In the years to come, we will benefit from increasing experience in the operation of HERA the microscope and in the interpretation of the data it provides. We might also gain further awareness of the sophistication, efficiency and versatility of the photon detectors we are born with.

One moonless Hamburg night I arrived outside my front door after cycling back from DESY. Photon detectors were almost useless under the prevailing conditions, but my brain was obviously doing its utmost to process the limited data available to it, for I came to discern, as patches of darkness within the darkness, the familiar shapes of the bicycle shed, bushes, the neighbour's bird bath, and . . . my consciousness was triggered by a circular patch of darkness that did not belong there. Something told me "animal", which puzzled me because, although I could resolve no details of its substructure, it appeared not to possess any of the gross features, e.g. head, legs, movement, that I normally associated with animals. From my unconscious came another message, "hedgehog".

I had never encountered one of these in my life, but from my second-hand knowledge I could see neither anything inconsistent with nor anything specific to a hedgehog. Having exhausted the capabilities of sight, I reached down and touched the object. Its texture was that of a bristle doormat. That, I decided, supported the hypothesis of a hedgehog. I gave it a gentle push, and found that it resisted being rolled forwards in a way which was entirely consistent with its having legs and a will of its own. When I returned from locking my bicycle in the shed, it had vanished.

From HERA we have already gained new insight into the structure of the proton and the interactions of its constituents. Hopefully, with the continued accumulation of statistics, we will be able to make various high-precision measurements which will unambiguously verify or refute some of our current hypotheses. Perhaps, however, it is also possible that somebody, scrutinising some scanty data from a region that HERA and its detectors are ill-designed to measure, will suddenly exclaim "I know! It's a hedgehog!" and be absolutely right.

Bibliography

[1] E.Rutherford, **Phil. Mag. 21 (1911) 669**

[2] G.Ingelman and R Rückl, **Phys. Lett. 201 (1988) 369**

[3] C.G.Callan and D.Gross, **Phys.Rev.Lett. 22 (1969) 156**

[4] J.I. Friedman and H.W.Kendall, **Annual Review of Nucl. and. Particle Science 22 (1972) 227**

[5] R.P.Feynman, *Photon Hadron Interactions*, W.A.Benjamin, New York 1972

[6] G.Atlarelli and G.Parisi, **Nucl. Phys. 126 (1977) 297**

[7] ZEUS Collaboration, M.Derrick et al., **Phys. Lett. B 316 (1993) 412**

[8] H1 Collaboration, I.Abt et al.,**Nucl. Phys. B 407 (1993) 515**

[9] L.V.Gribov,E.M.Levin and M.G.Ryskin, *Semi-hard Processes in QCD*, **Phys. Rep. 100 1-2 (1983) 284**

[10] ZEUS Status Report, ZEUS Collaboration 1990

[11] J.H.C.Roberts, **RAL-87-095** 1987

[12] J.C.Giddings, **PhD Thesis**, Imperial College London 1993

[13] G.Blair et al., *Calibration of the CTD using the 1992 Autumn Data*, **ZEUS-Note 92-122**, January 1993

[14] N.McCubbin, G.Hartner, **ZEUS Offline Documentation**

[15] R.Brun et al., **GEANT 3.13**, CERN DD/EE/84-1 1987

[16] J.Shulman, *Obtaining the r-ϕ Hits from the FADC Trains*, **ZEUS-UCL-89-5**, University College London 1989

[17] N.Dyce et al., *The CTD Reconstruction Programme User's Guide*, **ZEUS-Note 94-011**, February 1994

[18] F.F.Wilson, *The Design and Optimisation of the ZEUS Central Tracking Detector*, **PhD Thesis**, University of Bristol 1989

[19] J.Shulman, *Multi-Pulse Performance of a Test Drift Cell for ZEUS*, **PhD Thesis Part II**, Imperial College London 1988

[20] J.Shulman, P.Kaziewicz, **Private Communication** May 1993

[21] J.Lane, **Presentation at the ZEUS Tracking Meeting**, DESY 20th January 1994.

[22] C.Catterall, **Presentation at the ZEUS Tracking Meeting**, DESY 21st April 1994

[23] J.Shulman, **Private Communication** June 1994

[24] G.Bruni et al., *A Description of TGTRAK and Associated Tables*, **ZEUS-Note 94-009**, 1994

[25] D.Bandyophadhyay et al., *VCTRAK Offline Output Information*, **ZEUS-Note 93-122**, 1993

[26] P.Billoir and S.Qian, **Nucl. Instr.and Meth. A311 (1992) 139**

[27] C.D.Catterall, M.Derrick, J.B.Lane and L.M.Shcheglova, *A First Look at Multiplicity Distribution in DIS Events with 1993 CTD Data*, **ZEUS-Note 93-130**, December 1993

[28] B.Foster, **Presentation at the ZEUS Collaboration Meeting**, February 1994

[29] C.Catterall, **Presentation at the ZEUS Weekly Meeting**, 22 May, 1995

[30] J.Shulman, **Presentation at the ZEUS Collaboration Meeting**, June 1995

[31] J.Feltesse, *Measurement of Inclusive Differential Cross Sections*, **Proceedings of the HERA Workshop, p. 33-58**, DESY 1987

[32] F.Jacquet and A.Blondel, **Proceedings of the Study of an ep Facility for Europe 79/48, p.391-394**, U. Amaldi ed. 1979

[33] S. Bentvelsen, J.Engelen, P.Koojiman, *Reconstruction of (x, Q^2) and Extraction of Structure Functions in Neutral Current Scattering at HERA*, **Physics at HERA, Volume 1**, DESY 1991

[34] S.Bentvelsen and P.Koojiman, *Reconstruction of x and Q^2 and the Effects of Initial State Radiation*, **ZEUS-Note 91-57**, 1991

[35] H.Abramowicz et al., *A Determination of F_2 with the 1992 Data* **ZEUS-Note 93-078** 1993

[36] M.Rocco, **PhD Thesis**, University of Iowa 1994, DESY F35D-94-04

[37] A.H.Mueller, ed., **Perturbative Quantum Chromodynamics** World Scientific, Singapore 1989

[38] A.D.Martin, R.G.Roberts and W.J.Stirling, **Phys. Lett. B 316 (1993) 145**

[39] G.Ingelman, **Physics at HERA Vol.3 p. 1366**, DESY 1992

[40] l.Lönnblad, *ARIADNE 3.1* **Comput. Phys. Commun. 71 (1992) 15**

[41] A.Kwiatkowski, H.Spiesberger and H.-J.Möring, **Physics at HERA Vol.3 p.1294** DESY 1992

[42] A.Kwiatkowski and H.Spiesberger, **Physics at HERA Vol.3 p.1419** DESY 1992

[43] B.Anderson et al., **Phys. REp. 97 (1983) 31**

[44] T.Sjöstrand and M.Bengtesson, **Comput. Phys. Commun. 43 (1987) 347**

[45] M.Glück, E.Reya and A.Vogt, **Phys. Lett. B306 (1993) 391**

[46] G.Marchesini et al., **Comput. Phys. Commun. 67 (1992) 465**

[47] G.Marchesini and B.R.Webber, **Nucl. Phys. B 310 (1988) 461**

[48] D.Bandyopadhyay, **ZEUS Internal Software** 1993

[49] ZEUS Collaboration, M.Derrick et al., **Phys. Lett. B 338 (1994) 483**

[50] H.Beier, **Diploma Thesis University of Hamburg**, DESY F35D-94-07 1994

[51] ZEUS Collaboration, M.Derrick et al., **Phys. Lett. B 315 (1993) 481**

[52] H1 Collaboration, I.Abt et al.,**Nucl. Phys. B 407 (1993) 515**

[53] B.Levtchenko, *The Breit System (Primer)* **ZEUS-Note 94-099** August 1994

[54] V.A.Jamieson **PhD Thesis University of Glasgow** 1994

[55] TASSO Collaboration, W.Braunschweig et al., **Z. Phys. C 45 (1989) 193**

[56] OPAL Collaboration, M.Z.Akrawy et al., **Phys. Lett. B 247 (1990) 617**

[57] L3 Collaboration, B.Adeva et al., **Phys. Lett. B259 (1991) 199**

[58] Ya.I.Azimov, Yu.L.Dokshitzer, V.A.Khoze and S.I.Troyan, **Z. Phys. C31 (1986) 213**

[59] Yu.L.Dokshitzer, V.A.Khoze, A.H.Mueller and S.I.Troyan, *Basics of Perturbative QCD*, **Editions Frontieres** 1991

[60] Ya.I.Azimov, Yu.L.Dokshitzer, V.A.Khoze and S.I.Troyan, **Z. Phys. C27 (1985) 65**

[61] H.Kreutzmann, **PhD Thesis University of Bonn**, Bonn-IR-91-08

[62] PLUTO Collaboration, Ch.Berger et al., **Phys. Lett. B 95 (1980) 313**

[63] HRS Collaboration, M.Derrick et.al., **Phys. Rev. D 34 (1986) 470**

[64] ZEUS Collaboration, M.Derrick et al., **Z. Phys. (1995) 93**

[65] H1 Collaboration, T Ahmed et al., **Nucl. Phys. B445 (1995) 3**

[66] K.H.Streng, T.F.Walsh, and P.M.Zerwas, **Z. Phys C2 (1979) 237**